THE DEVELOPMENT AND SIGNIFICANCE OF GEOMETRIC PATTERNS IN ROCK-MELT MIXTURES: INSIGHTS FROM NUMERICAL MODELLING

GIULIA FEDRIZZI

Supervisors:
Prof. Sandra Piazolo
Dr. Sam Pegler
Dr. Oliver Harlen

Submitted in accordance with the requirements for the degree of Doctor of Philosophy

THE UNIVERSITY OF LEEDS

Centre for Doctoral Training in Fluid Dynamics
School of Computer Science

December 2024

Intellectual Property

I confirm that the work submitted is my own and that appropriate credit has been given where reference has been made to the work of others.

Acknowledgements

I wish to thank my supervisors, Sandra Piazolo, Sam Pegler and Oliver Harlen, for their constant support, countless meetings and encouragement throughout this journey. In particular, I am grateful to Sandra for her early enthusiasm for my research interests and for encouraging me to apply for the CDT. I am especially thankful to Daniel Koehn, who, as an informal supervisor, provided the code for the numerical part and patiently answered my numerous questions.

A big thank you to James for always supporting me and being there from the moment I applied to the submission of this thesis. Thank you also for your help in so many technical areas – from programming and GIS to geochemistry and language questions. I think I even have a vague understanding of C++ pointers now.

I also want to thank Danielle, my CDT 'twin', with whom I shared so much: our MSc project, PhD supervisory team, conferences, countless tea breaks, trips to Helix, and the general chaos of our PhD journeys.

Next, I would like to thank the CDT in Fluid Dynamics and the people in the CDT office(s) for sharing this experience with me. Special thanks to Peter and Claire for always solving problems quickly and making the paperwork almost bearable. Thank you to my fieldwork mates, Manon and Eleanore, for their help during this part of the project.

Finally, I want to thank my family for their support (with a special mention to my cousins!), and especially my parents for instilling in me a passion for science and curiosity. Grazie!

The numerical experiments performed in this project were run on ARC3, part of the High Performance Computing facilities at the University of Leeds, UK.

This work was funded by the UK Engineering and Physical Sciences Research Council (EPSRC) grant EP/S022732/1 for the University of Leeds Centre for Doctoral Training in Fluid Dynamics.

Abstract

The presence of melt in the Earth's lower and middle crust plays a crucial role in crustal evolution, rheology, and magmatic processes. Melt generated at depth can either remain in place or migrate towards shallower levels, forming magmatic bodies in the upper crust. The efficiency of this migration is strongly affected by the spatial distribution and connectivity of the melt. Zones of partial melting are complex environments and can be influenced by multiple interacting processes. These processes leave distinct signatures in the melt distribution, indicating that melt geometrical patterns can be used to interpret the mechanisms active during their formation. However, the exact link between the processes and their effect on the melt patterns has not been fully understood.

This study uses a hybrid discrete-continuum model to investigate the interplay between the rates of melt production, melt pressure diffusion, extensional deformation and pre-existing structures in shaping melt distribution patterns. Our numerical experiments show that when the melt production rate exceeds pressure diffusion, melt pressure accumulates, leading to the formation of well-connected hydrofracture networks. In contrast, systems dominated by pressure diffusion exhibit fewer and smaller fractures, favouring porous flow rather than fracture-driven migration. The introduction of extensional deformation promotes the development of shear fractures and organised, asymmetrical patterns. In systems that show compositional layering, hydrofractures develop inside fertile layers and parallel to their boundaries. The interactions between such structures and deformation create complex fracture geometries, enhancing connectivity and facilitating melt transport. We compare the geometric patterns that emerge from the numerical experiments with those observed in natural melt veins or dykes from two study areas, one in the Lewisian Complex in NW Scotland and the other in the Rogaland region in Norway. These comparisons provide insights such as the timing of deformation, the role of melt pressure and the influence of compositional banding.

This work highlights the importance of understanding the links between geometrical patterns in melt distribution and active processes, providing a framework for interpreting melt networks in natural systems.

Contents

List of Figures

Chapter 1

Introduction

The production and migration of melt are fundamental processes in the Earth's lower and middle crust (e.g., Vanderhaeghe 2009). For instance, these processes play a critical role in crustal differentiation, driving changes in chemistry and making the lower crust more mafic and less hydrated, while the upper crust becomes more felsic and hydrated (Brown & Rushmer 2006, Brown 2013). The presence of melt also greatly impacts crustal rheology, as melt dramatically weakens the crust (e.g., Van der Molen & Paterson 1979, Rushmer 1991, Vanderhaeghe 2009). Melt generated at these depths can migrate from its source, often becoming the precursor to magmatic bodies that are emplaced in the upper continental crust (Cruden & Weinberg 2018). However, the effectiveness of these processes is strongly influenced by the spatial distribution of melt fractions, as the connectivity of the melt network largely determines its ability to migrate to shallower levels.

During partial melting, several processes are active concurrently, shaping the spatial distribution and flow of melt. In particular, geometric patterns in melt distribution are affected by the relative rates of processes such as melt production, melt pressure diffusion and external deformation (Brown & Solar 1998). This complexity is further intensified by pre-existing structures in the host rock, which can strongly influence melt pathways. By understanding how specific processes affect these patterns, we can identify the mechanisms that were active and that influenced melt networks. Linking processes to melt geometry not only allows us to understand the interactions between processes but also provides insights into the efficiency of melt migration through the crust.

In the literature, much of the interpretation at the outcrop scale relies on observational data. Melt patterns are typically classified based on their geometry, with less emphasis on the underlying processes that produced them. Numerical studies, while giving valuable insights on specific problems, are often limited in scope. They typically focus on individual mechanisms, such as the efficiency of porous flow (e.g. Dannberg & Heister 2016) or the ascent rates of diapirs (Weinberg & Podladchikov 1994). Consequently, many studies based on numerical models do not consider the spatial signatures that these processes leave in the rock record, such as melt distribution patterns, which constitutes a significant gap in the literature.

The many factors that influence melt mobility make these systems highly dynamic. When modelling such complex systems it is essential to consider the feedbacks between numerous mechanisms. These mechanisms include, for example, the opening of a fracture and the resulting pressure dissipation (Nicolas & Jackson 1982). While such principles are well-documented in aqueous fluid systems (e.g. Koehn et al. 2020), they become even more complex when partial melting is involved. Partial melting directly increases porosity and significantly influences the response of the solid fraction.

1.1 Research Questions

This thesis aims to systematically investigate the relative rates of processes that are active during partial melting and their effect on the spatial distribution of melt through time. The goal is to predict the effects of the various processes and link them to the melt patterns. A hybrid model (Ghani et al. 2013), combining a continuum approach with a Discrete Element Model (DEM) component, is employed to simulate the porous flow of melt alongside the elastic response of the solid rock.

The main research questions explored in this thesis are:

- How do the relative rates of melt production, melt pressure diffusion, and external deformation influence fracture and melt patterns?
- What are the feedback mechanisms between the different processes?
- Is external deformation necessary for the formation of interconnected, melt-filled fracture networks?
- How do pre-existing structures in the host rock such as compositional layering affect melt distribution and fracture development?
- How can the resulting fracture networks be quantified or measured and how can this help us assess their connectivity and efficiency in melt migration?
- Can the results of this numerical model be applied to real-world field data, and what insights can they provide about the tectonic environment during rock formation?

1.2 Thesis Outline

This thesis is composed of 9 chapters, including this introduction. Chapter 2 reviews the current literature on the influence of melt presence on the rheology, deformation and brittle behaviour of the lower and middle crust, discusses melt migration and migmatite classification and examines modelling approaches. Chapter 3 describes the two study areas and the questions arising from observed melt patterns, providing the rationale for our numerical modelling. Chapter 4 includes a description of the numerical code and methods of pattern analysis. Chapter 5 presents the tests performed on the model to ensure robustness and some improvements to the code. This is followed by three chapters of original scientific research (Chapters 6, 7 and 8), which investigate the relative roles of melt viscosity and melt production rates, the effect of extensional deformation, and the influence of compositional layering, respectively. The contents of these three chapters are organised in the form of manuscripts to be submitted as journal papers. Therefore, they include some repetitions of other chapters. Chapter 9 includes a general discussion of the thesis findings, addresses the limitations of the model, proposes future research directions and concludes the study.

Chapter 2

Background

This chapter provides an overview of the current knowledge regarding zones with melt presence in the lower and middle crust. It begins by discussing the general rheology of these crustal levels, including their responses to deformation and fluid pressure, followed by the effects of melt presence and its consequences. The discussion highlights how melt can influence the crust's deformation response and enhance brittle behaviour. The chapter also reviews the mechanisms of melt migration, covering pervasive porous flow, dyking, hydrofractures, and diapirism. It summarises how migmatites have been classified based on observational criteria and examines the interpretations made regarding the effects of processes on melt geometric distribution. Finally, it explores current approaches to modelling and simulating these processes.

2.1 The Rheology of the Lower and Middle Crust

Decades of experiments in rock mechanics, seismic observations, micro- and macrostructural studies have provided us with complementary views of the rheology of the lower and middle crust. Ductile behaviour is common for the solid component in a rock-melt mixture (Bürgmann & Dresen 2008). Due to the high temperature in these environments, it is expected to observe ductile structures in the same areas as melt (e.g. Brown

& Solar 1998, Weinberg & Regenauer-Lieb 2010).

Deformation tends to localise in places that highly depend on the local distribution of a variety of parameters, like local mineralogy, grain size, the presence of fluids and their composition, temperature, pressure, stress conditions, melt content and melt distribution (Bürgmann & Dresen 2008 and references therein). Furthermore, due to such heterogeneities, the same rock can often exhibit brittle and ductile behaviour at the same time (Bell & Etheridge 1973, Weinberg & Regenauer-Lieb 2010). In this case, the behaviour is likely to be determined by the rate of deformation: an elastic (brittle) response is typically triggered by a high rate whereas ductile, time-dependent flow happens when deformation is applied gradually (Piazolo et al. 2019).

2.1.1 Hydrofractures

Hydrofractures are defined as the brittle failure in rocks caused by fluid overpressure. Their importance was first investigated by Hubbert & Willis (1957) and Hubbert & Rubey (1959). Fluid overpressure can be caused by many processes but in rocks it is often the consequence of processes like thermal expansion, dewatering, metamorphic reactions or density-driven fluid migration (Fyfe 1978, Cox 2005).

To understand the role of fluid in the fracturing of the host rock, Mohr diagrams are often used to represent the 2-D stress states of materials (Figure 2.1). The x and y coordinates of each point of a circle represent the magnitude of the normal (σ_n) and shear (τ) stress respectively. When the circle intercepts the Mohr-Coulomb failure envelope (labelled as 'failure curve' in Figure 2.1), the rock fails and the location of this interception will determine the type of fractures that develop in the rock. Mode I fractures occur when the circle cuts the failure curve in the extensional regime. They open in a direction that is perpendicular to the maximum tensile stress and they are typical of hydrofractures. Mode II fractures occur in the compressive regime and they open at an angle (θ) to the maximum principal stress. Fracturing in the compressive regime generally requires higher effective stresses. However, applying

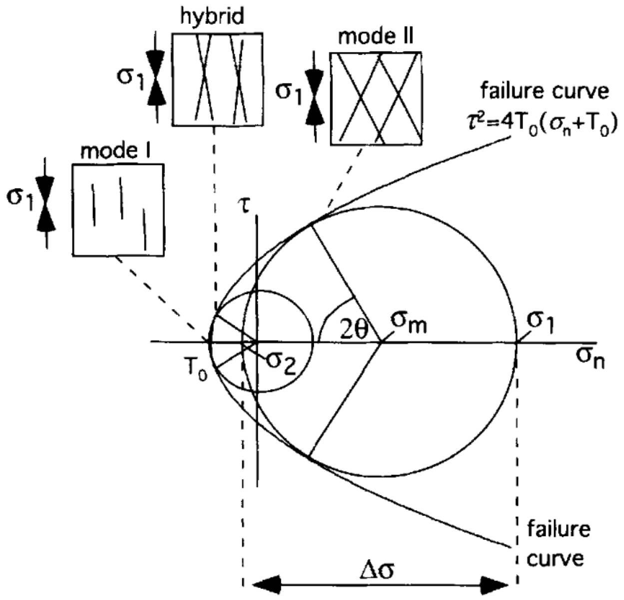

Figure 2.1: Mohr diagram showing how different conditions produce different fracture types. Fluid overpressure can trigger a tensile failure (smaller circle, mode I fractures) by moving circles towards the left-hand side of the diagram. The larger circle produces type II fractures as it intercepts the envelope in the compressive regime. From Koehn et al. (2005).

fluid overpressure shifts the circles towards the left-hand side of the graph. In this case, stress states that used to be stable (because they were far from the failure curve) can be moved until they intercept it in the negative x (σ_n) half-plane. A stress state represented by the small circle in Figure 2.1 will therefore produce mode I or hybrid fractures because of fluid overpressure.

Once fractures start forming, their propagation is influenced by the fluid gradient magnitude and orientation, the host rock mechanical properties and the discontinuities of the system (Vass et al. 2014). The permeability of the host rock is deeply affected by the onset and propagation of new fractures, therefore cracks will significantly control the flow of the fluid (Cox 2005).

2.1.2 The Role of Melt

It is known that even a few percentages of molten material have a significant effect on the aggregate's rheology (Kohlstedt & Zimmerman 1996, Vanderhaeghe 2009). In particular, the distribution and connectivity of melt have a great influence on the bulk rheology (Dell'Angelo & Tullis 1988, Brown 2013). Experiments have shown that with the onset of partial melting, rocks exhibit a drop in their strength of about two orders of magnitude (Van der Molen & Paterson 1979, Paquet et al. 1981, Dell'Angelo & Tullis 1988), which is reported in the melt content-aggregate strength plot in Figure 2.2b.

There are two fundamental geometric thresholds for the strength of a partially molten rock. The first one occurs when melt reaches fluid connectivity (Figure 2.2a, between the first two stages) and the second when the aggregate loses the solid continuity (Figure 2.2a, between the second and third stage). These situations can usually occur only if melt remains in the same volume where it originated. However, if melt leaves its source layer (melt segregation), the fluid fraction will not increase enough to reach connectivity. Whether a volume of rock can reach such stages or not also depends on the timescale of melt formation compared to that of melt loss, as highlighted by Diener & Fagereng (2014). When the rate of melt production is greater or equal to that of melt segregation, melt is likely to leave the source rock continuously. If melt production is slower than migration, melt loss will occur in pulses triggered when the fluid fraction reaches the value defined as percolation threshold (Handy et al. 2001). Mechanisms that favour or hinder melt migration are therefore important to understand when studying crust rheology and structure.

Melt-Enhanced Embrittlement

The mechanisms that govern hydrofracturing with an aqueous fluid and with melt are very similar (Rivalta et al. 2015). An increased melt pressure moves the brittle-plastic transition towards greater depths (Brown & Solar 1998, Davidson et al. 1994). This means that, as the pore-fluid pressure increases, brittle behaviour can be observed at progressively lower levels in the Earth's crust. Fractures occur for smaller values of differential stress, increasing the brittle field for shear fracturing as well (Etheridge et al. 2021).

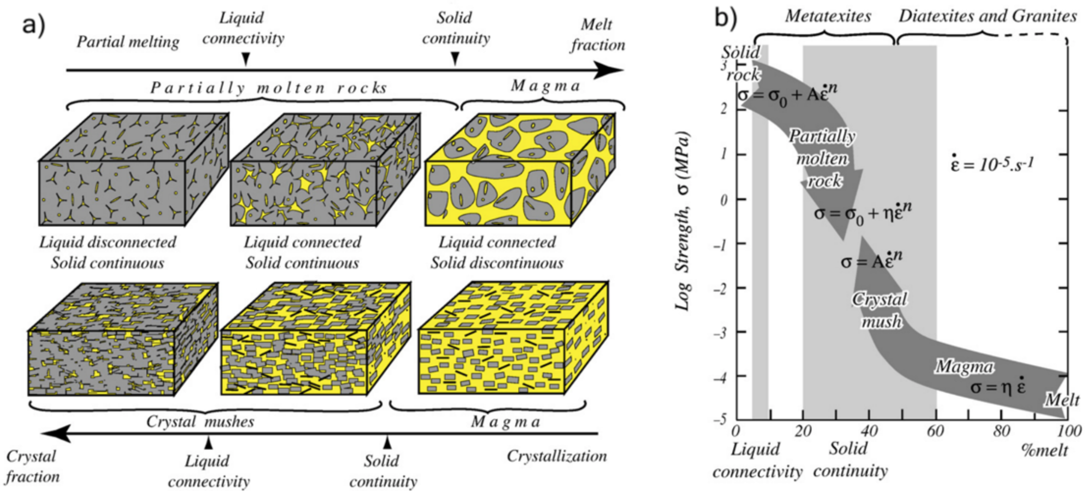

Figure 2.2: (a) Evolution of melt distribution in a rock undergoing progressive partial melting (first row) and crystallisation (second row, right to left). The two geometric thresholds for the viscosity drop happen at the transition between these stages and are highlighted in grey in Figure (b), which shows crustal strength evolution as a function of melt percentage. From Vanderhaeghe (2009).

When vapour-absent partial melting occurs in crustal rocks, it is usually associated with a volume increase of the mineral-melt assemblage (Clemens & Mawer 1992, Rushmer 2001, Etheridge et al. 2021). Several experimental works have shown that this behaviour promotes the switch from a ductile regime, where deformation is accommodated mainly by dislocation or diffusion creep, to cataclasis in the host rock. Experiments by Van der Molen & Paterson (1979) observed microfracturing in a wide range of melt percentages, from less than $\sim 3\%$ up to $\sim 20\%$. They highlighted the importance of fractures and suggested that it is these cracks, rather than melt viscosity, that control flow, as flow stress does not show strain rate sensitivity. However, the confining pressure in their experiments was only 300 MPa and the strain rates were as high as 10^{-5} s^{-1}, making brittle failure very easy. Dell'Angelo & Tullis (1988) applied a larger confining pressure (1500 MPa) and varied the strain rate. For melt fractions between ~ 5 and 10% at 10^{-6} s^{-1}, dislocation creep and melt flow can accommodate the excess melt pressure and no fractures are formed. However, a rate of 10^{-5} s^{-1} did not allow enough time for melt to flow fast enough and the high pore pressure resulted in cataclasis. Their conclusion was that the relative rate of melt flow and strain rate controls the deformation regime, with cataclasis occurring when melt flow is slow and creep accommodating strain when the flow rate is comparable with the strain rate.

At a larger scale, melt overpressure can be the cause of macroscopic fractures. For example, Davidson et al. (1994) observed the presence of melt-filled fractures, usually exhibiting a predominant orientation, in rocks from the Central Gneiss belt (British Columbia, Canada). Moreover, these fractures are sometimes found in conjugate sets, following the orientations predicted by the Mohr failure criterion. The angle of these shear cracks can be used to estimate the differential stress at the time of fracturing. The tensile stress of a partially molten rock is also expected to be quite low, with the lithology that they studied, the Gosford sandstone, estimated to have a tensile strength of -3.6MPa. In some places, tensile brittle fractures, semi-brittle fractures and distributed ductile shearing were found in the same outcrop: This observation shows that the different processes were active at the same time and that the behaviour of the host rock is likely to be determined by local conditions.

Clemens & Mawer (1992) suggested that melt-induced fractures and their propagation in the host rock are critical phenomena in the segregation and ascent of melt. These mechanisms make melt migration much more efficient than density contrasts alone, especially for granitic compositions. Melt-induced fracturing can lead to the formation of tensile (mode I) fractures even when the general orientation of stresses is compressional. Many studies that followed showed how fracturing can be induced by an increase of volume of the material undergoing phase change. Brown et al. (1995) confirmed with their model that migration times calculated based only on gravity-driven compaction were consistent with times observed only for water-rich granite. This was not true in the case of dry compositions: Additional driving forces were needed to explain widespread melt segregation in volatile-absent melting. This was explained by considering the volume changes that happen during phase transition, which are positive in the case of anhydrous phases and negative in volatile-rich ones. The addition of expansion during phase change produced fractures that promoted

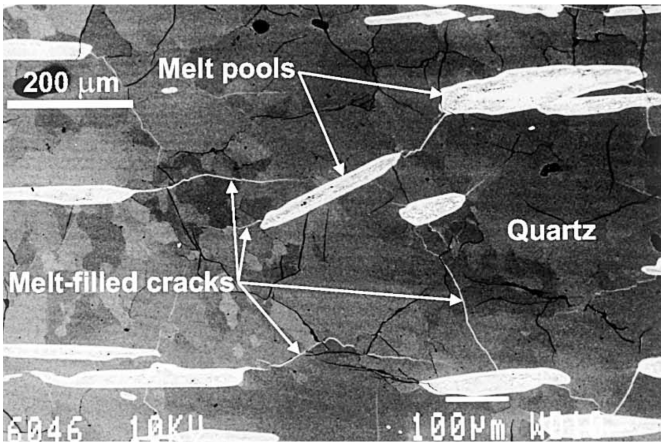

Figure 2.3: Scanning back-scattered-electron microscopy image showing cracks and melt pools caused by partial melting when muscovite and quartz are involved. Fractures connect melt pools and were filled with melt. From Connolly et al. (1997).

melt escape and simulated melt migration in a geologically reasonable timescale for dry environments.

Partial melting of migmatites involves incongruent melting that forms new mineral (solid) phases and a melt phase (Davidson et al. 1994). These sets of reactions are usually fluid-absent for two main reasons: 1. H_2O is highly soluble in silicate melts and would be consumed immediately, and 2. fluid-present melt can produce only small (<2%) fractions of melt (Burnham 1979, Patiño Douce et al. 1990). Therefore, once the fluid phase is consumed, fluid-absent melting occurs because of the breakdown of hydrous phases, which in metapelite compositions are typically muscovite and biotite.

Experiments on muscovite-bearing assemblages by Connolly et al. (1997) showed how the fracture network generated by the volume change increased the rock permeability by four orders of magnitude. They were able to estimate the length and distribution of the single fractures. An example of their experiments is shown in Figure 2.3, where the white lines connecting the melt pools are melt-filled fractures that developed because of fluid overpressure.

Rushmer (2001) found that if only biotite is present (and not muscovite), the volume change related to dehydration melting is negative and melt remains trapped locally.

This work confirmed the importance of the aggregate's composition, as different dehydration reactions result in different fluid pressure variations: When only biotite is involved, melting alone is not enough to create the fracture network that favours melt migration. In this case, melt will remain in the local places where it formed until a larger amount is generated or external deformation is applied. A prolonged presence of melt caused by this mechanism could explain the existence of extremely weak layers found in collisional belts. These lithological differences therefore control the permeability development and affect the different paths that melt can take. In muscovite-bearing aggregates, thanks to the formation of higher melt overpressure, melt pathways can develop at lower melt fractions. On the other hand, melt distribution is controlled by the grain boundaries in biotite-rich assemblages, and pre-existing structural anisotropies of the host rock have a larger influence on melt distribution (Holyoke & Rushmer 2002).

The pressure changes related to the expansion of rock melting have been quantified in metapelitic lithologies by Etheridge et al. (2021) using phase equilibrium combined with Mohr-Coulomb theory. Their model showed the effect of small increments of partial melting on the fluid pressure, predicting the generated overpressure to be in the order of tens of MPa. Such values are high enough to easily fracture the solid medium in closed systems. Figure 2.4 reports one of their calculation of fluid pressure increase. The plot shows a monotone increase until a clear increment corresponding to muscovite breakdown (785°C) is reached. This spike in pressure generation is followed by another gradual growth caused by biotite. This behaviour is consistent with the experimental studies reported above and provides a useful quantitative analysis.

Fracturing does not only happen in a brittle way: if the temperature of the crust is high enough, ductile fracturing will occur, meaning that it will be time-depending, aided by crystal plasticity and creep mechanisms that cause microstructural damage (Dell'Angelo & Tullis 1988, Rutter & Mecklenburgh 2006). Weinberg & Regenauer-Lieb (2010) investigated these phenomena numerically, modelling ductile fracturing

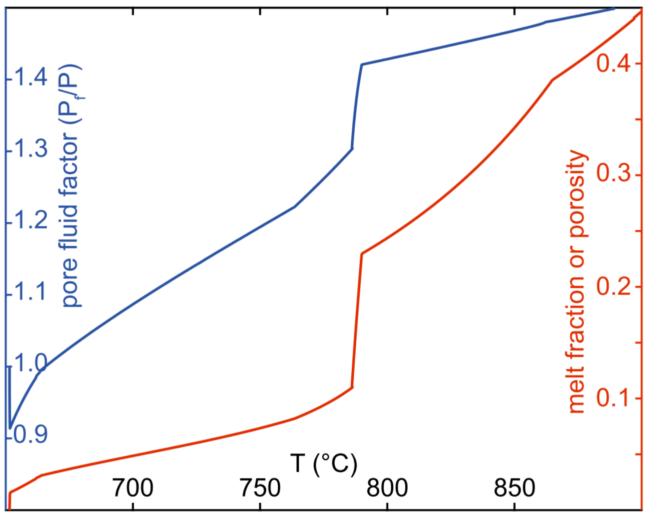

Figure 2.4: Calculation of pressure increase as a result of partial melting by Etheridge et al. (2021). Pore fluid factor (fluid pressure normalised over Pressure) and melt fraction are plotted as the temperature increases.

triggered by melt overpressure. They argue that if melt pressure at the tip of these melt-filled fractures is greater than fracture toughness, they will reach a critical length and initiate brittle-elastic dyking. Therefore, dyking is permitted by ductile fractures in suprasolidus environments (hotter than the temperature below which the rock is completely solid), while the process will switch to brittle-elastic fracturing in colder environments (subsolidus crust).

2.1.3 The Role of Deformation

Deformation is widely regarded as one of the most influential factors in the development of migmatite structures and is often considered a mechanism that enhances melt migration (e.g. Sawyer 2001, Holtzman et al. 2003, Brown 2004, Cruden & Weinberg 2018). The presence of tectonic stresses affects the style and the amount of fracturing in a partially molten rock, which is a function of the relative contribution of melt (fluid) pressure, deformation rate and deformation type (Nicolas & Jackson 1982).

If fluid pressure is high and deviatoric stress is low, the effective least principal stress shifts leftward on the Mohr diagram until it intersects the failure envelope in the tensile regime. This results in the formation of hydrofractures (Bons et al. 2022). Conversely, a high deviatoric stress combined with low fluid pressure leads to shear fracturing and fractures at an angle of ±60° with σ_3. In this case, fluid pressure does not accumulate easily as the aperture of fractures allows rapid pressure diffusion, resulting in relatively short fractures (Nicolas & Jackson 1982). When both deviatoric stress and fluid pressure contribute significantly, the failure criterion predicts fractures forming at angles between 60° and 90° commonly referred to as hybrid fractures (Bons et al. 2012). In complex environments such as melt production zones, fracture network patterns are strongly influenced by the interplay between pressure increases, stress states and the evolution of the porosity and permeability fields (Weinberg & Regenauer-Lieb 2010).

2.2 Melt Migration

Melt formation starts along grain boundaries and the liquid fraction is initially present in isolated pockets (e.g. Connolly et al. 1997, Marchildon & Brown 2002). The interconnection of melt is governed by the surface tension between the fluid and the solid crystals (Holness et al. 2011). The dihedral angles between silicate melts and rocks are typically less than 60° (Laporte & Watson 1995), enabling the formation of a network at melt fractions constituting only a few percent of the rock volume (Sawyer 2001, Rosenberg & Handy 2000, Clemens & Stevens 2016, Cruden & Weinberg 2018). Connectivity of melt and permeability of the partially molten rock have a great influence on the drainage mechanisms of the fluid phase from the host rock (Gueguen & Dienes 1989).

2.2.1 Mechanisms of Melt Migration

Melt migration from its source rock is a result of the relative motion between the fluid and solid phases (Brown 2010). There is no evidence of the existence of large magma chambers that feed structures at a shallower level (Brown 2007). Melt transport is considered to originate in partially molten sources, but the link between flow at the grain scale and the higher-level structures still needs to be fully understood (Brown

2007, Brown et al. 2011). Various mechanisms have been proposed to explain melt extraction and ascent. The main categories of these mechanisms include: pervasive porous melt flow at the mesoscale (or percolation), dyking (and hydrofractures), and diapirism (Vanderhaeghe 2009, Brown 2013).

Pervasive Porous Flow

The density contrast between melt and host rock generates pressure gradients that could allow for melt separation by porous flow (Jackson et al. 2003). However, the high viscosity of silicate melts often inhibits segregation by gravity-driven porous flow. Segregation of melt in this way might not happen within geologically reasonable timescales (Wickham 1987, Rutter & Mecklenburgh 2006, Brown 2010), unless its viscosity is particularly low (e.g. basaltic compositions, Jackson et al. 2003). Such gradients are the result of the relative rates of melt production, compaction (McKenzie 1984) and pressure diffusion (Sawyer 2001, Brown et al. 2011). Pressure gradients can also be the consequence of changes that occur with partial melting during volume changes (Connolly & Podladchikov 1998, Rushmer 2001, Brown et al. 2011, Etheridge et al. 2021). However, tectonic-induced pressure gradients are much larger than those resulting from density differences. They are thought to be one of the major forces in the mobility of melt in the crust and play a major role in the formation of networks of melt channels (Brown et al. 2011).

A schematic representation of how melt percolates inside a solid rock like a fluid flows in a porous medium is reported in Figure 2.5. The most basic models include the compaction of the matrix (as highlighted in the third panel of Figure 2.5), caused by the upward migration (segregation) of melt. This homogeneous deformation of the host rock in turn favours the upward movement of melt. The interconnection of melt at the small scale eventually develops into a permeable porosity, allowing melt flow (Brown et al. 2011).

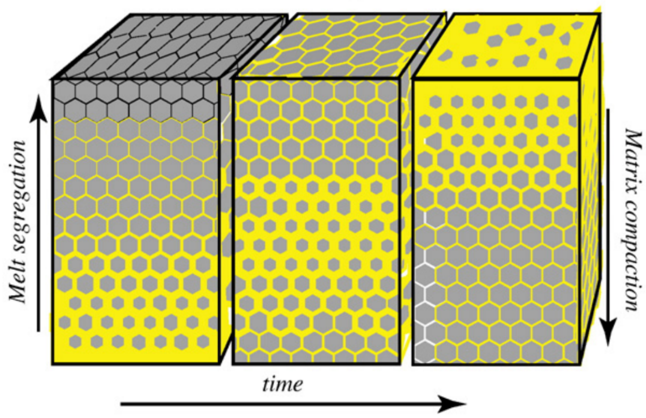

Figure 2.5: Schematic representation of pervasive flow of melt in a rock aggregate. Melt is represented in yellow. From Vanderhaeghe (2009)

Dyking

Dykes are melt-filled fractures that form primarily in the tensile regime (Mode I) and propagate perpendicular to the least compressive stress (Brown 2007). They are caused by brittle fracturing at their tip, which causes elastic deformation in the host rock. Their propagation can be explained by brittle-elastic fracture and requires a high pore pressure (from near- to supra-lithostatic, to prevent their collapse), and a minimum width and fast propagation rates to avoid freezing (Hobbs & Ord 2010, Clemens 1998).

Much attention has been given to processes such as dyking, especially of mafic composition, as they used to be considered the only type that could travel over long distances (Marsh 1982). Felsic compositions are now considered able to form self-propagating dykes, provided they reach a critical width (Clemens & Mawer 1992, Petford 1995, Weinberg 1999, Cruden & Weinberg 2018). Dykes can originate from rocks with a low melt content (e.g. Clemens & Stevens 2016). For example, it has been shown that volumes of rock are able to feed dykes through fractional melting, thanks to the gradual extraction of melt from the source rock (Harris et al. 1995).

Dyke formation has been interpret to happen by hydrofracture (Rubin 1993, Bons & van Milligen 2001, Bons et al. 2004) or ductile fracture (Brown 2004, Weinberg & Regenauer-

Lieb 2010). In the first case, fracturing is caused by internal melt pressure rather than externally applied stress. It requires pervasive melt-filled porosity and a high pore fluid pressure that leads to melt-enhanced embrittlement (Brown 2013, Etheridge et al. 2021). Hydrofractures are thought to form a small but sufficient number of dykes that drain melt from the anatectic zone (Brown 2013). The resulting system is thought to be highly dynamic and self-organised, with some authors arguing that melt extraction by hydrofracture happens in pulses rather than in a continuous way (Bons et al. 2004).

Ductile fracturing is characterised by extensive inelastic deformation caused by crystal plasticity or creep around the tip of a fracture (Brown 2004, Weinberg & Regenauer-Lieb 2010). In this area, affected by microstructural damage, fractures grow as a consequence of the coalescence of melt-filled pores (Brown 2013). The result of this process is conjugate shear bands with irregular ('zigzag') margins (Brown 2004). According to Weinberg & Regenauer-Lieb (2010), ductile fractures can reach a critical length and propagate towards shallower levels. They suggest that ductile fractures switch their propagation style as they migrate into colder and more competent crustal regions and develop into brittle-elastic dykes.

Diapirism

Diapirs consist of a volume of material that is buoyant, mobile and deformable which forces its way through a viscous medium due to their density contrast (Cruden & Weinberg 2018). Magmatic diapirs require sufficient accumulation of melt for the ascent to start. Small perturbations in the magmatic layer can form Rayleigh–Taylor instabilities, and the dominant instabilities are amplified until they form pillow-like structures that develop into diapirs. Their ascent is more efficient when the host rocks have a power-law behaviour (Weinberg & Podladchikov 1994). Faster travel rates prevent freezing and allow them to cover longer distances (Weinberg 1999).

2.3 Migmatites: Solid Rock-Melt Mixtures

Migmatites are rocks that have undergone medium to high metamorphism and heterogeneous partial melting (Ashworth 1985). They are the main sources of crustal magmas in continental environments (Cruden & Weinberg 2018).

2.3.1 Migmatite Structures

As a result of the inhomogeneous partial melting, they are heterogeneous on a macroscopic scale, with distinct parts classified as *Paleosome* and *Neosome* (Sawyer & Brown 2008). The classification of migmatites does not rely on chemical or mineralogical analysis, it is instead based on observational criteria. The *paleosome* is the part of the rock that was not affected by partial melting and therefore could still preserve minerals and structures that were present before the metamorphic event. The *neosome* is the part that was affected by partial melting and includes *leucosome* and *residuum*. The former is the light-coloured part, mainly composed of quartz and feldspars in proportions that depend on the original composition and melting conditions. The latter is the portion that remained solid after the extraction of the melt fraction, which can be partial or complete. When the predominant minerals are dark-coloured, this part takes the name of *melanosome*. An example of a light-coloured leucosome that is separated from the melanosome is shown in Figure 2.6. If the composition is ambiguous, the name attributed to that part of the rock is *mesosome*. This can refer both to the neosome and the paleosome (Sawyer & Brown 2008).

Based on how much the leucosome travels in a volume of rock, it is identified with different names, schematically represented in Figure 2.7. *In situ* leucosome is formed by fractions of melt that did not travel far from where they formed. It typically localises in dilatant structures, places of low pressure and other locations that will be discussed further in section 2.2. It can be surrounded by melanosome and can form leucosome networks when separated volumes interconnect. When leucosome moves from its original place of formation but remains frozen in the same layer of formation, it is

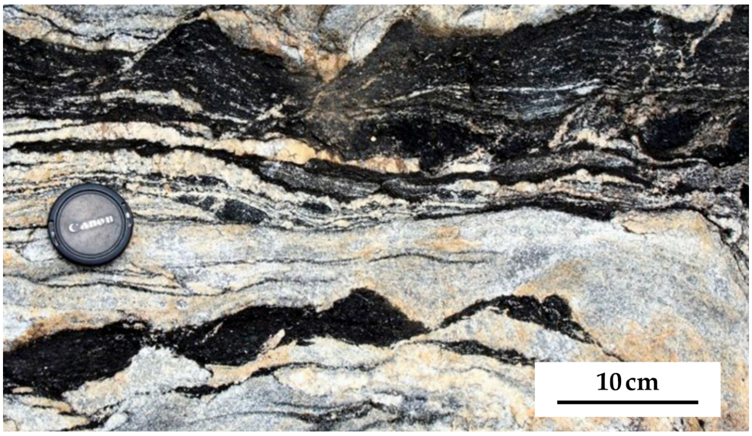

Figure 2.6: Migmatite from the Camboriú Complex, South Brazil showing a clear distinction between leucosome and melanosome. From Martini et al. (2019).

called *in source*. Finally, smaller volumes of leucosome can merge and form larger tabular bodies, which are named leucocratic veins (Sawyer & Brown 2008).

The two main classes of migmatites are metatexites and diatexites (Ashworth 1985). The main difference is defined by the melt fraction: in metatexites, the leucosome makes less than 50% of the volume of the rock, while it is the dominant phase in diatexites. If the system is closed, the melt fraction corresponds to the degree of partial melting, otherwise it is smaller. This causes metatexites to preserve their pre-existing structures, while these are usually overprinted by extensive partial melting in diatexites. This shows that the amount of partial melting is the first major factor in the structure formation. Therefore, a primary cause of differences in migmatite structures is the environment in which they form: typically, metatexites are products of contact aureoles, while diatexites form in regional metamorphic terrains (Sawyer & Brown 2008). This classification does not take into account melt migration inside a volume of rock.

Metatexites and Diatexites are further classified into second-order structures. Structures typical of metatexites include:

- *early-stage structures*, which consist of dispersed sites, sometimes referred to as nebulitic structures.

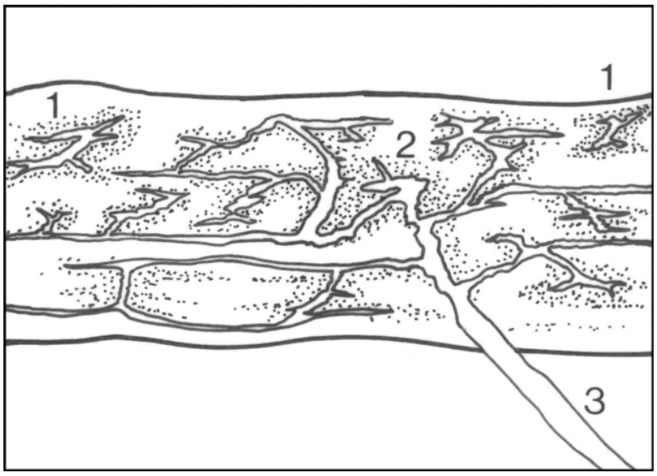

Figure 2.7: Sketch from Sawyer & Brown (2008) showing leucosome mobility. (1) represents *in situ* leucosome, (2) shows *in source* leucosome and (3) a leucocratic vein.

- *patch structures*, characterised by scattered but macroscopically visible molten areas typically formed in low-strain environments such as competent lithologies or large-scale pressure shadows. They are generally *in-situ* or *in-source*.
- *dilation structures*, formed by deformation creating localised low-pressure sites in areas such as between boudins, shear failure zones, pressure shadows or fold hinges.
- *Net structure*, created by the intersection of two or more sets of orientations, with one often parallel to the layering or foliation of the host rock and the other following shear bands.
- *Stromatic structure*, made of thin, laterally persistent layers of leucosome, which can have various origins, including compositional or deformational.

Common structures in diatexites include:

- *Nebulitic structures*, characterised by scattered remnants of paleosome. They require an absence of deformation.
- *Schollen structuress*, which form under deformation, resulting in tabular fragments of competent layers

- *Schlierien structures*, comprising thin felsic bands interspersed with thin bands of mafic minerals.

Some diatexites lack distinct morphology altogether. Structures that are not strictly linked to one type or the other are:

- *Vein-structured*, featuring leucocratic veins.
- *Fold-structured*, where folding occurred while the migmatite contained melt.
- *Layer-confined*, where melting was restricted to specific layers of the host rock.

2.3.2 Linking Melt Patterns to Processes

The classification reported in section 2.3.1 is mainly descriptive. Despite the definition of different geometric structures, they do not explain the underlying principles that control the spatial distribution of leucosome in the host rock. Only a few studies have investigated the geometric patterns of melt (Brown 2010), and linked the leucosome distribution to the mechanisms that caused it.

A common method for quantifying leucosomes or vein distribution in outcrops with layer-parallel melt veins involves measuring vein spacing and thickness along one-dimensional line traverses perpendicular to the main foliation (e.g. Brown et al. 1995, Marchildon & Brown 2003, Yakymchuk et al. 2013). This method examines the relationship between the thickness and spacing of melt veins to determine whether the layer geometry results from a self-organising system, indicated by an exponential distribution, or is influenced by external factors, such as deformation (Marchildon & Brown 2003, Yakymchuk et al. 2013).

Structures formed by melt can be analysed by mapping the two-dimensional distribution at the outcrop scale (e.g. Oliver & Barr 1997, Sawyer 2001). Spatial relationships between melt veins can be used to interpret the relative timing of anatexis relative to deformation (e.g. Oliver & Barr 1997). Three-dimensional geometries can be reconstructed using perpendicular surfaces of small outcrops (Tanner 1999, Marchildon &

Brown 2003) or X-ray tomography (Brown et al. 1999).

As discussed in section 2.2.1, melt pressure can have an active role in opening fractures in the host rock (Brown 2004, Bonamici & Duebendorfer 2010). This allows melt to migrate from its place of formation and can start the transition from a scattered distribution of melt to the formation of draining networks (Brown 2004).

Pre-Existing Structures

One of the most commonly observed phenomena is that melt tends to migrate towards places of low pressure. For example, brecciated rocks can attract melt from neighbouring places (Martini et al. 2019). They are places where rocks are broken into many smaller pieces by external forces and the volumes between the fragments are places of low pressure. Heterogeneities in the protolith are known to potentially exert significant control over melt distribution. Brown (2004) highlighted the role of pre-existing structures, observing that mesoscale melt flow tends to concentrate along foliation planes, in continuity with former architectures. The importance of such structures is well-documented; for instance, structures like foliation, layering and bedding appear to contribute to the formation of net and stromatic structures (Sawyer & Brown 2008). These planes are often exploited as 'mechanical guides' for melt (Vanderhaeghe 2001), leading to the development of layer-parallel leucosomes. Their influence is so pronounced at small scales that melt distribution may not align with the orientation of tectonic stresses (Sawyer 2001). However, despite being the preferred structures for melt localisation at the small scale, they are not thought to be efficient in the draining of melt (Marchildon & Brown 2003, Diener et al. 2014). The accumulation of melt in these areas has been observed to generate a local build-up of buoyancy, eventually leading to the fracturing of the host rock and the formation of melt offshoot veins (Vanderhaeghe 2001). The resulting structure is a continuous network of layer-parallel and larger dykes (Oliver & Barr 1997), with the latter believed to be responsible for large-scale melt flow (Sawyer 2001, Marchildon & Brown 2003, Diener et al. 2014).

Pre-existing structures (i.e. foliation and small-scale compositional layering) start to lose their influence when the melt volume becomes too extensive or other processes have a stronger effect. Larger structures are less sensitive to small-scale anisotropy (Diener et al. 2014), but are often controlled by external deformation, if present.

External Deformation

Melt geometry has been used to interpret the stress state during partial melting, as well as to understand the timing of melt relative to deformation. This includes determining whether melting occurred throughout the deformation event or during specific phases (Vanderhaeghe 2001). Evidence of synmigmatitic deformation is observed at various scales. Small structures surrounding larger leucosome layers can be used to determine the direction of shear (Maaløe 1992), while other melt structures can reveal their position relative to a larger fold (Allibone & Norris 1992). At the outcrop scale, extensional deformation creates local pressure gradients that cause melt to move towards dilatant sites such as fold hinges or boudin necks (Brown & Solar 1998, Brown 2005). The orientation of melt sheets at a larger scale is controlled by tectonic stresses and regional deformation (e.g. Sawyer 2001, Marchildon & Brown 2003) in a way that causes melt-filled fractures to have consistent orientations and form conjugate sets (Davidson et al. 1994). Field relations combined with the Mohr-Coulomb failure criterion have been used to interpret the stress field (Brown & Solar 1998). In particular, differential stress can be estimated by using the angle between melt-filled veins (Davidson et al. 1994).

The link between melt distribution and the mechanisms that were active during partial melting is key to understanding under which conditions a migmatite formed. Deformation is considered a crucial mechanism that enhances melt migration, as it contributes to localisation (Brown & Solar 1998, Hasalová et al. 2008) and the formation of fractures (Davidson et al. 1994, Petford et al. 2000). However, melt migration has been observed to occur as a porous flow within both deforming and non-deforming settings (Stuart et al. 2016, Meek et al. 2019). This suggests that melt distribution patterns in

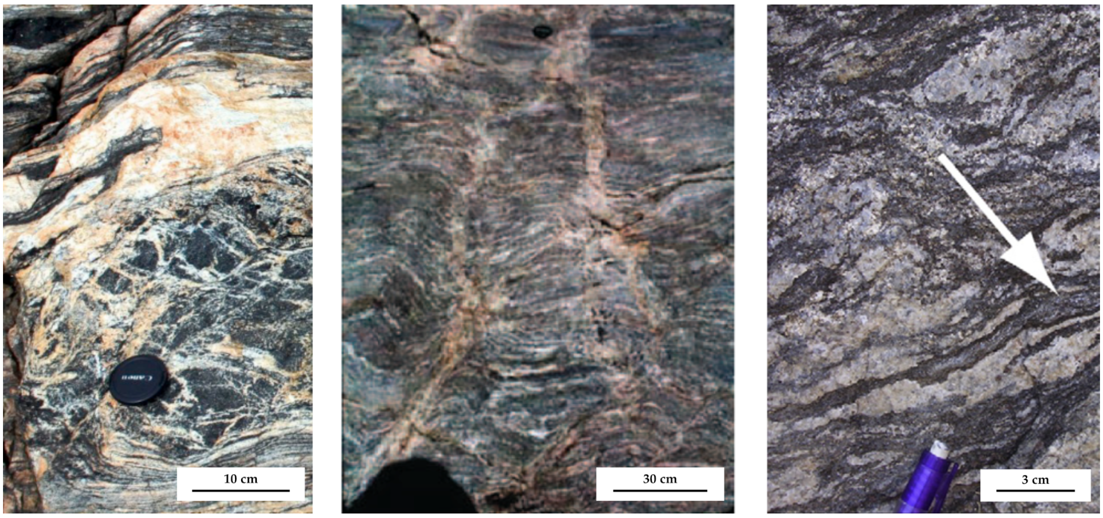

Figure 2.8: Three examples of structures that formed in different deformation regimes: completely brittle (left, Martini et al. (2019)), brittle-ductile transition (middle, Brown (2004)), completely ductile (right, Bonamici & Duebendorfer (2010))

tectonically active systems may share greater similarities with those in undeformed environments than commonly believed.

Shear zones are efficient mechanisms for melt extraction and migration (Brown & Solar 1998, Stuart et al. 2018). When melting occurs at the same time as the deformation processes, syn-anatectic structures are formed (Martini et al. 2019). In this case, it is typical to find folds or fractures filled with leucosome (Weinberg & Regenauer-Lieb 2010).

When deformation occurs in different deformation regimes, different structures can be recognised. Figure 2.8 shows two end members (first and third panel) and a transition between them. The first panel shows melt that migrated towards gaps between a rock that has been fractured in a brittle way. Brittle deformation can be recognised by the sharp edges in the rock fragments. The structures shown in the second one formed in a transitional regime and present features similar to both environments. The third figure shows wavy structures typical of ductile deformation.

2.4 Modelling Approaches

2.4.1 Numerical Methods for Granular and Porous Flow

The model chosen for this project includes a part simulating porous flow and one using a discrete element method to model the solid rock.

Models for flow in porous media were first developed in the field of chemical engineering for the simulation of fluidised beds. The two main approaches include the two-fluid and the discrete element method. The two-fluid model is a continuum approach to a system and it was first developed by Anderson & Jackson (1967). The two phases are considered interpenetrating continuum media, the conservation equations are solved on each phase separately and their macroscopic behaviour is modelled by balancing the equation of mass, momentum and thermal energy on both phases. A two-fluid model works with volume fractions: the presence of the two phases is expressed in terms of percentage in every cell of the grid. The discrete element method was first introduced by Cundall & Strack (1979). In this model, particles interact with each other, exchanging momentum and energy. They can behave elastically and transmit forces. Particles can be allowed to deform and interact with multiple other particles at the same time.

2.4.2 Numerical Modelling of Hydrofractures

Several numerical models of hydrofracturing include the fundamental processes discussed above: the elastic deformation of the host medium, fluid circulation inside host rock and cracks, and fracture growth and propagation. Many of them showed that porosity and the mechanical properties of the matrix play a major role in the initiation and propagation of these fractures (Maillot et al. 1999, Flekkøy et al. 2002, Nermoen et al. 2010, Ghani et al. 2013, 2015, Vass et al. 2014).

However, modelling fractured media is a challenging problem, especially when included in standard porous flow models. Fractures are, by definition, strong discontinuities that cannot be described by averaged approaches (Long et al. 1982). They also must take into account the interaction between the fluid and the solid in a dynamic way, as the fluid itself can be the cause of such structures and fractures deeply affect the fluid flow. For this reason, using multiple superimposed grids, each of them used to solve a different phase, can be a valid approach (Berre et al. 2019).

The model proposed by Maillot et al. (1999) is an example of this hybrid method. They focused on mode II fractures, modelling the seismic effects of fractures caused by fluid injection. Their model used a combination of a finite difference approximation for the motion of the solid medium and a lattice Boltzmann approach for the pore fluid pressure diffusion. Flekkøy et al. (2002) developed a similar method, but studied mode I fractures. Their model uses a hybrid discrete-continuum method introducing a two-way coupling between solid and fluid. The solid medium is represented by nodes connected by elastic springs, while the fluid equations are solved in a continuum grid. This approach ensures that fractures forming in the solid medium affect permeability in a realistic measure, preventing averaging effects and capturing interstitial pressure diffusion.

2.4.3 Numerical Modelling of Melt Migration

Melt migration has mainly been modelled as porous flow (McKenzie 1984, Ribe 1985, Scott & Stevenson 1986, Spiegelman 1993*a*, Connolly & Podladchikov 1998, Jackson et al. 2003, Rees Jones & Katz 2018, Maierová et al. 2023), dykes (Sleep 1988, Clemens & Mawer 1992, Leitch & Weinberg 2002, Bons et al. 2004), and diapirism (Weinberg & Podladchikov 1994, Louis-Napoleon et al. 2022).

These numerical studies provide important insights into specific mechanisms but often focus on single mechanisms. They do not model the spatial patterns resulting from complex interactions between multiple processes.

Many of the numerical methods in the literature focus on the mantle, especially the ones that use porous flow. An example is the work of Dannberg & Heister (2016), who used a finite-element model with the implementation of the McKenzie equations (McKenzie 1984) to simulate global mantle convection that includes melt migration. However, mathematical modelling of melt migration in the crust with porous flow is a relatively new approach. Recent developments have shown that the lower and middle crust (section 2.1) can have the right conditions not only to generate melt but also to make melt migration possible, without crystallisation because of low temperatures. This opens the possibility to apply these methods to these shallower regions as well.

2.4.4 Modelling with *Latte*

The code *Latte* (Ghani et al. 2013, described in detail in section 4.1.3) is based on the hybrid approach developed by Flekkøy et al. (2002). Originally designed to model hydrofractures in brittle rocks, it was used by Koehn et al. (2019) to model melt hydrofractures. In their study, the fluid phase was assigned physical parameters to reproduce the behaviour of melt and its flow was simulated on a square continuum grid. A spring network represented the host rock and its brittle-elastic response. This setup allowed the study of fault network development above a dyke, investigating parameters such as the external deformation and the Young's Modulus of the host rock.

This initial application demonstrated the potential of *Latte* for modelling melt-induced fractures, providing a strong foundation for further development. In this thesis, the code has been extended and refined to better capture the complex interplay between melt flow, fracture development, and host rock properties, making it suitable for a wider range of processes and scenarios.

Given the capabilities and limitations of the model, this thesis focuses on the first two melt migration mechanisms described in section 2.2.1: pervasive porous flow and fracturing, as well as their interaction.

Chapter 3

The Signatures of Melt Presence in the Rock Record: A Field Perspective

3.1 Introduction

Fieldwork was conducted in two distinct locations. The first study area was situated along the North-West coast of Scotland, while the second was located near Stavanger, in the southern region of Norway. Both areas are characterised by a high abundance of melt-filled dykes, with the literature suggesting that in situ melting was prevalent. In both locations, the rocks are known to be well exposed. These sites were chosen as they are good examples of locations where the presence of melt is well documented and the deformation events have been studied. However, the interaction between the two phenomena has not been studied in detail. In particular, the extent to which the observed structures are influenced by melt production versus deformation or structurally controlled remains unclear. In the first location (Scotland), the rocks are situated in an area that corresponds to a terrane boundary that has been documented as a melt-rich environment. Despite melt influx being interpreted as concurrent to the active deformation during terrane amalgamation, melt patterns are not considered to be influenced by the deformation. Similarly, the study area in Norway has been interpreted to be a high-grade metamorphic terrane where melt was present for a long time. However, the timing of melt presence and deformation and how they influenced each other remains uncertain.

In this chapter, each study location is presented in a dedicated section that includes the geological background, field photographs and relevant data. In the final section, the two areas are compared in terms of the history of melt presence and tectonic deformation. The variations in structures and geological conditions provide the basis for the different configurations used in our numerical experiments.

When taking pictures of the entire outcrop was not possible, photogrammetry was used to reconstruct images from multiple photographs. This method allowed us to create images that were perpendicular to the outcrop surfaces and avoid distortions caused by perspective. These reconstructions were made using Agisoft Metashape Standard (Version 1.8.3). Melt distributions were traced from the reconstructed images, and vein orientations were analysed using the methods described in Section 4.3.1, which were also applied to the numerical experiments, ensuring consistency between field and numerical analyses.

3.2 Melt Ingress Along a Terrane Boundary and Melt-Rich Tonalite-Trondhjemite-Granodiorite Gneisses: A Case Study from the Laxfordian Front and Rhiconich terrane, North-west Scotland

3.2.1 Geological Background

The Lewisian Gneiss Complex in the North-West of Scotland consists of tonalite-trondhjemite-granodiorite (TTG) Gneisses, locally showing mafic to unltramafic enclaves and supracrustal metasediments (Park & Tarney 1987, Goodenough et al. 2010, 2013). It is interpreted to have formed as the result of tectonic assembly of various

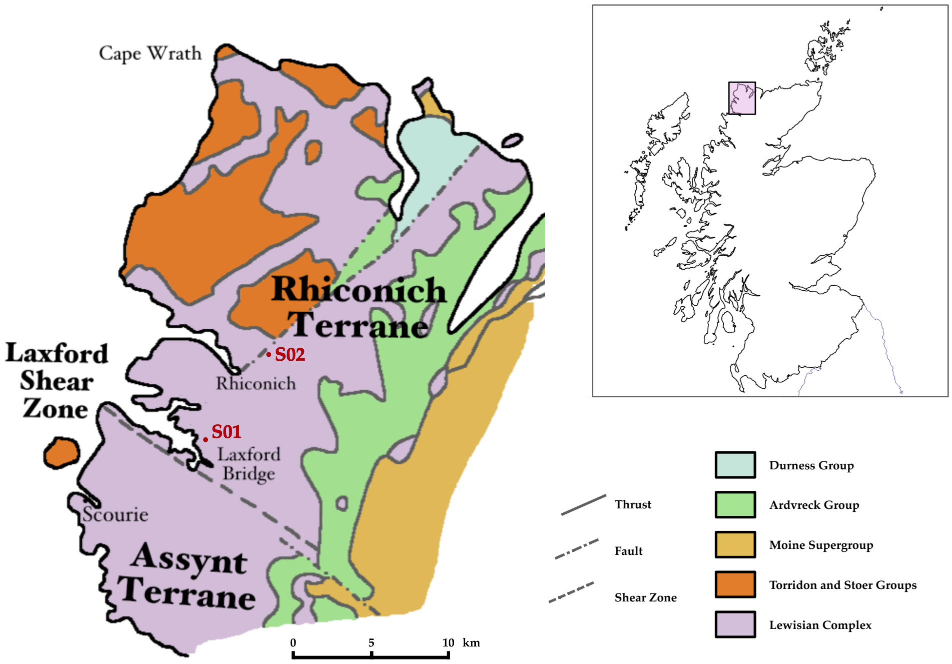

Figure 3.1: Schematic map of the region comprising the Rhiconich terrane and the Northern area of the Laxfordian terrane. The locations of the two studied outcrops are shown in red. Modified from Goodenough et al. (2010).

terranes with different origins that occurred in the Paleoproterozoic (Whitehouse 1989, Friend & Kinny 1995, 2001, Goodenough et al. 2013). A schematic map of the region is shown in Figure 3.1, together with the locations of the studied outcrops.

The locations studied in this work are situated in the Rhiconich terrane and at the boundary between the Rhiconich and the Assynt terranes. The Rhiconich terrane (Friend & Kinny 2001) consists of Precambrian basement rocks and is defined as the region between Loch Laxford in the South and the coast between Cape Wrath and Rispond in the North (Kinny et al. 2005). In general, this terrane is relatively fertile, incompetent and was metamorphosed under amphibolite facies conditions. It includes:

- TTG gneisses with mafic and metasedimentary enclaves, including discontinuous amphibolites, and small units of metasediment that are intruded by numerous granitic veins (Dash 1969, Kinny et al. 2005, Dash & Bowes 2014);

- Granodioritic TTG gneisses (*Inchard gneisses*, Kinny & Friend 1997), which constitute the largest component of the terrane;

- A swarm of mafic dykes that cross-cut structures and fabrics of the amphibolite facies (*Scourie dykes*, Park & Tarney 1987);

- Pink-coloured granitic-pegmatitic sheets (*Rubha Ruadh Granites*, Kinny et al. 2005) that cross-cut the mafic dykes (Goodenough et al. 2013). They occur in the boundary zone between the Rhiconich and Assynt terranes and were deformed under amphibolite-facies conditions. Their age has been measured to be 1854 ± 13 Ma by Friend & Kinny (2001) and 1880 ± 4.1 Ma by Goodenough et al. (2013).

- A second series of granitic sheets, which were not affected by deformation (Goodenough et al. 2013).

The Rhiconich terrane was affected by the following events:

- Laxfordian metamorphic event (c. 1903 - 1750 Ma): During this event, the Lewisian crust was buried and deformed under amphibolite-facies conditions. This event involved aqueous fluids, and produced potassic granites and pegmatite sheets. It also caused ptygmatic folding and boudinage of the Rubha Ruadh Granites (Corfu et al. 1994, Friend & Kinny 2001, Kinny et al. 2005).

- Somerledian (c. 1670 Ma, Corfu et al. 1994): also affecting the Assynt terrane, it is a further overprint.

The Assynt terrane is located south of the Rhiconich terrane. Its main TTG gneisses are relatively infertile, have undergone granulite-facies metamorphism and retrograde amphibolite- and greenschist-facies. This terrane shares the Laxfordian and Somerledian events with the Rhiconich, the two terranes have united before the Laxfordian and as a consequence of the activation of the Laxford Shear Zone between the two (Friend & Kinny 2001).

The Laxford shear zone (1.9-1.8 Ga, Beacom 1999) marks the boundary between them.

It has been interpreted as an Inverian shear zone that has been reactivated during the Laxfordian (Goodenough et al. 2010). During this reactivation, gneisses that constitute the Rhiconich terrane partially melted and underwent pervasive deformation, while gneisses in the Assynt terrane (drier and more brittle) responded by forming discrete shear zones (Goodenough et al. 2010).

The Laxford shear zone affects an area that has been divided into three sectors: Southern, central and northern (Goodenough et al. 2010). The southern and central part, which correspond to the *Claisfearn* and *Foindle zones* defined by Sutton & Watson (1950), can be considered part of the Assynt terrane; the northern part (*Badnabay zone* in Sutton & Watson 1950) belongs to the Rhiconich terrane (Kinny et al. 2005).

The main foliation to the North of the Laxford Shear Zone dips to the South-West, same as the orientation found within the shear zone itself. It starts as very steep and becomes less steep further away (North) from the shear zone (Goodenough et al. 2010). Dykes are interpreted to have intruded the area after the main deformation event in a static, low-stress environment.

Melt in the Rhiconich Terrane

The Rhiconich terrane is characterised by numerous granitic and granitic-pegmatite sheets, with a thickness that varies from 1 to 100 meters. They are generally irregular in shape, can cross-cut the original foliation and are weakly foliated or undeformed (Goodenough et al. 2010). Goodenough et al. (2013) identified two main magmatic events during the Laxfordian. The first one involves the formation of a magmatic arc, where magmas exploited old terrane boundaries as weak zones for their intrusion (1900 - 1870 Ma, also dated by Mason 2016 at 1910-1850 Ma on South Harris). Friend & Kinny (2001) found that the origin of the melt is a protolith with an age consistent with the one of the local TTGs, but it cannot be the only source for the extensive melting. Therefore, they suggest a deeper origin involving a more fertile protolith.

In the second phase, towards the end of the Laxfordian, a series of pegmatitic granitoid

Figure 3.2: Photogrammetry reconstruction of the outcrop at Location S01.

sheets have been interpreted to be the result of crustal thickening linked to a collisional event and subsequent heating (1790 - 1770 Ma). The fact that they are mostly undeformed suggests that they formed in a late stage of the Laxfordian event (Goodenough et al. 2010, 2013). The origin of such melt is not yet clear. One interpretation involves the melting of local crust and is supported by field relations described in Goodenough et al. 2013, as they are parallel to the foliation. On the other hand, experimental data from Watkins et al. (2007) claim that, based on the local TTGs geochemistry, these could not have produced enough melt to feed the late granitic sheets and therefore an external source should also be considered. In this study, we focus on the granitic sheets that formed during this second stage of magmatism.

3.2.2 Summary of Field Observations

Figure 3.2 presents an example of an outcrop featuring numerous granitic sheets. In this area, the sheets are generally coarse-grained and appear pink because of the presence of alkali feldspars. Their thickness is highly variable, ranging up to a few metres. Although the contacts of the dykes with the host rock are often irregular, a general orientation can be usually identified for each dyke in the outcrops. Most of the large pegmatite sheets are concordant with the main Laxfordian foliation and become less concordant further away from the shear zone.

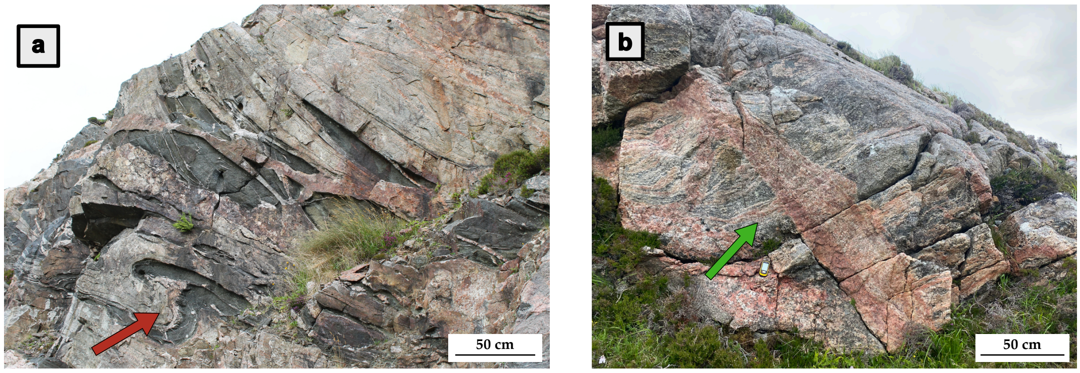

Figure 3.3: Two examples of melt structures in a location close to S01 (Figure 3.2). (a) Melt accumulating in a fold hinge, indicated by the red arrow. (b) A larger pegmatitic sheet and a cross-cut, highlighted by the green arrow.

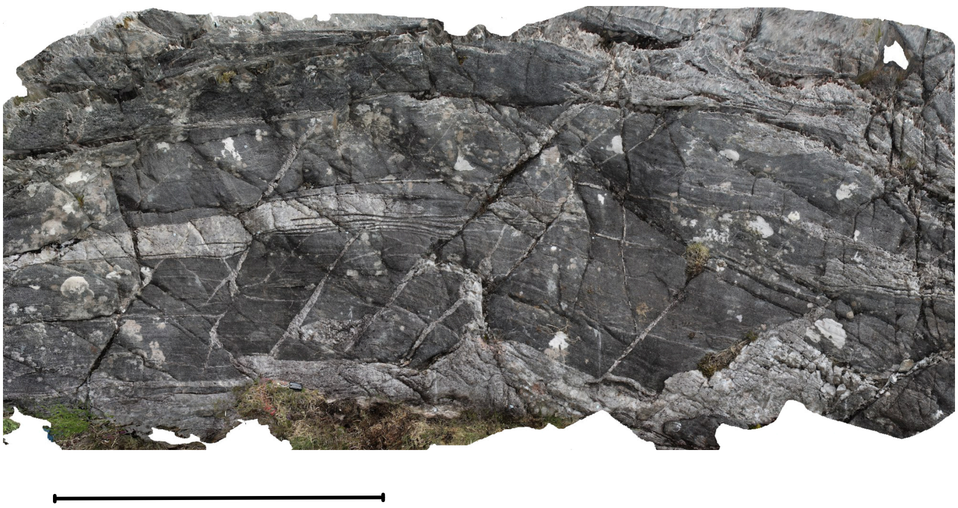

Figure 3.4: Melt fracture network observed at Location S02.

Figure 3.3 shows some structures that suggest that melt was still present when deformation was active. The outcrops are located close to the S01 outcrop. The red arrow points at a fold hinge where melt accumulated (Figure 3.3a). Many sheets are connected to smaller cross-cutting pegmatites, as shown by the example in Figure 3.3b (green arrow). Goodenough et al. (2010) suggest that the intrusive sheets were formed by partial melting and interpret the smaller bodies as feeding the larger ones.

3.2.3 Discussion

In the Rhiconich terrane, melt layers are predominantly parallel to the foliation (outcrop S02, Figure 3.4. In the Laxfordian shear zone, large dykes are more varied in their orientation, with many cross-cutting the foliation. The interpretation of these differences in melt pathway patterns remains uncertain. Goodenough et al. (2010) proposed that the contrasting geometries reflect differences in the timing of melt flux. Specifically, they suggested that the structures in the Rhiconich terrane are dominated by in-situ melting, occurring synchronously with the main foliation-forming deformation, whereas the dykes in the Laxfordian front (e.g., outcrop S01, Figure 3.2) intruded after the primary deformation event. However, whether such an interpretation can be inferred from the observed geometries remains debated. Numerical modelling that incorporates compositional variations and scenarios of syn- versus post-deformational melt generation is required to better understand the controls on melt pathway patterns. Specifically, testing conditions such as melt generation during deformation and the influence of compositional banding could provide critical insights into the interpretation of these patterns.

3.3 Layer-Parallel Melt Veins in the Rogaland Region, Norway: Interplay Between Host Rock Anisotropy and Deformation

3.3.1 Geological Background

The study area is situated in SW Norway, in the Rogaland region and is part of the Sveconorwegian orogeny. The exact location of the outcrops is shown in Figure 3.5. The metamorphic history of the Rogaland area has been typically interpreted as the result of a continent-continent collision first (with high-grade metamorphism, ca. 1050 Ma, Bingen et al. 2008, Drüppel et al. 2013), then a decompression (970 to 950 Ma, Tomkins et al. 2005) and orogenic collapse that allowed the emplacement of the Rogaland Igneous Complex (Westphal et al. 2003, Bingen et al. 2008, Blereau et al. 2017).

However, a second model (Slagstad et al. 2013) proposed an accretionary setting to account for evidence that came from magmatism (Blereau et al. 2017). Arc-like chemistry was found to be more recent than the previously suggested age for continental collision (Slagstad et al. 2013). According to this model, the accretionary margin was much more long-lived and alternated between periods of extension and compression. The accretionary events in the active continental margin took place between 1140 and 920 Ma (Slagstad et al. 2017). This active margin was involved in several metamorphic, deformational events and different phases of magmatic activity. The first phase was dated at around 1070 to 1010 Ma, with a peak between 1050 and 1030 Ma, and formed the Sirdal Magmatic Belt. In the second one, magma composition became more ferroan, probably due to different melting conditions and/or source of melt. This phase occurred from 1000 to 920 Ma with a peak between 1000 and 990 Ma and, in its later stages, is responsible for the formation of the Rogaland Igneous Complex (RIC), an anorthosite-mangerite-charnockite-granite (AMCG) complex. RIC is dated between 930 and 920 Ma, and formed a contact aureole that spans as wide as 20km.

The metamorphic history of the area is complex and possibly involves two or three distinct stages. The first interpretations consisted of a regional metamorphic event at around 1035 Ma and a high-temperature, large-scale contact metamorphic event caused by the emplacement of the RIC at ca. 930 Ma. The final stage consisted of a retrograde overprint under upper amphibolite to granulite facies (908 Ma).

However, Drüppel et al. (2013) suggested a different interpretation that involved a single, protracted regional metamorphic event. The peak of this event was dated 70 Ma prior to the intrusion of the RIC and was followed by a near-isothermal decompression phase and near-isobaric cooling. Drüppel et al. (2013) did not find any record of a second thermal pulse in the silicate mineral assemblage in the area. This interpretation was expanded by Blereau et al. (2017), who proposed a long-lived regional metamorphism characterised by high-temperature to ultra-high-temperature conditions (~850-950°C) and pressures of ~7 to 8 kbar, then a period of high-temperature

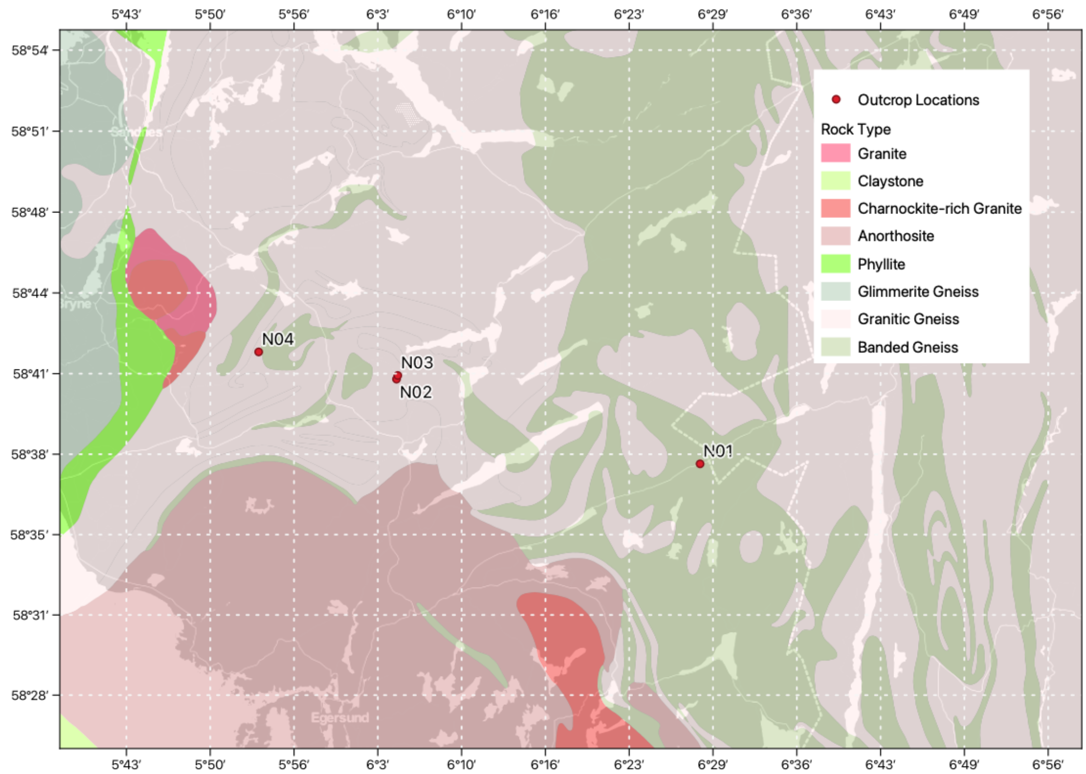

Figure 3.5: Geological map of the area and location of the studied outcrops. Data from the Norwegian Geological Survey and OpenStreetMap contributors.

decompression down to ~5 kbar. They found that rocks located up to 10 kilometres or more from the RIC contact were affected by HT to UHT caused by the subsequent emplacement of the RIC (~920 Ma). These observations are consistent with evidence that melt was present in these rocks for over 100 Ma. This event was not recorded in locations further than this area. A high temperature in the region means that a potentially large volume of melt was produced locally and remained hot for a long period of time.

The region was also affected by extensional deformation, though the exact timing is difficult to estimate due to the overprinting caused by the long-lived metamorphism. The deformation that was active in this area has been interpreted as the result of syn-orogenic and/or late-orogenic doming (Slagstad et al. 2013). It coincided with ultra-high temperature metamorphism and intrusion of the main igneous plutons.

Pre-Sveconorwegian lithologies include:

- Orthogneisses (1.5 Ga): They have plutonic and volcanic protoliths, are variably metamorphosed and often migmatitic (Bingen et al. 2005). They were intruded by mafic sheets.

- Gyadalen paragneisses (unsure age, around 1.5 Ga): Pelitic or semipelitic sediments metamorphosed at high grades (Tomkins et al. 2005, Blereau et al. 2017). Also intruded by mafic dykes.

- Granitoid Orthogneiss (1.23-1.20 Ga): intruded both the migmatitic orthogneisses and the Gyadalen paragneisses. They were not intruded by mafic dykes (Slagstad et al. 2018).

- Faurefjell metasediments (Hermans et al. 1975): include quartzite, marble, calc-silicate gneiss (e.g. 3.3.2), oxide-rich layers.

3.3.2 Locations and Melt Pathways Characteristics

This section includes some of the outcrops that were studied during fieldwork. Others are shown and discussed in more detail in later chapters.

Location N01 – *In-situ melting in pre-melt foliated rock*

The outcrop at this location (Figure 3.6) includes a metapelite with locally-produced melt showing stromatic leucosome (layer-parallel leucosome). Our interpretation is that the high melt fraction persisted over an extended period, with minimal melt movement. The melt remained within the layer where it formed, organizing itself on a small scale. There is no evidence of melt fluxing or significant interaction with the solid phase, which supports the interpretation that the melt is of local origin, generated by partial melting within the same layer.

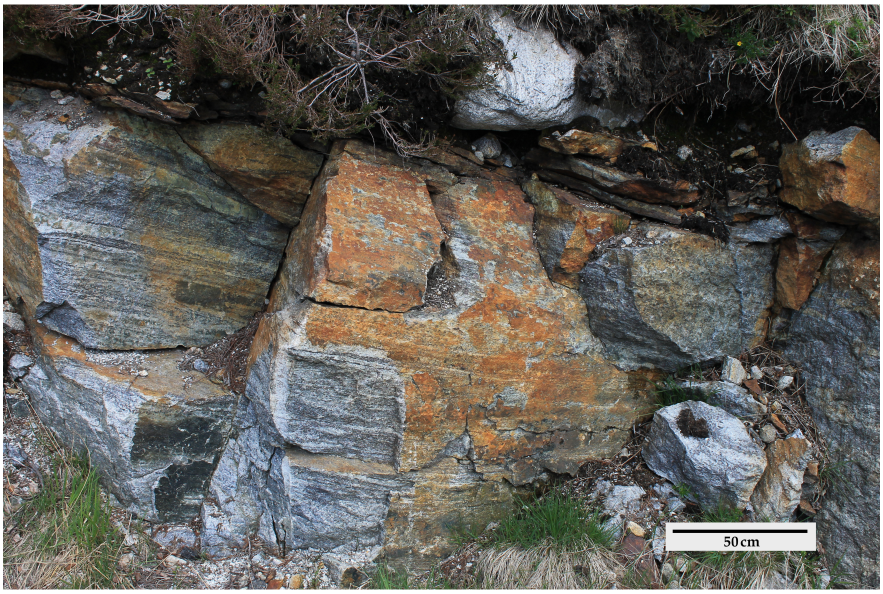

Figure 3.6: Location N01, showing foliation-parallel melt.

Figure 3.7: Faurefjell metasediments showing boudinage structures.

Location N02 – *In-situ melting in layered metasediments*

The lithology in this outcrop (Figure 3.7) consists of the Faurefjell metasediments, predominantly composed of quartz-diopside gneiss. A calc-silicate layer exhibits boudinage and displays sharp contacts with the surrounding material, which is primarily composed of quartz and feldspar. The boudins are properly separated and discontinuous, with the material between them often becoming highly quartz-rich. The presence of blue quartz, a known indicator of high-temperature conditions, is observed. These features provide evidence of high temperature and extensional deformation.

Location N03 – *In-situ melting during extension in pre-melt layered sequence*

This location also provides strong evidence of extensional deformation (Figures 3.8 and 3.9). Displacement is accommodated by structures that resemble boudins but have a different origin and have their long axes parallel to the tectonic extension. Movement occurred along the melt planes, where grains had begun to crystallise but remained lubricated by the presence of molten material. The composition is homogeneous along the shear direction. Such a structure indicates that both melt and some crystals were present during deformation.

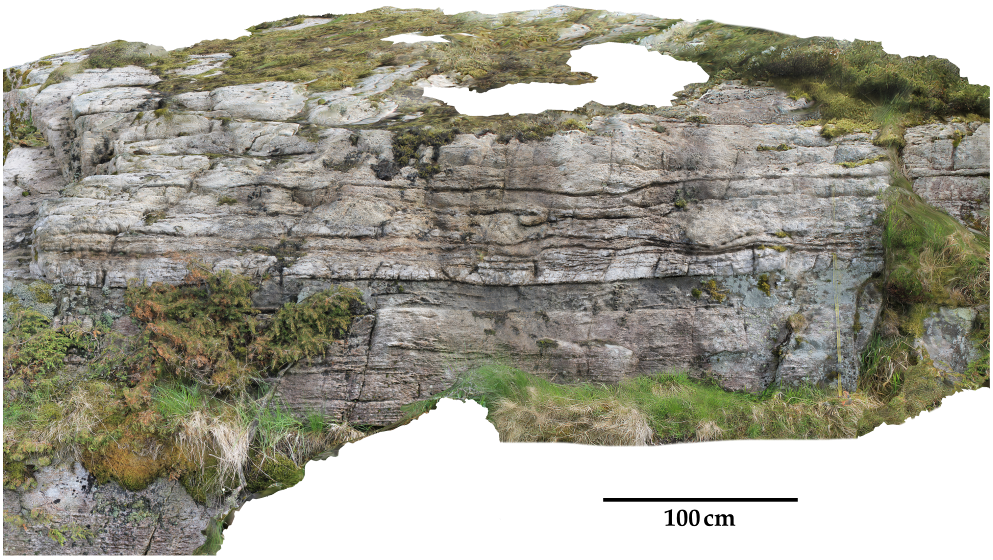

Figure 3.8: Extensional deformation structures at Location N03.

Figure 3.9: Same outcrop as 3.8, side view.

Location N04 – ***Higher melt fraction in layered sequence***

This location locally exhibits a relatively high melt fraction (Figures 3.11 and 3.12), suggesting a potential contribution from an external melt source. However, the absence of any chemical reaction between the melt and the host rock suggests that the melt source is likely nearby and shares a comparable chemical composition. While the area shows signs of deformation, the offsets are small (Figures 3.10 and 3.13), indicating that the deformation was not intense. Most melt layers in the outcrops (Figures 3.10, 3.11, 3.12 and 3.13a) are parallel to the foliation, with only a few sheets cross-cutting it. We measured the orientation of the cross-cutting veins in outcrop 4 (Figure 3.13b), and they had highly consistent orientations (Figure 3.14).

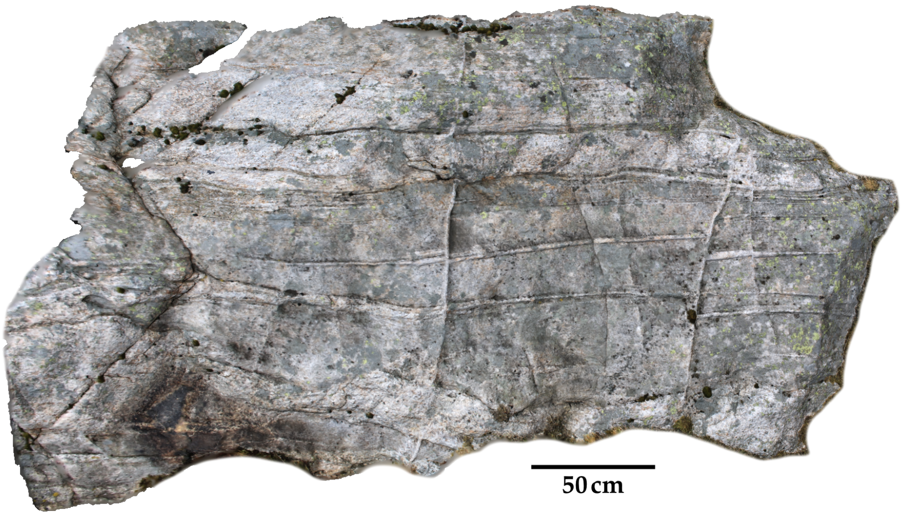

Figure 3.10: Outcrop 1 at location N04 displaying thin, foliation-parallel melt layers and high-angle discordant melt veins.

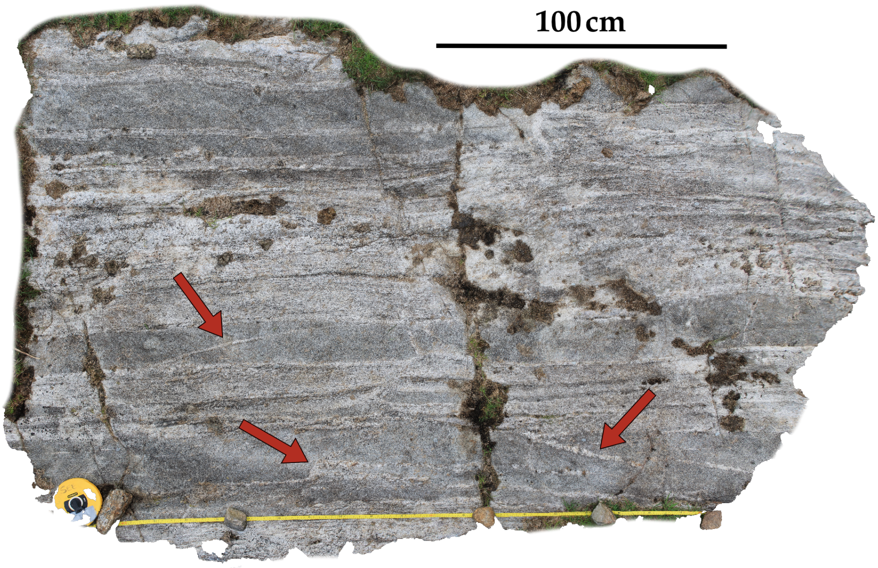

Figure 3.11: Outcrop 2 at location N04. Thicker layers of melt with smaller veins cutting through the foliation. A few examples of such veins are highlighted by the red arrows.

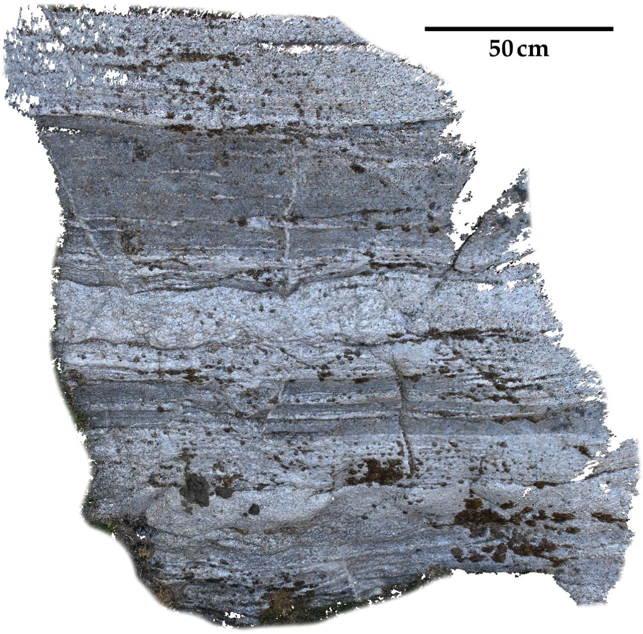

Figure 3.12: Outcrop 3 at location N04. Similar to Figure 3.11, thicker layers with smaller veins that cut through the foliation.

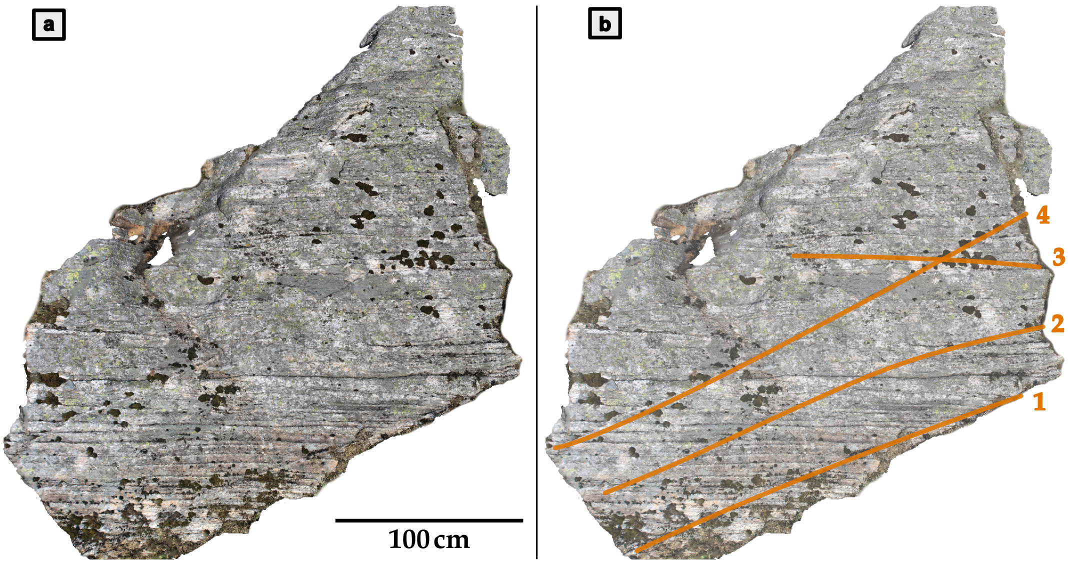

Figure 3.13: (a) Photogrammetry reconstruction of outcrop 4 from location N04. (b) Locations of the cross-cutting veins shown in Figure 3.14.

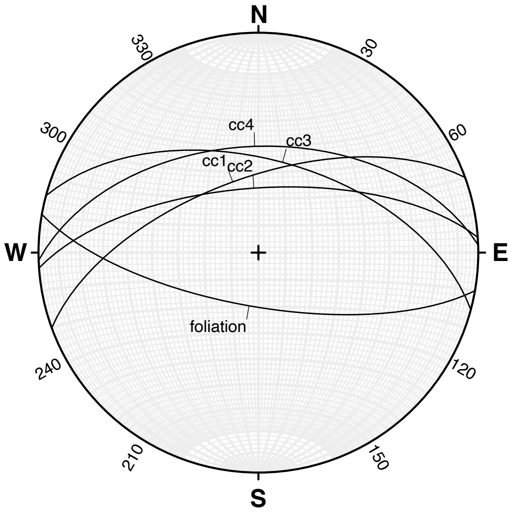

Figure 3.14: Stereonet representation of the foliation and cross-cutting planes (cc) from outcrop 4.

3.3.3 Remaining Questions Regarding Melt Pathway Characteristics and their Interpretation

While in some of the locations there is substantial evidence of extensional deformation occurring when melt was present, the extent to which this deformation influenced melt distribution remains not fully understood. At location N04, the absence of any reaction between the melt and the host rock may indicate local melting, However, the presence of significant melt volumes in some outcrops (Figures 3.11 and 3.12) suggests that melt could have originated from a nearby, external source. Therefore, it remains uncertain to what extent the resulting melt network is controlled by compositional layering or external deformation. Additionally, it is unclear whether the relative contributions of melt pressure and external deformation can be inferred from the geometric patterns of melt distribution.

3.4 Discussion

3.4.1 Comparison of Features in the Two Study Areas and the Questions They Pose

Conditions in the studied outcrops from Scotland and Norway are different. These differences are reflected in the leucosome distribution observed in the field. In the Norwegian locations, evidence from some of the outcrops (e.g. Figures 3.7 and 3.8) indicates that the rocks in the area have undergone extensional deformation. In particular, Figure 3.8 (Location N03) suggests that it was active while melt was still present. The presence of extensional deformation is also supported by what is reported in the literature (Section 3.3.1). On the other hand, the deformation is generally compressional in Scotland but the timing of the deformation is unsure. Therefore, this uncertainty suggests the following questions:

- What is the effect of external deformation on melt distribution?
- Can we understand if deformation was active from melt veins?

A big difference between the two areas is the number of veins that cross-cut the host rock anisotropy. The melt veins and dykes in outcrops S01 and S02 are quite large and can cut through the host rock heterogeneity. A few outcrops in Norway also show relatively thick layers (Figures 3.11 and 3.12), but they are generally parallel to the host rock foliation. Veins in nearby outcrops can also be fairly thin (Figures 3.10 and 3.13). Overall, studied locations in Norway show fewer discordant dykes than the ones observed in Scotland. In the area in Scotland, even if the main set of melt layers is parallel to the foliation (Figure 3.4), it still has many offshoots propagating into the background rock. These observations bring us to the following questions:

- What is the role of compositional banding? What is the interplay between deformation and anisotropic structures such as foliation and compositional layering? What determines the development of discordant veins or dykes?

Veins that do not follow the foliation of the host rock often exhibit a consistent orientation, appearing parallel to one another and creating an asymmetric structure.

- What is the explanation for their preferred orientation?

Chapter 4

Methods

4.1 Numerical Model

The code called *Latte* (Koehn et al. 2005, Ghani et al. 2013, Sachau & Koehn 2013, Ghani et al. 2015), part of the *Elle* environment (Jessell et al. 2001), was chosen for the numerical part of the project. *Latte* can simulate melt percolation through the solid phase by porous flow together with the brittle-elastic rheology of the host rock. Porous melt flow has been extensively explored in analytical studies (e.g. Scott & Stevenson 1986, Spiegelman 1993*b*, Rees Jones & Katz 2018). However, these studies typically operate at larger scales, with models that are more suitable for investigating mantle-scale processes rather than the smaller scale targeted in this work. These approaches average properties at the mesoscale, whereas our aim is to employ a method capable of reproducing microstructures with greater precision. On the other hand, *Latte* includes the benefits of modelling with superimposed grids (Berre et al. 2019) and includes the brittle-elastic behaviour of the solid phase too.

4.1.1 *Elle*

Elle (Jessell et al. 2001) is a generalised framework for the simulation of microstructures in rocks, written in C++. Initially, it was developed to model micro-processes and the

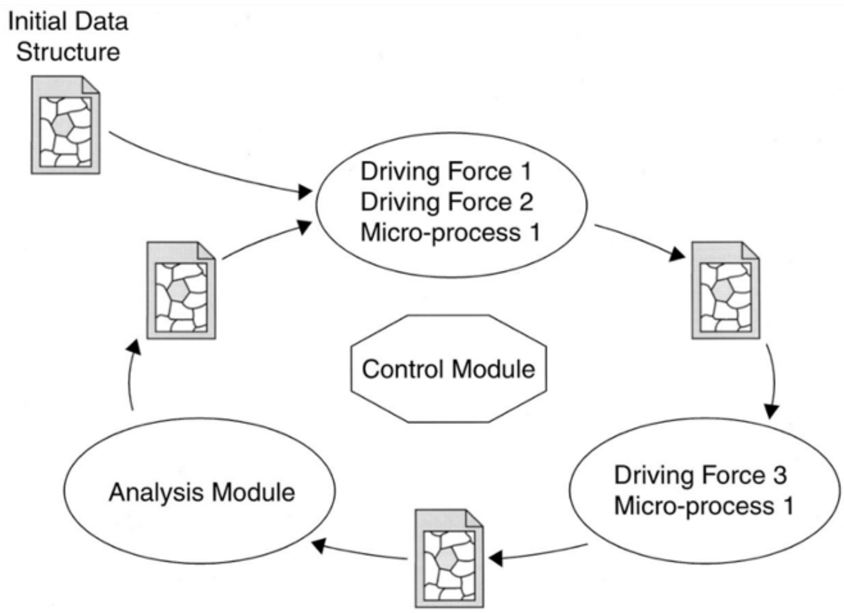

Figure 4.1: *Elle* workflow from the initial data structure to the routines calculating micro-processes (from Jessell et al. 2001).

evolution of rock microstructures at the crystal scale during metamorphism and deformation processes. The phenomena included intra- and inter-crystalline deformation. The workflow is illustrated in Figure 4.1: starting from an initial data structure, routines simulate the various processes, calculate the resulting forces and pass them to the next step. The initial data structure is the description of the spatial distribution of physical and chemical properties in the rock. Routines can be added to the system to include more processes.

4.1.2 Spring Model

Processes for simulating fracture formation were added to the *Elle* system by Koehn et al. (2005). They developed a discrete-element model able to simulate the linear elastic behaviour of rocks with the full description of the stress and strain field. The model simulates rock aggregates as a set of elements (circular particles) linked by springs, as represented in the first panel of Figure 4.2. They form a 2-dimensional, triangular lattice which is in equilibrium when all forces that act on a particle cancel

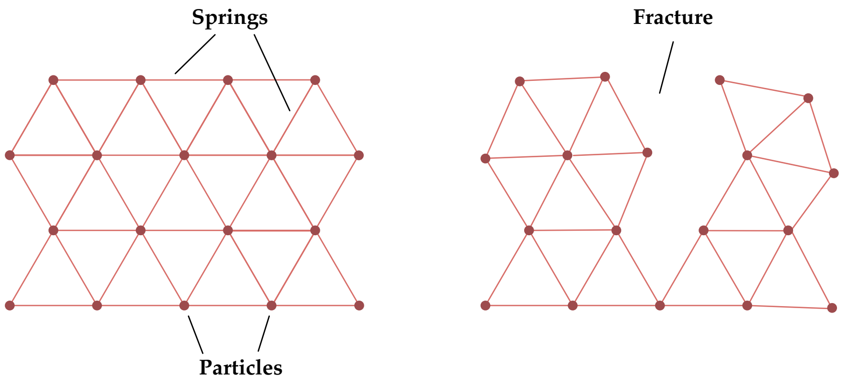

Figure 4.2: Spring model illustrating bonds (springs) between particles, particle packing and fractures (broken springs).

out. However, when equilibrium is perturbed, the spring network starts a relaxation cycle during which particles respond to the resulting forces and move until the new equilibrium position is achieved. Particle movement during relaxation is controlled by a parameter defined as relaxation threshold. Only particles that would move by a length larger than the relaxation threshold are actually moved (Malthe-Sørenssen et al. 1998).

After every relaxation cycle, all the bonds are checked: A spring breaks when a critical tensile stress is reached, as shown in the third panel of Figure 4.2. The first spring to break will be the one with the highest probability of breaking. Boundary particles are not allowed to break their bonds with their neighbouring particles. This version of the code includes the improved fracture criterion presented in Sachau & Koehn (2013).

4.1.3 *Latte*

The code *Latte* (Ghani et al. 2013, 2015, Sachau & Koehn 2013) adds a fluid phase to the lattice-spring model. Therefore, rock-fluid interactions are modelled using a combined Discrete Element-continuous approach. The solid and the fluid are solved on two separate grids, shown in Figure 4.3. The former is defined by the same grid and properties described in the above section 4.1.2: a 2-D (initially) triangular grid of

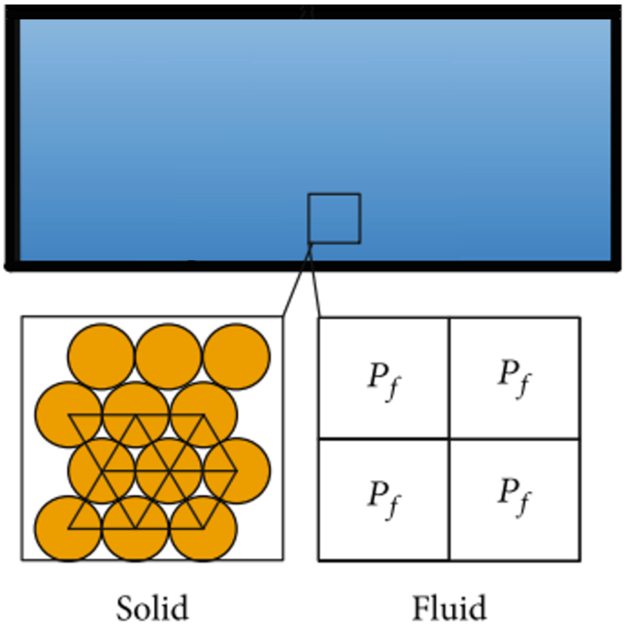

Figure 4.3: Latte's two grids: on the left, solid is simulated on the (initially) triangular grid while on the right fluid equations are solved on a square grid. Adapted from Koehn et al. (2020)

particles connected by springs. The fluid is solved on the square grid, which is twice as large as the solid one. Porosity, permeability and local particle velocities are defined and calculated on the solid grid, which passes them on to the fluid lattice.

Continuum Component

The continuity equations are solved both for the solid and the fluid on their respective grid (Ghani et al. 2013):

$$\partial_t \left[(1-\phi)\rho_s\right] + \nabla \cdot \left[(1-\phi)\rho_s \mathbf{u}_s\right] = \Gamma_m \tag{4.1}$$

$$\partial_t \left(\phi \rho_f\right) + \nabla \cdot \left(\phi \rho_f \mathbf{u}_f\right) = -\Gamma_m \tag{4.2}$$

where ϕ is the porosity, which is defined as the volume that is not occupied by particles, ρ the density (f for fluid and s for solid), u the velocity (with the same subscripts as ρ), Γ_m the melt production rate (Jackson & Cheadle 1998). The phase change (solid fraction becoming melt) was added in this study.

To calculate the local seepage velocity ϕu_f, the model uses Darcy's law:

$$\phi\left(\mathbf{u}_\mathrm{f}-\mathbf{u}_\mathrm{s}\right)=-\frac{K}{\mu_f}\nabla P \tag{4.3}$$

which includes the local permeability (K) on a unit area and the fluid viscosity (μ_f).

Permeability is defined with the Kozeny-Carman equation (Kozeny 1927, Carman 1937, 1956):

$$K(\phi)=\frac{r^2}{45}\frac{\phi^3}{(1-\phi)^2} \tag{4.4}$$

where r is a fixed grain size. This equation has been demonstrated to provide a good approximation for melt flow in migmatites (Brown et al. 1999). Equation 4.4 is used to calculate permeability in every cell of the fluid lattice except for those where a fracture is present. For these cells, an additional term is added to the base value to account for the enhanced permeability in cracks:

$$K_f=K+\phi_m K_{f0}, \tag{4.5}$$

where K represents the permeability of the cell before accounting for the presence of a fracture, ϕ_m is the porosity generated by partial melting (corresponding to the increase in melt fraction), K_{f0} a default permeability value in a fracture (10^{-15} m^2). In a porous medium, secondary permeability caused by fractures can cause the effective permeability to increase by several orders of magnitude (Berre et al. 2019) and that cannot be captured by particle movement alone. The increase in porosity (ϕ_m) is used as a proxy for the fracture aperture, as directly determining aperture is not straightforward in this type of models (Flekkøy et al. 2002). This approach to calculating permeability, which considers the variation in porosity to be caused by the opening of a fracture, reduces the resolution requirements and allows to capture phenomena occurring at scales smaller than that of the fluid grid (Flekkøy et al. 2002).

The fluid is assumed to be compressible. Its density is calculated from the density at a reference pressure ρ_0 and varies as a function of the compressibility (β) and pressure (P):

$$\rho_\mathrm{f} = \rho_0(1 + \beta P)\,. \tag{4.6}$$

The solid compressibility is considered negligible compared with the fluid compressibility, so ρ_s is assumed constant. Substituting equation 4.6 for the fluid density and Darcy's law (equation 4.3) into the continuity equation for the fluid (equation 4.2), we obtain the diffusion equation for the fluid overpressure:

$$\phi\beta\left[\frac{\partial P}{\partial t} + \mathbf{u}_\mathrm{s}\nabla\cdot P\right] = \nabla\cdot\left[(1+\beta P)\frac{K}{\mu}\nabla P\right] - (1+\beta P)\nabla\cdot\mathbf{u}_\mathrm{s}. \tag{4.7}$$

Solid Component

Solid and fluid interact at every timestep, with the solid passing the local porosity and the particle velocity to the fluid, and the fluid passing the local fluid force back to the solid. Therefore, the momentum exchange between solid and fluid for unit mass of solid (dm) in a unit volume cell (dV) is the sum of three forces (per unit area):

$$d\mathrm{m}\frac{d\mathrm{V}_s}{dt} = f_e + f_p + f_g \tag{4.8}$$

f_e being the interparticle elastic force, f_p the fluid pressure and f_g the gravitational loading.

We assume uniaxial strain, where only the vertical component (ε_1) of the strain tensor is not zero. Therefore, the vertical stress σ_1 is

$$\sigma_1 = \frac{(1-\nu)\,E}{(1+\nu)(1-2\nu)}\varepsilon_1 \tag{4.9}$$

where E is the Young's modulus and ν is the Poisson ratio. Assuming $\nu = 1/3$, $\sigma_1 = 2/3\,E\varepsilon_1$.

The elastic force for a particle is the sum of all forces applied by all connected springs.

It can be decomposed into its normal (f_n) and its shear component (f_s):

$$f_e = f_\mathrm{n} + f_\mathrm{s} = \sum_{i=1}^{6} k_\mathrm{n}^i \Delta u_\mathrm{n}^i + \sum_{i=1}^{6} k_\mathrm{s}^i \Delta u_\mathrm{s}^i \tag{4.10}$$

where k_n^i is the spring constant for the normal and k_s^i for the shear displacement. The sums are over six elements, which are the six neighbouring particles. If a spring breaks, it is removed from the model and a repulsive force is added in its place. As already mentioned when describing the spring model (section 4.1.2), this happens when the sum of strain energy for tensile (U_t) and shear (U_s) failure:

$$U_\mathrm{tot} = U_\mathrm{t} + U_\mathrm{s} \tag{4.11}$$

reaches a critical value, so that

$$\frac{U_\mathrm{s}}{E_\mathrm{cs}} + \frac{U_\mathrm{t}}{E_\mathrm{ct}} = \left(\frac{\sigma_\mathrm{n}}{\sigma_0}\right)^2 + \left(\frac{\tau}{\tau_0}\right)^2 = 1 \tag{4.12}$$

is satisfied. Here, E_ct is the critical strain energy for failure for tension, E_cs the one for shear, σ_n the normal stress, τ the shear stress, σ_0 the tensile strength, τ_0 the shear cohesion. This describes an ellipse in the $\sigma_n - \tau$ Mohr space for negative σ_n (hybrid tensile – shear fractures).

4.1.4 Partial Melting

The original implementation and set up of the code was designed for the simulation of aqueous fluids and did not account for phase transitions between solid and fluid. This functionality was added so that the model could simulate partial melting. The details of such mechanism are the following:

1. In the fluid grid, porosity increases by a quantity denoted ϕ_m (porosity caused by partial melting)

2. The solid fraction decreases by the same amount
3. Fluid pressure increases due to the larger molar volume of the fluid with respect to the solid (Etheridge et al. 2021)
4. Pressure diffusion occurs in the fluid grid
5. Information about the updated porosity and fluid pressure is passed to the solid lattice
6. The solid grid updates: it calculates the movement of the particles and the new porosity and permeability
7. Stresses are checked on every bond of the solid network. Fracturing happens when the failure criterion (equation 4.12) is reached.

Partial melting occurs in discrete points distributed throughout the simulation domain. At each time step, one or more points of the fluid grid are selected. To avoid imposing sharp gradients, a 2-D Gaussian function is applied around each chosen point, smoothing the effects across neighbouring fluid cells. If a point is sufficiently close to a domain boundary, the effect of partial melting continue from the opposite side. These processes are illustrated in figure 4.4: Panel (a) shows the increase in fluid pressure, panel (b) displays the corresponding increase in porosity. Panels (c) and (d) show horizontal and vertical profiles of the two variables, extracted along the lines indicated in panel (a).

The values of fluid pressure are taken from the calculation done by Etheridge et al. (2021) on a metapelite. Using phase equilibria modelling (THERMOCALC), they predicted the melt pressure increase as partial melting progresses. They assumed that no melt escapes from the system and that the pore fluid pressure ($\lambda_v = P_f/\sigma_{\text{vertical}}$) starts from 1 (fluid pressure is the same as lithostatic pressure). We start our simulations with some porosity already present in the system and we assume that it is filled with melt. In the low-porosity range of their $\phi - \lambda_v$ plot (3% - 10%), we calculated that the pore fluid factor increases linearly with porosity with a coefficient of 4.087 ($r^2 = 0.987$). At

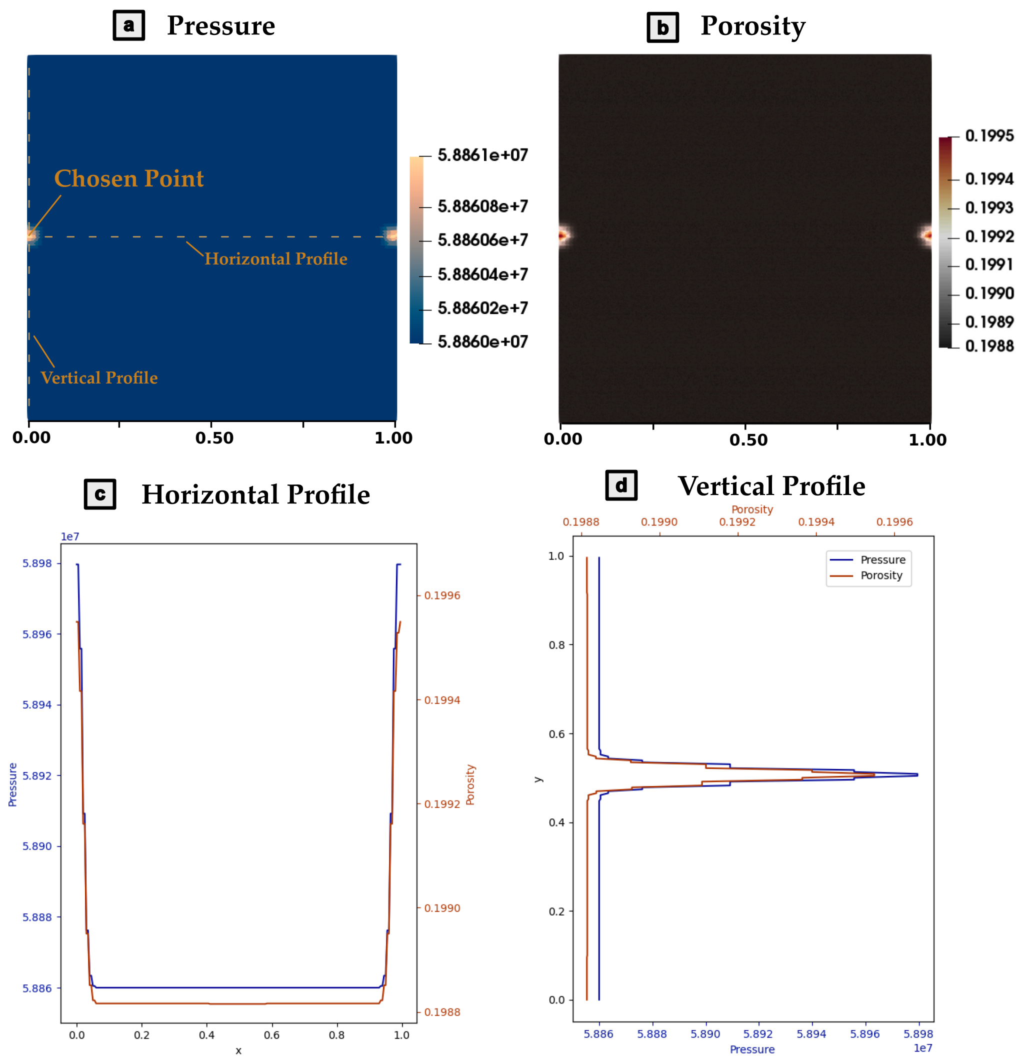

Figure 4.4: Partial melting boundary conditions. (a) and (b) Fluid pressure and porosity visualisations respectively, showing the chosen melt spot and how it continues from the other side of the domain. The two lines indicate the location of the horizontal (c) and vertical (d) profiles.

every time step in which partial melting occurs, we use this relation to calculate the increase of pore fluid factor given a discrete increase of melt fraction.

In contrast to the closed system assumption of Etheridge et al. (2021), fluid pressure in our numerical experiments can diffuse away from the spot where it formed.

4.1.5 Cloud-In-Cell Method for Updating the Two Grids

Because of the two-grid approach, some of the variables will be stored on the first grid and others on the second one. Their value is passed from one grid to the other through a tent function. Solid particles (red in Figure 4.5) are free to move in the domain and they are assigned to a square grid (black squares) whose cells are half as large as those of the fluid grid (blue cells in Figure 4.5). When values are passed from one grid to the other, a linear weighting scheme is used. Weights are calculated based on the distance between the particle (r) and the square grid node (r_0) and are used to calculate a smoothing function:

$$s\left(r - r_o\right) = \begin{cases} \left(1 - \frac{x - x_0}{\Delta x}\right)\left(1 - \frac{y - y_0}{\Delta y}\right) & \text{if } x - x_0 < \Delta x,\ y - y_0 < \Delta y \\ 0 & \text{otherwise} \end{cases} \tag{4.13}$$

where x, y are the particle coordinates and x_0, y_0 describe the position of the square grid node. This is done for 16 neighbouring cells, highlighted in grey in Figure 4.5.

4.1.6 Motivation for the Choice of the Methods

This hybrid Discrete-Element-continuum approach was chosen because melt creates fractures when it is produced and propagates. Therefore, the model needs to be able to simulate fractures in the solid phase. Fracturing is a process that works well in discrete element models while a purely continuum approach would struggle to deal with fracturing as it produces discontinuities (Bons, Koehn & Jessell 2008). The spring network model has been shown to work well to simulate fracturing in geological media (Walmann et al. 1996, Malthe-Sørenssen 1998, Malthe-Sørenssen et al. 1998, 1999).

Our goal is to model melt percolation with porous flow. When partial melting begins, melt is distributed in volumes of fluid material that are scattered throughout the host rock. By including porous into the model, melt is allowed to play an active role thanks to the of the fluid pressure.

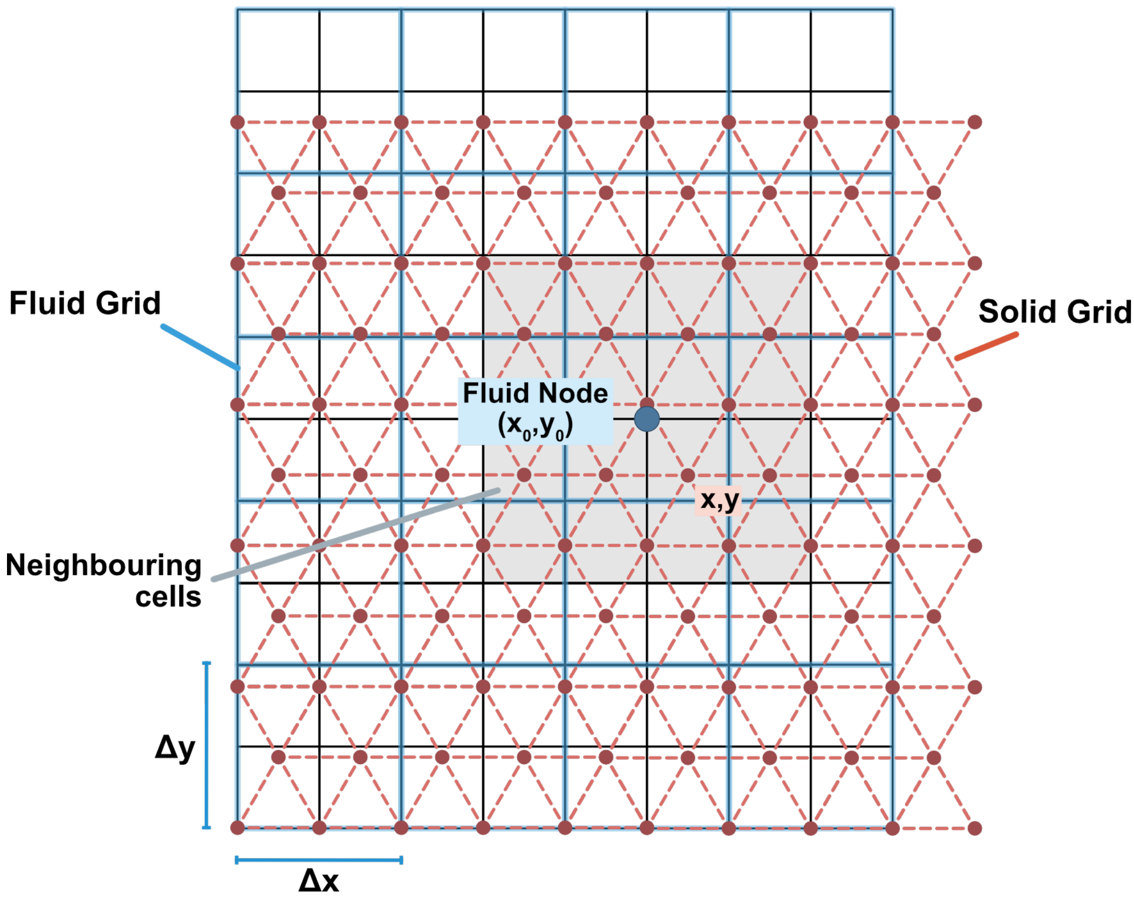

Figure 4.5: Overlapping visualisation of the two grids, including the auxiliary grid for the solid model.

Simulating porous melt flow coupled with fracture formation in the solid matrix poses significant challenges as it includes evolving porosity and permeability, dynamic fracturing and the interaction between a deforming solid and a moving fluid. While commonly used software like ANSYS products (*ANSYS Inc.* n.d.), OpenFOAM (*The OpenFOAM Foundation* n.d.) and ITASCA's PFC (Itasca Consulting Group n.d.) and UDEC (Itasca Consulting Group n.d.) are powerful in their specific fields, they are not ideally suited for this type of coupled system. ANSYS and OpenFOAM are based on continuum methods, which are optimal for systems where material properties change smoothly. However, they are more limited in the simulation of localised fracture networks and dynamic porosity and permeability fields. While ANSYS supports fluid-structure interaction, the two-way coupling remains limited, with porosity and permeability fields being only weakly coupled to the mechanical deformation. Its fracture mechanics tools are designed for systems with pre-defined crack paths or where the fracture mechanics are already known. These requirements make the software not suitable for the simulation of spontaneous nucleation and a large number of small-scale fractures. OpenFOAM presents similar limitations. Despite some implementations of fracture mechanics (e.g. Carolan et al. 2013, Lee et al. 2015, Sangnimnuan et al. 2021), its ability to simulate dynamic networks and their feedback with porosity and permeability is still limited to simple cases or geometries.

ITASCA's codes differ from *Latte* in the way that they handle mechanical interactions within the solid phase. While *Latte* represents rocks as discrete particles and interactions happen in pre-defined connections (spring network), ITASCA's implementations rely on detailed contact mechanics between solid blocks or particles. However, similar to the previously discussed models, the coupling between fluid and solid is more limited in terms of two-way feedback.

4.1.7 Assumptions and Limitations

- This model does not resolve microscale effects. This means that the model does not simulate grain-scale flow, but simulates an averaged behaviour. They are included in the mesoscale behaviour (e.g. pressure diffusion in a porous medium).
- The 2-dimensional nature of the code still captures the main features. Principal stresses σ_1 and σ_3 are aligned with the horizontal or vertical axes in the simulations.
- The model focuses on the brittle-elastic behaviour of the solid phase and does not include ductile deformation.
- The viscosity of the fluid phase is Newtonian.

4.2 Setup Differences Between Chapters

There are a few major differences in the setup parameters between Chapter 6 and Chapters 7 and 8. Compared to the first chapter, in the second and third: the Young's modulus is smaller, making the material easier to deform, the tensile strength is higher, which makes fracture opening harder, the domain is smaller, and therefore the melt spots are relatively larger.

Most of the parameter values for the numerical experiments in Chapter 6 were taken from Etheridge et al. (2021). This setup can be interpreted as a fine-grained, compositionally homogeneous rock with small melt spots. This configuration results in numerous small fractures, which tend to form clusters. The high number of small fractures corresponds to a domain saturated with high fluid pressure that makes the host rock stiff and prone to reach its failure threshold at multiple points simultaneously. In contrast, the other two chapters model a much coarser-grained rock. This material can sustain higher values of fluid pressure before breaking, resulting in fewer but larger fractures.

These changes were driven by the difficulties in imposing realistic deformation rates to the set-up in Chapter 6. When these deformation rates were applied on such a rigid and brittle host rock, they caused fast and simultaneous development of a high number of short fractures that were only the result of the applied extension. The new set of parameters promoted a more efficient localisation of fractures and allowed us to investigate the interaction between partial melting and external deformation.

4.3 Pattern Analysis in Fracture Networks

4.3.1 Topological Analysis: Key Concepts and Parameters

Fracture networks were analysed as systems of branches and nodes and topological features were used to describe the relationship between them. Topological analysis allows us to describe such networks in terms of dimensionless parameters that do not

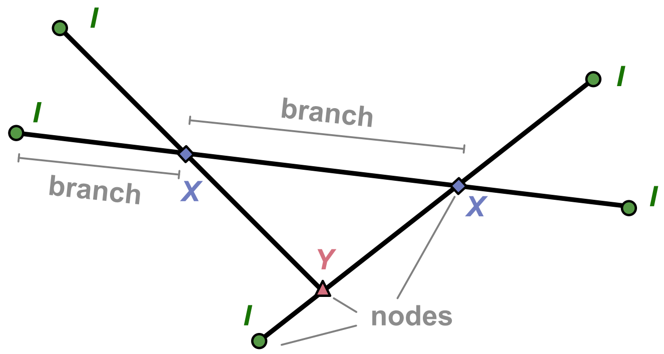

Figure 4.6: Schematic representation of the elements in a fracture network. A node is the intersection between two lines and a branch is the segment between two nodes. The different symbols represent different types of nodes: *I*, *Y* and *X*.

depend on their scale (Jing & Stephansson 1997). It also captures important features such as connectivity, which has a great influence on the permeability and transport properties of rocks.

A fracture network that intersects a surface forms a system of lines, which can be classified into nodes and branches. A node is defined as either the start/end of a line or the point where two lines cross (Figure 4.6). Each line can be divided into one or more branches, depending on how many other lines intercept it, and each branch has a node at each end (Sanderson & Nixon 2015).

Node Counting

Nodes can be of three types: *I-nodes*, *Y-nodes* and *X-nodes* (Manzocchi 2002). This classification is based on the node's connectivity: *I- type* if it is an isolated tip, *Y- type* if it ends as an abutment against another fracture, *X- type* if it is a fracture intersection (Figure 4.6). The relative abundance of each node type determines the network's connectivity, with *X-nodes* and *Y-nodes* enhancing it. Barton & Hsieh (1989) introduced a ternary diagram to easily visualise their relative abundance. Each fracture network can be plotted as a single point in the *I-Y-X* space.

Fracture Abundance and Size

In our case, information about fractures is available in a 2-dimensional space. Therefore, quantities related to fracture abundance can be normalised by the sample area to obtain the parameters defined by Dershowitz & Herda (1992). Such parameters are:

$$\text{(Areal) frequency: } B_{20} = N_B/A \tag{4.14a}$$

$$\text{Fracture intensity: } B_{21} = \Sigma L_B/A = N_B B_C/A \tag{4.14b}$$

$$\text{Dimensionless intensity: } B_{22} = N_B B_C^2/A \tag{4.14c}$$

where in the B_{xy} system x refers to the dimension of the sampling region (two in this case) and y to the dimension of the sampled feature. Here, N_B is the number of branches, L the total length of branches, A the sampled area and B_C the characteristic branch length defined as:

$$B_C = \Sigma L_B/N_B \tag{4.15}$$

which corresponds to the average length of a branch.

4.3.2 Implementation of the Fracture Network Extraction from 2-D Images

The tool developed for this thesis performs a similar type of network analysis as several existing software packages, such as FracPaQ (Healy et al. 2017), a MATLAB-based tool for analysing fracture data and quantifying parameters such as length, orientation, intensity, and connectivity; NetworkGT (Nyberg et al. 2018), a plugin for GIS software (ArcGIS and QGIS) offering similar functionality; and Fatbox (Wrona et al. 2022), a Python toolbox focused on fault and fracture network analysis. However, our implementation is specifically tailored to the format and geometry of the results from the numerical experiments and the melt network interpreted from the field images. This custom approach provides greater flexibility for our data and does not rely on external software, requiring only a small set of widely used Python libraries.

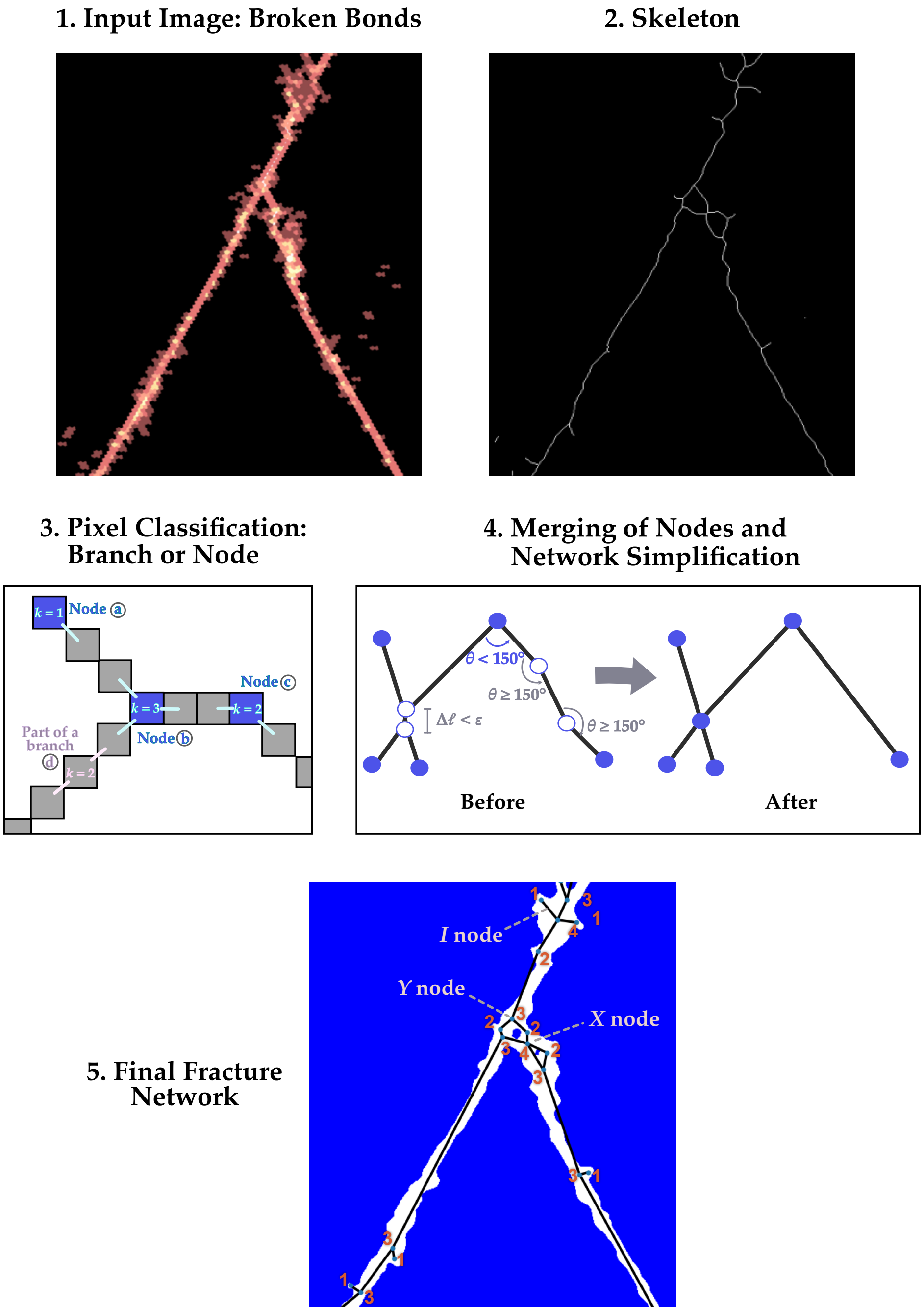

Figure 4.7: The process of network extraction from the geometry of broken bonds in a figure. (1) The input image is the spatial distribution of the particles affected by a fracture. (2) Same image after applying the *skeletonise* filter. (3) Schematic example of how nodes are identified based on their degree (k, number of neighbours). (4) Nodes are merged if their distance (Δl) is smaller than a set threshold (ε), they are removed if they have degree 2 ($k = 2$) and the angle between their two branches is greater than 150°. (5) The final version of the fracture network.

Figure 4.7 illustrates the process of extracting the fracture networks from the numerical simulations. The initial framework was adapted from the publicly available GitHub repository extract-raster-network (Vanderkam 2021), which was subsequently modified and extended to obtain the relevant parameters for the fracture network analysis.

Fractures are identified by analysing the images created by visualising particles of the solid grid that have at least one broken bond with their neighbours (Figure 4.7, step 1). The second step involves applying the skeletonisation algorithm `morphology.thin` (from the Python package Scikit-learn, Pedregosa et al. 2011). This algorithm simplifies the structure by reducing the fractures to a one-pixel-wide trace while preserving the topology of the network. Each pixel belonging to the resulting skeleton is examined based on its connectivity to neighbouring pixels (step 3). Pixels were classified as either part of a branch or a node, depending on the number of connected neighbours (degree of a node, k in Figure 4.7) and the angle between said neighbours. Pixels with only one neighbour are always considered a node, as they are one extreme of a branch (e.g. node a). Pixels with three or more neighbours represent crossings between branches, therefore they are classified as nodes (e.g. node b). The original code was edited to include pixels with $k = 2$ as potential nodes: if their two neighbours are at an angle to each other, like in case c, they are a node. Otherwise, if the neighbours form a straight line as in case d, the pixel belongs to a branch. The nodes that are identified in this phase are connected to form a graph using the Python library networkx (Hagberg et al. 2008). Step 4 consists of some operations that aim to simplify the network by merging or removing nodes. If the distance between two nodes is less than a threshold (ε), they are merged by replacing them with a new node whose location is the average of the two old nodes. In order to avoid an excessive segmentation of the network, we implemented a test on the angle at nodes with $k = 2$ to check if they can be removed. If the two branches connected to a node are almost in a line, with a tolerance of $\pm 30°$, the node is considered to be redundant and removed from the network. If the difference in orientation between the two branches is greater than 30°, this means that the node marks an important change in orientation and will be kept. An example of this process is illustrated in the right-hand side of step 4. Finally, step 5 of Figure 4.7 represents the final version of the network.

As part of the new features added to the feature extraction algorithm, nodes in the final network were classified by their degree, which is defined as the number of branches connected to the node (reported in orange in panel 5 of Figure 4.7). Nodes with a degree of 1 were identified as I-nodes, those with a degree of 3 were classified as Y-nodes, and nodes with a degree of 4 or higher were labelled as X-nodes.

4.3.3 The DBSCAN Algorithm

The DBSCAN algorithm (Density-Based Spatial Clustering of Applications with Noise, Ester et al. 1996) was used to classify fractures into clusters. The goal of the analysis is to identify fracture patterns automatically, in particular when they form elongated clusters that can serve as high-permeability channels. This algorithm is based on spatial density and defines clusters as groups of points that are close to other points. Clusters have an arbitrary shape, which is solely dependent on the spatial density of points. Points that lie in low-density areas, i.e. far from other points, are marked as outliers (“noise"). A further filter was applied, which kept only clusters consisting of at least 40 points. As opposed to other algorithms such as *k*-means, DBSCAN does not require to provide the number of clusters *a priori*. DBSCAN requires two parameters: (1) the maximum distance (ε) between two points p and q to consider p and q as neighbours and (2) the minimum number of neighbours each point needs to have to be considered a core point. If this is the case, all its neighbours are also assigned to that cluster, otherwise, it is considered noise.

The first parameter, ε, was determined by plotting the distance of each point to its k^{th} neighbour (*kNN* distance) and sorting the points by increasing distance. In this method, k needs to be the same value as the minimum number of neighbours, which was set to 10. Figure 4.8c shows the plot of the 10^{th} nearest-neighbour distances for the points associated with a fracture. Each distance between a point and its 10^{th} neighbour

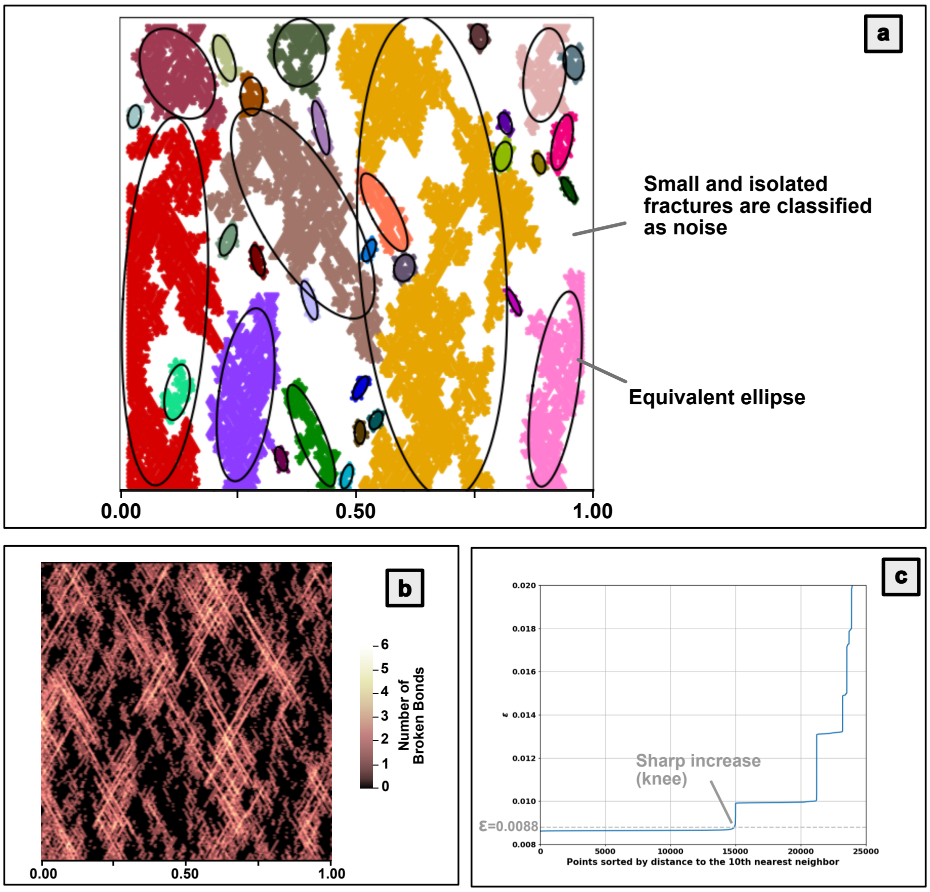

Figure 4.8: (a) DBSCAN analysis of a fracture distribution. Colours represent the different clusters identified by the algorithm. Equivalent ellipses are drawn on top of each cluster. (b): Numerical experiment showing the number of broken bonds around each particle as a representation of fractures in the host rock. $\mu_f = 10^6$, melt production rate = 0.008 per melt spot per time step. Equivalent to case a in Chapter 6, Figure 6.6. (c) *kNN* distances between a point and its 10^{th} nearest neighbour. The plot allows us to find the best estimate for the ε parameter in the DBSCAN analysis.

is calculated and sorted so that the *kNN* distances are in ascending order. Each point is a coordinate on the x axis and shows its *kNN* distance on the y axis. The optimal ε value corresponds to the start of a sharp increase in the ε parameter. In Figure 4.8c, this happens at around point number 15000 and corresponds to $\varepsilon \sim 0.0088$. Before this value, ε remains almost constant, showing that the 10 nearest neighbours of each point are all closer than 0.0088. At around this value, it is possible to observe a 'knee' in the curve. Therefore, this value was chosen to be used in the classification.

The minimum number of points is slightly higher than what is generally recommended ($2 * D$ or $2 * D + 1$, where D is the number of dimensions). This is due to the high number of points and high noise in the data.

The analysis was done using the Python package Scikit-learn (Pedregosa et al. 2011), The spatial distribution of fractures (Figure 4.8b) is given as input to the algorithm, which classifies points into separate clusters. Figure 4.8a shows the result of the analysis, where points belonging to the same cluster are plotted using the same colour, while noise (small fractures) is ignored.

Parameters such as the cluster number, size, elongation and orientation can be used to describe the fracture pattern. In order to get the shape parameters, each cluster was approximated by its equivalent ellipse (or inertia ellipse), which can be obtained from the covariance matrix, C:

$$C = \begin{pmatrix} \sigma_x & \sigma_{xy} \\ \sigma_{xy} & \sigma_y \end{pmatrix}. \tag{4.16}$$

The lengths of the major and minor axes of the ellipse are represented by the square root of the largest ($\sqrt{\lambda_1}$) and smallest ($\sqrt{\lambda_2}$) eigenvalues respectively. The orientation of the principal eigenvector represents the ellipse orientation (angle with the x axis):

$$\Theta_1 = \arctan \frac{v_{1y}}{v_{1x}} \tag{4.17}$$

where $\mathbf{v}_1 = \left(v_{1x}, v_{1y}\right)$ is the eigenvector corresponding to the largest eigenvalue λ_1 of C, adjusted for the correct quadrant based on the signs of its components.

Chapter 5

Numerical Modelling using *Latte*: Tests and Improvements

The model *Latte* has been successfully employed to simulate faulting and hydrofracture development (e.g. Ghani et al. 2015, Vass et al. 2014, Koehn et al. 2019, Aleksans et al. 2020). However, the robustness of some of its features has not been comprehensively tested in the published literature. In this chapter, we present a series of tests designed to evaluate the reliability of the code. The second part of the chapter includes improvements made to the existing version and describes adaptations implemented to extend its applicability to melt-rock systems.

5.1 Solid Grid Testing

5.1.1 Grid Resolution: Stress in the Solid Grid

Two grid configurations were used for these tests. The first grid consisted of 200 x 230 solid particles and 100 x 100 fluid cells. The second grid, with double the resolution, contained 400 x 460 solid particles and 200 x 200 fluid cells to simulate the same domain size. The other parameter that was changed was the relaxation threshold (r_t). As discussed in Chapter 4, Section 4.1.2, the relaxation threshold serves as a stopping criterion, where particles are only moved if their displacement exceeds the given r_t value. Gravity was applied in the vertical direction. The resulting principal

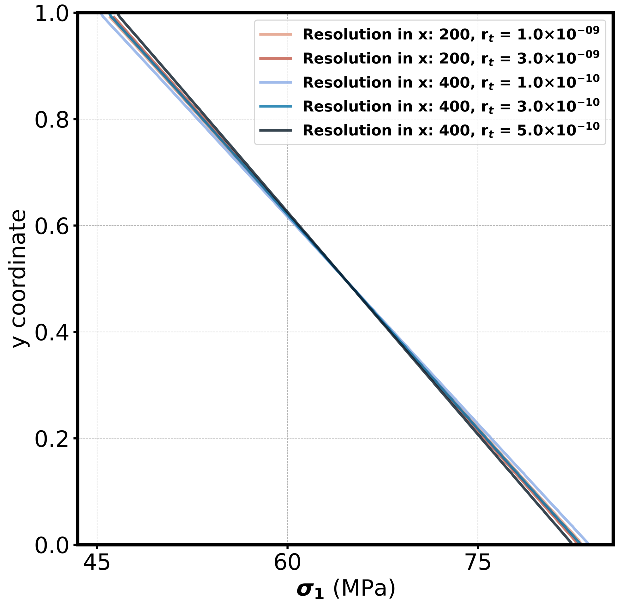

Figure 5.1: Vertical profiles of stress (σ_1) that were obtained when using two grid resolutions, 200 x 230 and 400 x 460, and different values for the relaxation threshold.

stress is reported in Figure 5.1. The plot shows the principal stress (σ_1) along the y-coordinate, with different lines representing variations in grid resolution (200 and 400 in the x-direction) and different relaxation thresholds (r_t).

The close overlap of lines across both grid resolutions and various r_t values suggests that the stress profile remains the same regardless of the grid resolutions or the relaxation threshold applied. This consistency indicates that the numerical model produces reliable stress values that are independent of these parameters.

5.1.2 Grid Geometry: Testing the Grid Anisotropy

As discussed in previous sections, the initial solid grid in each numerical experiment consists of a particle network arranged so that nodes form equilateral triangles. However, this configuration introduces anisotropy, with bonds between grid points forming angles of either 0°, 60° or 120°, potentially leading to directional differences in grid strength. The test presented in this section was performed to investigate whether this grid geometry affects fracture formation.

The triangular grid was kept the same, while two different setups, reported in Figure 5.2, were studied. In the first one, the gravitational force was applied vertically, which means that it was perpendicular to the horizontal line formed by the particles. The second case was achieved by rotating the gravitational force application by 90°. This case corresponds to having gravity acting in the horizontal direction, or parallel to one of the particle lines. During each time step of the simulations, a constant fluid pressure was added to a point in the centre of the domain. Fluid pressure accumulated, leading to fracture initiation in the host rock. Under these conditions, with gravity as the sole external force and fluid pressure injection in a homogeneous medium, fractures would be expected to align vertically.

The resulting fracture patterns are presented in the respective panels. In the first case (Figure 5.2a), the bonds in the grid are not aligned vertically and parallel to the gravitational force. As a result, it is slightly harder for fractures to form at 90°. Nevertheless, in the innermost fluid injection zone, fractures appear in a vertical orientation, forming a concentrated zone of fractured material. In this area, fluid pressure is high enough to open fractures in the tensile regime. Further from this central zone, fractures propagate at 60° or 120°, representing shear fractures opened by differential stress. This propagation is facilitated by the the alignment of certain bonds with these angles. In the second case (Figure 5.2b), a line of particles has the same orientation as the predicted orientation of tensile fractures (90°), slightly facilitating the opening of vertical fractures. There are fewer shear fractures propagating from the central region. In this case, the grid orientation does not favour the typical shear fracture angles, making propagation slightly harder.

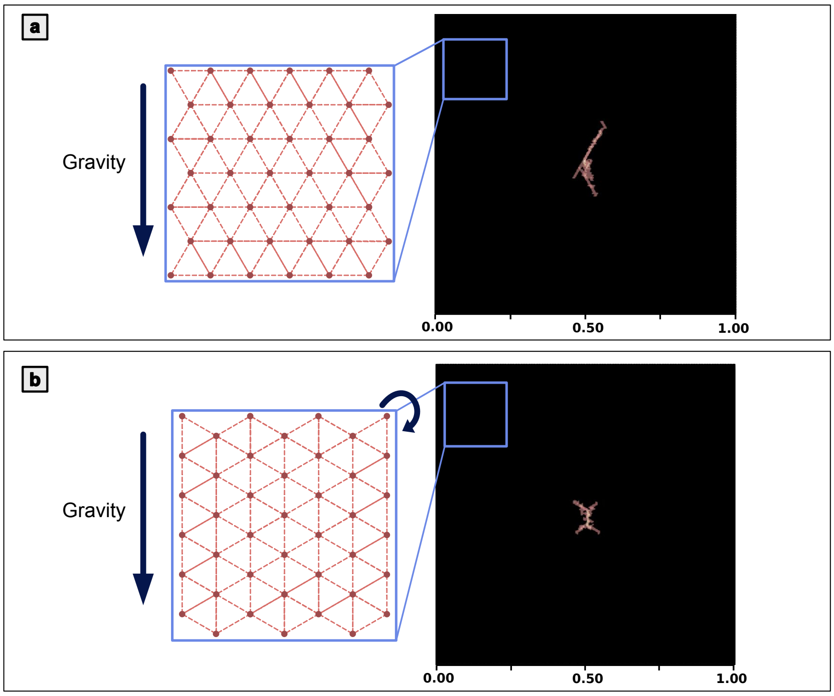

Figure 5.2: Two simulations with gravity applied along different directions of the domain.

5.1.3 Independence of Fracture Patterns from Deformation Rate

The elastic response of the solid grid occurs instantaneously and should be influenced only by the total amount of external deformation applied, rather than the rate at which this deformation is introduced. Fracture formation in a purely elastic material should remain consistent across different deformation rates if the total deformation is kept constant. To examine this, the test illustrated in Figure 5.3 displays fracture patterns produced under three different deformation (extension) rates. Time steps are chosen so that the cumulative deformation is the same across cases to allow a direct comparison.

The resulting fracture patterns appear very similar, indicating that the rate of deformation does not affect the fracture pattern. In the final panel, where the deformation rate is set to $9{\times}10^{-15}$ s^{-1}, the strain is slightly smaller, due to the approximation of the time step. However, even though some smaller fractures are absent, the overall pattern remains consistent.

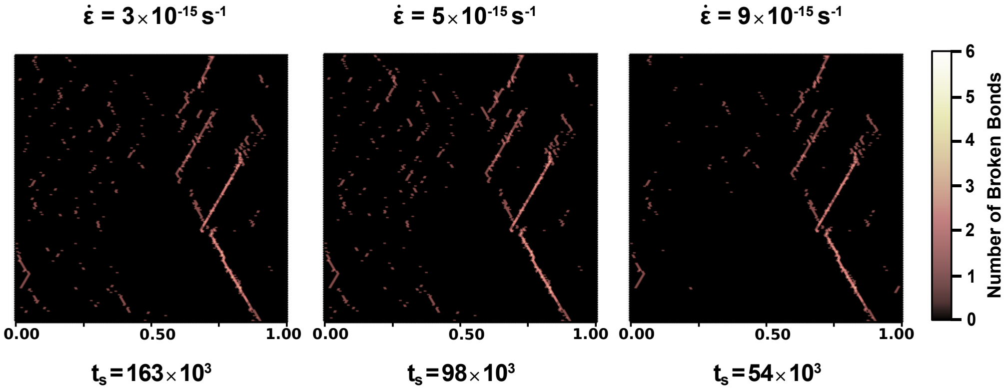

Figure 5.3: Three fracture patterns formed using three different values for the deformation rates. The time steps are chosen so that the finite strain is constant for each figure, showing that the fracture pattern is independent of the strain rate.

This behaviour is not realistic for all deformation types in natural rocks, where slower deformation rates can allow for ductile deformation. Our model simulates an exclusively elastic response in the solid medium and is applicable in systems where viscous deformation of the host rock is not a critical component. Therefore, the observed independence of fracture patterns from deformation rate is the expected result, confirming that the model behaves as predicted.

5.2 Fluid Pressure Grid Testing

5.2.1 Grid Resolution and Fluid Pressure Diffusion

Fluid pressure diffusion was tested across different domain sizes to verify that different grid steps did not affect the fluid pressure distribution.

In order to vary the simulation resolution, three domain sizes were chosen: 50, 100 and 150 metres. Since each grid contains the same number of elements, smaller domain sizes resulted in smaller grid steps and higher resolution. Figure 5.4 displays the results of injecting an identical amount of fluid pressure at the same depth across simulations with different resolutions. The fluid pressure increment was applied as an isotropic Gaussian function, with an equal spread in the x and y directions. This shape was used

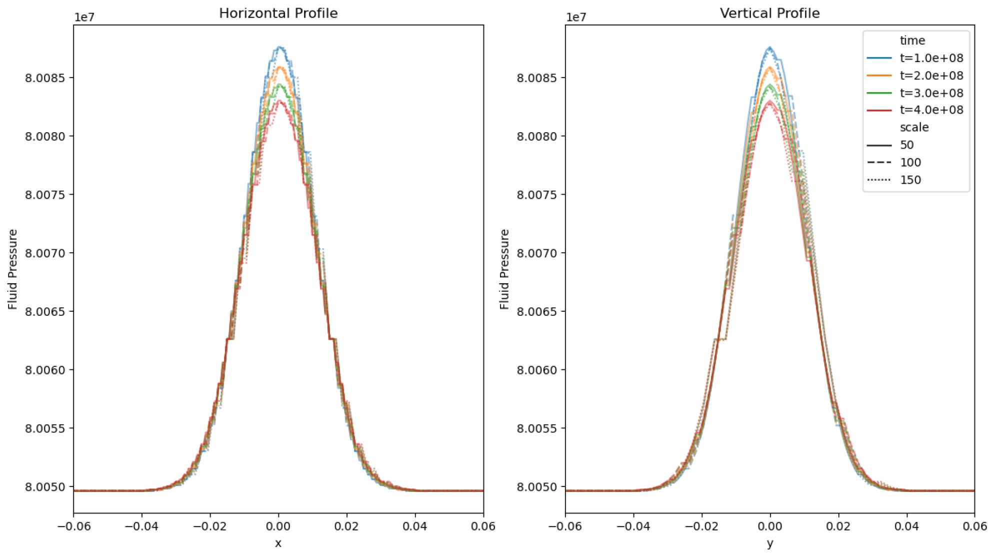

Figure 5.4: Horizontal and vertical profiles showing fluid pressure diffusion at four different timesteps when three different domain sizes (and therefore three grid step sizes) are used.

to avoid sharp contrasts between adjacent grid cells. Fluid pressure was added only once, at the start of the simulation, and as the simulation progressed, diffused with time. The plot indicates that differences between resolutions are negligible, confirming that any of the tested sizes may be used.

5.2.2 Continuous Injection of Fluid Pressure

In this test, a constant amount of fluid pressure is injected in a single point using the same Gaussian shape described in section 5.2.1. The fluid pressure increment is imposed at every time step throughout the simulation in the same spot. Figure 5.5 shows the maximum value of fluid pressure with time. Initially, the increment is fast, as pressure diffusion is still slow. As the fluid pressure increases, diffusion becomes faster until the system reaches an equilibrium between the injection rate and the diffusion rate. This is another aspect that demonstrates that the fluid pressure mechanism in the code is robust.

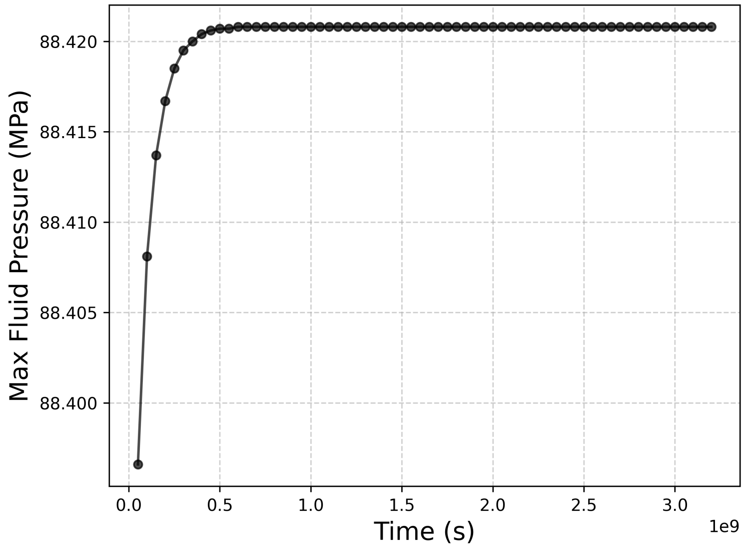

Figure 5.5: Maximum fluid pressure value as more fluid pressure is injected with a constant rate. The value increases until the rate of diffusion matches the rate of injection.

5.3 Solid-Fluid Grid Interaction

5.3.1 Improvements to the Transfer of Variables Between Grids

Some of the variables need to be transferred between grids, including porosity. Due to the geometry of the two grids, some cells in the fluid pressure grid may correspond to varying numbers of solid particles. For example, the four cells surrounding node 1 in Figure 5.6, highlighted in yellow, contain fewer solid nodes than the cells surrounding a node one or two rows below (e.g. number 2, highlighted in red). This poses a problem if a simple weighted sum is used to transfer values from particles to fluid nodes: The differences in solid particle counts are a consequence of initial discretisation rather than actual particle movement. The result is that entire rows of fluid nodes may receive artificially high or low porosity values. To address this, the system was improved by normalising values by the sum of the weights in each cell, resulting in a uniform distribution, as shown in Figure 5.6b.

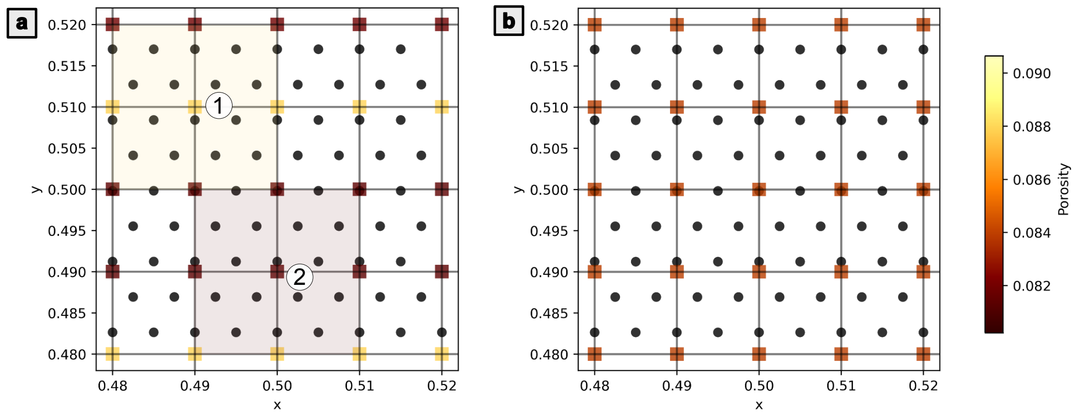

Figure 5.6: Representation of the two grids showing that some fluid pressure grid cells contain more solid grid particles (point 2) than other cells (point 1). Fluid grid cells are coloured by their porosity value, showing that the first method overestimates the solid fraction in cells where there are more solid particles because of the solid grid geometry. A weighted average produces a homogeneous interpolation.

5.3.2 Time-step Independence of Fluid Pressure Diffusion and Fracturing

A series of simulations were run with the same set of parameters but with a different time step. The chosen time step values ranged from 10^7 to 5×10^{10} seconds. In all simulations, a constant rate of pressure was added every time step so that 10^6 Pa were added cumulatively over 10^{10} seconds. Every other parameter, including the source area, was kept the same. No deformation was imposed and we chose not to increase porosity (unlike partial melting processes) in order to keep the study as simple as possible. To check if the time step had an influence on the results, the time of the first fracture was considered for all of the time steps. Figure 5.7 reports how long the numerical experiments had to run before the first bond was broken. Time steps from 10^7 to 10^9 showed a very similar time at which the first fracture occurred. On the other hand, time steps greater than 5×10^9 seconds showed an increasingly long time before the first bond was broken. This can be explained by the way that the code is structured. In a time step loop, the relaxation and check for failure happen after diffusion. Larger time steps favour pressure diffusion, making it more difficult to reach the conditions for fracturing.

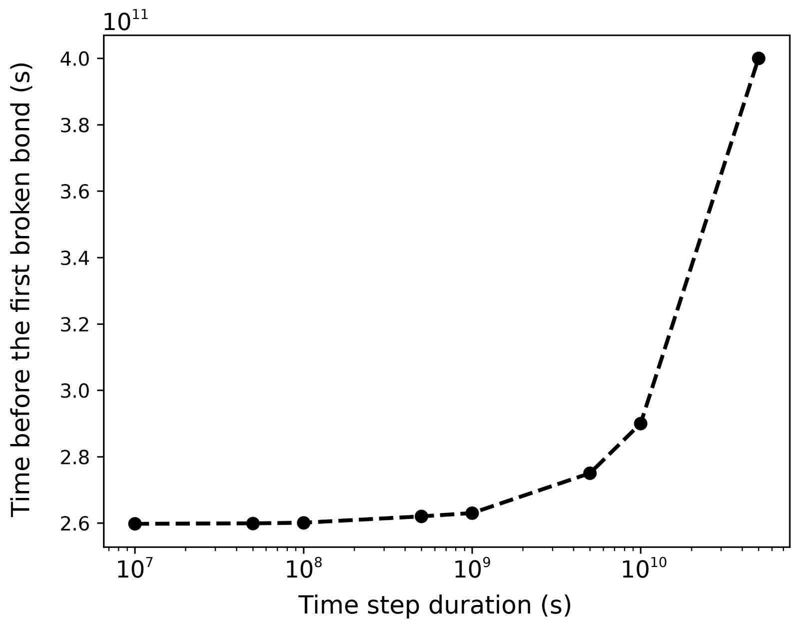

Figure 5.7: Time elapsed before the occurrence of the first fracture in simulations with different time steps. Fluid pressure is increased at a constant rate, fluid viscosity = 10^6 Pa s.

5.4 Model Performance Improvements

The relaxation routine was identified as the part of the code that took the longest to run. To improve the efficiency of the code, it was parallelised using OpenMP, allowing the workload to be distributed across multiple threads. The results of this implementation are presented in Figure 5.8. Panel (a) shows the code's performance, measured by the time interval between the generation of successive output files. The slowest performance is observed when no parallelisation is used (blue line) while increasing the number of threads resulted in faster execution times. For instance, running the code with two threads increased the speed by approximately 38%. With 16 threads, the execution speed was nearly four times faster than the original, non-parallelised version.

To verify that the parallelisation does not alter the simulation outcomes, the same test simulation with identical parameters was run using varying numbers of threads.

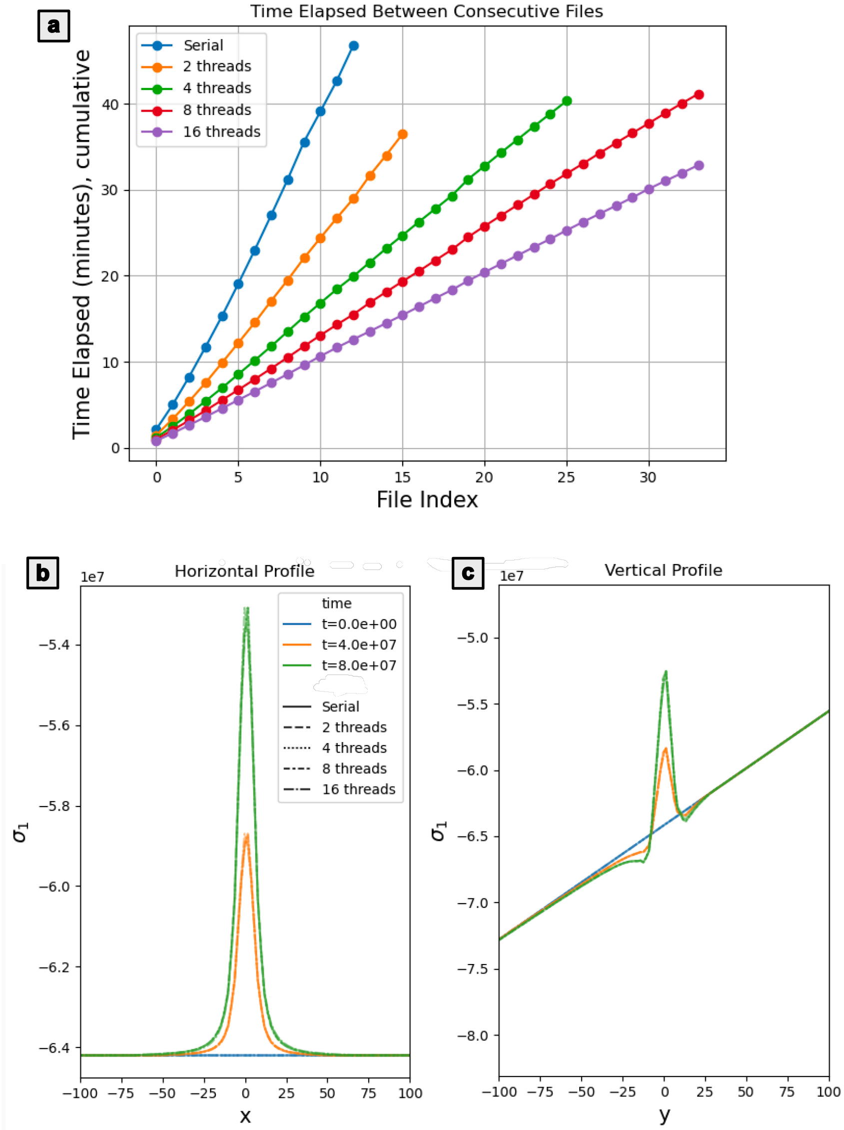

Figure 5.8: Results of the parallelisation of the relaxation routine. (a): time between the creation of consecutive files as a measure of the code speed. Different colours represent the number of threads used. (b) and (c): horizontal and vertical profiles of stress σ_1, showing that using parallelisation does not affect the results.

Panels b and c in Figure 5.8 show the horizontal and vertical stress (σ_1) profiles, respectively. As the resulting profiles are very similar across all cases, we can conclude that the parallelised code produces values that are consistent with the original implementation and therefore can be used to achieve the same results with improved performance.

Chapter 6

Using the Geometry of Melt Pathways within Partial Melting Zones to Assess Melt Production Rates and Melt Viscosity: Insights from Numerical Modelling

6.1 Introduction

The production and migration of melt are key processes in the Earth's lower and middle crust (e.g. Vanderhaeghe 2009). For example, these mechanisms greatly influence crustal chemistry by causing differentiation of the continental crust, which becomes more mafic and less hydrated in its lower portion and more felsic and hydrated in its upper portion (Brown & Rushmer 2006, Brown 2013). They also have a significant impact on rheology, as the presence of melt greatly reduces the strength of the crust (e.g. Van der Molen & Paterson 1979, Rushmer 1991, Vanderhaeghe 2009). Melt produced at these levels can leave its place of production and become the source of most magmatic bodies found at a shallower depth such as the upper continental crust (Cruden & Weinberg 2018). However, the effect of these processes depends on the spatial distribution of the melt fraction, and its connectivity is one of the major factors determining the ability of the melt to migrate to shallower levels. The geometry of the melt fraction strongly depends on the conditions during melt generation and migration, suggesting that melt patterns could be used to decipher the active processes at the time. However, the link between such mechanisms and the resulting melt geometric patterns is still not fully understood.

6.1.1 Melt Production Zones

Melt production zones are areas where pressure and temperature conditions cause some minerals to undergo a phase change from solid to fluid. Such conditions are often reached when mantle-derived magma provides enough heat, but they can be helped by a combination of radioactive heat production, mechanical processes (shear heating, viscous dissipation), latent heat and decompression (Brown 2013).

Crustal melting starts along the grain boundaries of a solid mineral aggregate (Brown 2004). It can happen in response to three main types of metamorphic reactions: fluid-present ('wet') melting, hydrate-breakdown melting and anhydrous melting (both fluid-absent). During wet melting, aqueous fluid enters the area and triggers local partial melting; this allows crustal rocks to melt at relatively low temperatures (650°C, Etheridge et al. 2021). This process is limited by the small quantities of aqueous fluid available in subsolidus crustal rocks so it is responsible for the first ~1% of melting (Etheridge et al. 2021). Therefore, most of the melt production happens under 'dry' conditions, due to either a temperature increase or a pressure decrease, in particular with the breakdown of micas (White & Powell 2002). However, different rock types and conditions can involve different reactions, which produce a different amount of melt at different rates (Powell et al. 2005, Rushmer 2001). According to the work of Etheridge et al. (2021) on a pelitic composition, the first stage of fluid-absent melting in such rocks ranges from ~650 to ~785°C and produces approximately 10% melt. A further increase of only a few degrees causes the consumption of the remaining muscovite, which triggers the production of another 10% melt. Once the temperature is above 800°C, melting occurs as a consequence of biotite breakdown and produces approximately 5% every 20°C.

Fluid-absent partial melting can cause an increase in the volume of the mineral-melt assemblage (Clemens & Mawer 1992, Connolly et al. 1997, Rushmer 2001) and, as a consequence of their confinement, results in local melt overpressure. This causes a decrease in the host rock's effective normal stress equal to the fluid pressure value (Terzaghi's principle). Once the increase in fluid pressure is high enough, it triggers the aperture of fractures in the host rock (Clemens & Mawer 1992, Bons et al. 2004, Bons, Druguet, Castaño & Elburg 2008, Brown 2004, Etheridge et al. 2021). Fractures can propagate and develop into a network, the extent and geometry of which play a crucial role in melt migration (Petford 1995).

6.1.2 Melt Migration

During the initial stages of partial melting, melt is typically found in isolated pockets. As the volume of melt increases, it can become mobile and eventually leave its original location (Diener & Fagereng 2014). In the case of a homogeneous rock not subjected to tectonic deformation, the key parameters controlling melt flow are the relative rates of melt production and melt pressure diffusion (Brown & Solar 1998, Sawyer 2001). Partial melting increases melt pressure, while diffusion facilitates the drainage of melt and reduces melt pressure. As a result, these processes play a crucial role in determining the rate of melt pressure accumulation, which can lead to fracture formation (Etheridge et al. 2021). When fractures form, they significantly influence melt mobility and segregation, especially in the early stages of melt extraction from the source rock (Petford 1995, Clemens & Mawer 1992, Brown 1994, Rushmer 2001). In particular, the degree of fracture connectivity is crucial in determining melt migration, as a well-connected and continuous network can transport melt efficiently (Petford & Koenders 1998). Evidence of this can also be found in the high number of melt-filled veins that develop in volumes of rock affected by partial melting. However, few studies have attempted to correlate their geometry with the conditions under which they formed.

One of the main physical properties that control pressure diffusion is melt viscosity. It can span several orders of magnitude and is a function of properties such as composition, temperature and volatile content (Brown et al. 1995, Hack & Thompson 2011). Typically, it can be estimated within an order of magnitude based on laboratory and/or numerical experiments (e.g. Bottinga & Weill 1972, Shaw 1972, Nicolas & Ildefonse 1996). The rate of melt production is affected by many factors. Some of them depend on the protolith properties, such as the rock composition and fertility, the amount of available H_2O, and the grain size. Other factors are related to the supply of heat (Etheridge et al. 2021, Daczko & Piazolo 2022), such as the magnitude of heating, time scale, heat source temperature and protolith conduction. Finally, they can be related to tectonic movements, such as decompression rate, and strain rate (Thompson 1999, Rutter & Neumann 1995). However, assessing production rates from field observations is a major challenge.

6.1.3 Migmatite Classification

Migmatites are rocks that comprise a formerly molten component (leucosome) and a metamorphic component that mainly remained solid. Our knowledge of partially molten rocks in the crust is largely derived from field-based studies (e.g. Nicolas & Jackson 1982, Maaløe 1992, Weinberg & Sarle 1998, Sawyer 2001, Bons, Druguet, Castaño & Elburg 2008, Marchildon & Brown 2002, Bons et al. 2009), and augmented by numerical modelling (Petford & Koenders 1998, Leitch & Weinberg 2002, Bons et al. 2004, Diener & Fagereng 2014). Migmatites have been classified based on observational criteria. Two main classes have been defined as first-order morphologies: metatexites and diatexites (Ashworth 1985, Sawyer & Brown 2008). In this type of classification, the criterion is the melt content: metatexites usually have less than 50% melt, while diatexites contain more than 50%.

Following the classification in Sawyer & Brown (2008), metatexites and diatexites can be further divided into second-order structures. Metatexites can have nebulitic, patch, dilation, net and stromatic structures, while diatexites can have nebulitic, schollen and schlieren structures or be without a distinct morphology. Types that are not linked to either primary classification are vein-structured, fold-structured and layer-confined migmatites. Despite the definition of these classes, the underlying principles that govern the spatial distribution of the leucosome remain uncertain. These distinctions refer to the geometric relations but do not focus on the processes that led to their formation. The mechanisms identified as important in this type of classification are features of the protolith (competent/deformable, fertile/infertile) or dictated by external stresses (pressure shadows).

Another way of describing a migmatite is based on how much the leucosome (i.e. former melt) has travelled in a volume of rock (Sawyer & Brown 2008). *In situ* leucosome is formed by fractions of melt that did not travel far from where they formed. It can be surrounded by melanosome and can form leucosome networks when separated volumes interconnect. When leucosome moves from its original place of formation but remains frozen in the same layer of formation, it is called *in source*. Finally, smaller volumes of leucosome can merge and form larger tabular bodies, which are named leucocratic veins. Again, the criterion does not involve causes and mechanisms of melt movement but only how extensive it was.

6.1.4 Modelling Approaches

Melt migration in the lower crust has mainly been modelled as porous flow (McKenzie 1984, Ribe 1985, Scott & Stevenson 1986, Spiegelman 1993*a*, Connolly & Podladchikov 1998, Jackson et al. 2003, Rees Jones & Katz 2018, Maierová et al. 2023), dykes (Sleep 1988, Clemens & Mawer 1992, Leitch & Weinberg 2002, Bons et al. 2004), and diapirism (Weinberg & Podladchikov 1994, Louis-Napoleon et al. 2022). Most modelling approaches only consider one mechanism for melt migration, e.g. melt percolation through porous flow or in discrete fractures. In this study, we use numerical modelling to combine porous flow with host rock fracturing and investigate the complex interactions between the two processes. We focus on the effects of local partial melting on the host rock, linking the rate of processes to the geometry of melt-produced fracture networks. We vary melt production rate and viscosity to show the relative importance of fluid (melt) pressure accumulation and diffusion. Our results show that these rates are critical in determining the fracture pattern. When melt production is the dominant process, fluid pressure quickly accumulates and generates highly developed and well-connected fracture networks. If diffusion is efficient, only small cracks form and melt migration occurs mainly as porous flow. We quantify the fracture patterns using network analysis based on fracture abundance, connectivity and clustering.

6.2 Methods

6.2.1 Numerical Scheme

The numerical experiments were performed using the 2-dimensional model called *Latte* (Koehn et al. 2005, Ghani et al. 2013, Sachau & Koehn 2013, Ghani et al. 2015), which is part of the *Elle* environment (Jessell et al. 2001, Bons, Koehn & Jessell 2008). The system comprises only a solid phase (i.e. the host rock) and a fluid phase, which corresponds to the melt fraction. For this reason, 'melt' and 'fluid' are used interchangeably in this work. Melt content is represented by the porosity and therefore described in the model as a fraction of 1. The numerical scheme uses two grids, one for each phase: the fluid pressure is solved using a continuum model and the solid phase is simulated by a DEM (discrete element model), making it a 'hybrid' model. Any other phases are ignored, and melt behaviour is assumed to be Newtonian.

Fluid Pressure

Melt is represented by the fluid pressure and is solved on a square grid using porous flow:

$$\partial_t \left[(1-\phi)\rho_s\right] + \nabla \cdot \left[(1-\phi)\rho_s \mathbf{u}_s\right] = \Gamma_m \tag{6.1}$$

$$\partial_t \left(\phi\rho_f\right) + \nabla \cdot \left(\phi\rho_f \mathbf{u}_f\right) = -\Gamma_m \tag{6.2}$$

where ϕ is the porosity, which is defined as the fraction that is not solid, ρ_f and ρ_s the fluid and solid density respectively, $\mathbf{u}_f$ and $\mathbf{u}_s$ their velocities and Γ_m the amount of melt that is produced (Jackson & Cheadle 1998). The local seepage velocity $\phi\mathbf{u_f}$ is calculated using Darcy's law (Koehn et al. 2020):

$$\phi\left(\mathbf{u}_{\mathrm{f}} - \mathbf{u}_{\mathrm{s}}\right) = -\frac{K}{\mu_f}\nabla P \tag{6.3}$$

where K is the local permeability on a unit area, μ_f is the fluid viscosity. The model calculates the permeability using the Kozeny-Carman equation (Kozeny 1927, Carman 1937, 1956):

$$K(\phi) = \frac{r^2}{45}\frac{\phi^3}{(1-\phi)^2} \tag{6.4}$$

where r is a fixed grain size. This equation has been shown to be a good approximation for melt flow in migmatites (Brown et al. 1999). Equation 6.4 is used to calculate permeability in every cell of the fluid lattice except for the ones that are affected by a fracture. In this case, an extra term is added to account for the increase in permeability in cracks:

$$K_f = K + \phi_m K_{f_0} \tag{6.5}$$

where K is the permeability of the cell before accounting for the presence of a fracture, ϕ_m is the porosity generated by partial melting (corresponding to the increase in melt fraction), K_{f_0} a default value of permeability in a fracture (10^{-15} m^2). The increase in porosity (ϕ_m) is taken as a proxy for the fracture aperture, as the latter is not straightforward to obtain (Flekkøy et al. 2002). This approach in calculating permeability, which considers the variation in porosity to be caused by the opening of a fracture, reduces the resolution requirements and allows us to capture phenomena that happen at a smaller scale than the one of the fluid grid (Flekkøy et al. 2002).

The fluid is compressible, with its density calculated from the density at a reference pressure ρ_0, and varying as a function of the compressibility (β) and pressure (P):

$$\rho_\mathrm{f} = \rho_0(1 + \beta P)\,. \tag{6.6}$$

The solid compressibility is considered negligible compared with the fluid compressibility, so ρ_s is assumed constant. Substituting equation 6.6 for the fluid density and Darcy's law (equation 6.3) into the continuity equation for the fluid (equation 6.2), we obtain the diffusion equation for the fluid overpressure:

$$\phi\beta\left[\frac{\partial P}{\partial t} + \mathbf{u}_\mathrm{s}\nabla\cdot P\right] = \nabla\cdot\left[(1+\beta P)\frac{K}{\mu_f}\nabla P\right] - (1+\beta P)\nabla\cdot\mathbf{u}_\mathrm{s}. \tag{6.7}$$

Solid Phase

The elastic behaviour of the solid phase is modelled with a discrete-element model solved on a grid that is initially hexagonal. The elements on the grid are circular particles linked by a network of springs. The movement of the solid particles is a function of the momentum exchange between solid and fluid for unit mass of solid (dm) in a unit volume cell (dV), which is the sum of three forces:

$$d\mathrm{m}\frac{d\mathrm{V}_s}{dt} = f_e + f_p + f_g, \tag{6.8}$$

f_e being the interparticle elastic force, f_p the fluid pressure and f_g the gravitational loading.

We assume uniaxial strain, where only the vertical component of the strain tensor (ε_1) is not zero. Therefore, the vertical stress σ_1 is

$$\sigma_1 = \frac{(1-\nu)\,E}{(1+\nu)(1-2\nu)}\varepsilon_1 \tag{6.9}$$

where E is the Young's modulus and ν is the Poisson ratio. Assuming $\nu = 1/3$, we obtain $\sigma_1 = 2/3\,E\varepsilon_1$.

The elastic force for a particle is the sum of all forces applied by all connected springs. It can be decomposed into its normal (f_n) and its shear component (f_s):

$$f_e = f_\mathrm{n} + f_\mathrm{s} = \sum_{i=1}^{6} k_\mathrm{n}^i \Delta u_\mathrm{n}^i + \sum_{i=1}^{6} k_\mathrm{s}^i \Delta u_\mathrm{s}^i, \tag{6.10}$$

where k_n^i is the spring constant for the normal and k_s^i for the shear displacement. The sums are over six elements, which are the six neighbouring particles. If a spring breaks, it is removed from the model and a repulsive force is added in its place. This happens when the sum of strain energy for tensile (U_t) and shear (U_s) failure:

$$U_\mathrm{tot} = U_\mathrm{t} + U_\mathrm{s} \tag{6.11}$$

reaches a critical value, so that

$$\frac{U_\mathrm{s}}{E_\mathrm{cs}} + \frac{U_\mathrm{t}}{E_\mathrm{ct}} = \left(\frac{\sigma_\mathrm{n}}{\sigma_0}\right)^2 + \left(\frac{\tau}{\tau_0}\right)^2 = 1 \tag{6.12}$$

is satisfied. Here, E_ct is the critical strain energy for failure for tension, E_cs the one for shear, σ_n the normal stress, τ the shear stress, σ_0 the tensile strength, τ_0 the shear cohesion (Sachau & Koehn 2013).

Model Workflow

The sequence of processes followed by the code is shown in Figure 6.1. Once the physical properties and boundary conditions are set up, the numerical experiment starts a time loop in which the following steps are repeated. The first one is partial melting, where a fraction of the solid changes phase and becomes fluid. The mechanisms of this are shown in Figure 6.2: (1) A point is chosen as the location for partial melting (Figure 6.2b), (2) Its porosity increases and so does the porosity of the points around it, following a Gaussian shape (Figure 6.2a). As a consequence, fluid pressure increases following the processes described in Etheridge et al. (2021). The code then solves the equations for both phases and the information is passed between the two grids.

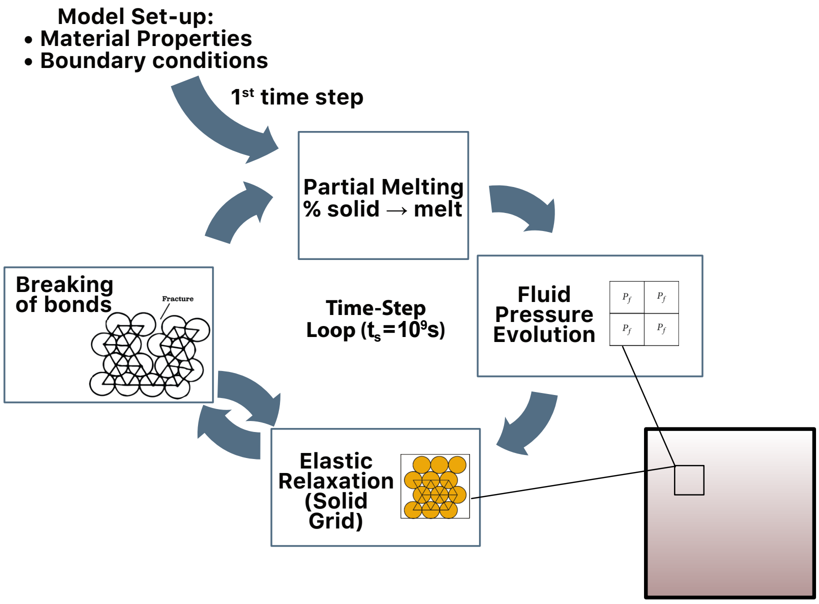

Figure 6.1: Sequence of processes in the numerical model. After the physical properties are set up, the time-step loop starts. Partial melting happens at each time step, increasing porosity and fluid pressure; then the model solves the equations for both media. If the stress applied to a spring is greater than the critical stress, the spring breaks. The model keeps applying the relaxation routine until a new equilibrium is reached.

When values are passed from one grid to the other, a linear weighting scheme is used. Weights are calculated based on the distance between the particle (r) and the square grid node (r_0) and are used to calculate a smoothing function:

$$s\left(r - r_o\right) = \begin{cases} \left(1 - \frac{x - x_0}{\Delta x}\right)\left(1 - \frac{y - y_0}{\Delta y}\right) & \text{if } x - x_0 < \Delta x,\ y - y_0 < \Delta y \\ 0 & \text{otherwise} \end{cases} \tag{6.13}$$

where x, y are the solid particle coordinates and x_0, y_0 describe the position of the square grid (fluid) node.

At the end of each time step, the elastic network is relaxed until a new equilibrium configuration is reached and all bonds are stable.

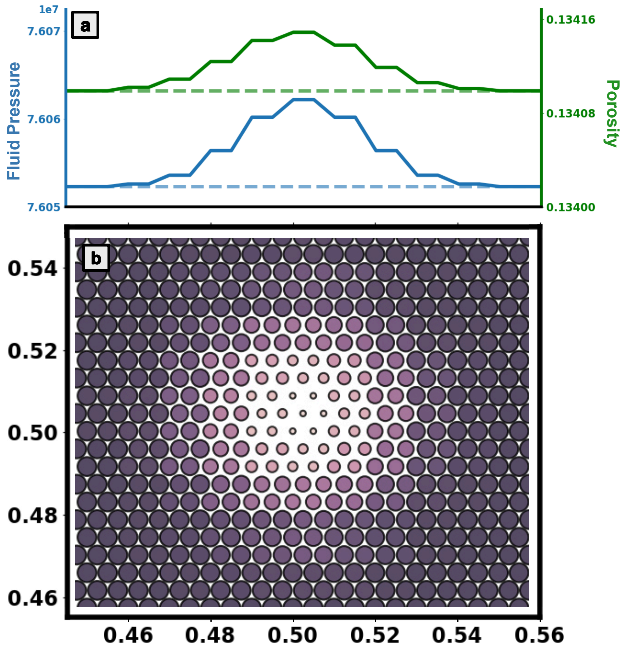

Figure 6.2: An example of how porosity and fluid pressure change when an area around a point is affected by partial melting. (a) Horizontal profiles of the two variables. (b) Representation of the solid fraction getting smaller: the particles representing the solid fraction reduce their size increasing the porosity and making more space for the fluid.

6.2.2 Model Set-up

The system considered in this study simulates a melt-producing zone, where each point in the domain has the same probability of producing melt. The host rock is already partially molten at the start of the numerical experiments; we simulate melt produced by the breakdown of hydrate minerals (Clemens & Mawer 1992, Connolly et al. 1997, Rushmer 2001, Etheridge et al. 2021) and explore the production of $\sim 27\%$ of melt.

The modelled area is set to represent 100 by 100 metres, divided into 100 fluid cells in each direction and into 200 by 230 solid particles. The higher number of solid particles in the vertical direction is due to the grid's triangular geometry. In all figures, axes are labelled non-dimensionally from 0 to 1, despite the physical domain size. The

Fixed Parameters

Parameter	Value	Units
Young's modulus[a]	10	GPa
Poisson's ratio[b]	1/3	-
Internal angle of friction[c]	30°	-
Tensile strength[d]	5	MPa
Rock density[e]	3000	kg/m^3
Melt density[f]	2500	kg/m^3
Initial Pore Fluid Pressure (λ_v) [g]	0.8333	-
Time step	10^9	s

Investigated Parameters

Parameter	Range	Units
Melt viscosity[h]	10^4 - 3.16×10^6	Pa s
Melt production rate[i]	0.1 - 0.9	% every melt spot (2 melt spots per time step)

[a] Jaeger & Cook (1976), Koehn et al. (2019)

[b] Jaeger & Cook (1976), Flekkøy et al. (2002), Koehn et al. (2019)

[c] Jaeger & Cook (1976), Koehn et al. (2019)

[d] Etheridge et al. (2021)

[e] as used in Jackson et al. (2003)

[f] as used in Jackson et al. (2003), gives a difference with the rock density of 500 kg/m^3 (Spiegelman 1993*b*)

[g] derived from the density difference (Etheridge et al. 2021)

[h] comparable to the ranges in Spiegelman (1993*a*), Brown et al. (1995), Clemens & Petford (1999), Hack & Thompson (2011)

[i] equivalent to 1% melt every 3.6 $\times 10^4$ years, Patiño Douce et al. (1990), Jackson et al. (2003).

Table 6.1: Parameters used in the numerical experiments and sources for their values.

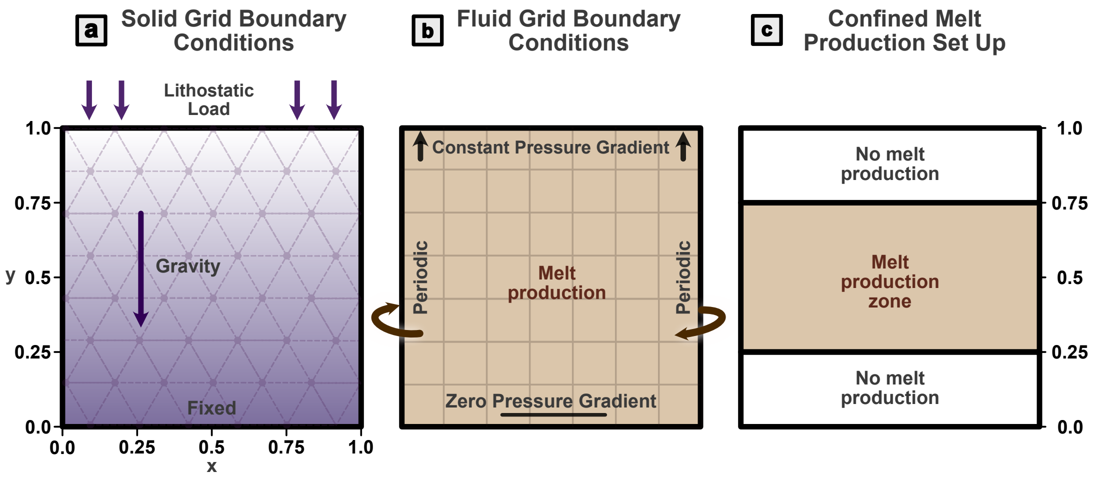

Figure 6.3: Set-up and boundary conditions of the numerical experiments. (a) Boundary conditions for the solid grid, including the gravitational force. (b) Boundary conditions for the fluid grid, showing that partial melting happens everywhere in the domain. (c) Set-up for simulations with one confined layer of melt production.

boundary conditions for the solid grid at the sides and bottom are free slip parallel to the boundary and repulsion perpendicular to it (Figure 6.3a). Fluid is free to escape at the top, where a constant pressure gradient is set between the last two rows (Figure 6.3b). A zero gradient is imposed on fluid pressure at the bottom and periodic boundary conditions are set between the two sides.

Gravity is applied vertically, producing confinement stress on the solid particles in the simulation domain (Figure 6.3a). The corresponding extra pressure is applied to the upper boundary of the domain, simulating the weight of the column of rock above. Stress is calculated by letting the particles in the solid grid relax until they reach their equilibrium position. Fluid pressure is also defined by a gradient according to gravity and its values are close to magmastatic (Etheridge et al. 2021).

Values for depth and rock strength are not defined according to absolute lower-crust values, but, once scaled, are consistent with a system that has a confining pressure equivalent to 1.2GPa, near-magmastatic fluid pressure and tensile strength of 5MPa (typical conditions described by Etheridge et al. 2021). In such a system, Etheridge et al. (2021) modelled that a melt pressure that exceeds the confining pressure by just 0.4% would be enough to fracture the host rock. This melt overpressure would be in the order of magnitude of 10^6 Pa, consistent with what is observed in our numerical experiments.

The parameters used in our numerical experiments are reported in table 6.1. The first set of parameters includes values that were kept constant in all simulations. The second part of the table reports the ranges for the parameters that were investigated. The first physical property that was changed is the fluid viscosity. This was varied between 10^4 and 3.16×10^6 Pa s (Spiegelman 1993*a*, Brown et al. 1995, Clemens & Petford 1999, Jackson et al. 2003). The second parameter that was investigated is the melt production rate. Melt production follows the processes described in Figure 6.2; at every time step, the model randomly selects 2 points in the domain for melt production and each point produces melt for 50 time steps after it was chosen. Each of these points consumes a fraction of the solid medium, which becomes porosity. This value is fixed for each simulation and is between 0.001 (0.1%) and 0.009 (0.9%). As the time step is set to 10^9 seconds, this results in the formation of 1% of new melt every $\sim 3.6 \times10^4$ to 2.85×10^5 years, comparable to rates reported in Patiño Douce et al. (1990), Jackson et al. (2003). Patiño Douce et al. (1990) calculated the production of 15% melt in 0.5 Ma (or 1% melt in 3.3×10^4 years), Jackson et al. (2003) used rates in the range of $\sim$ 1% every 1.33×10^3 to 9.3×10^4 years.

To avoid sharp gradients with the neighbouring points, a 2-D Gaussian function is defined around the chosen point. If the central point is close to a boundary, the Gaussian shape continues from the opposite side, so that each point in the domain has the same probability to increase its melt content by the same amount.

A second set of simulations consists of a confined area of melt production that is limited in the y direction. The geometry of their set-up is shown in Figure 6.3c: partial melting only happens in the area between y = 0.25 and y = 0.75. As melting occurs in half of the domain, only one point per time step is chosen as opposed to two. The other physical properties are the same as in the first case and do not vary between the central and the confining layers. This means that the domain of each numerical experiment starts as homogeneous, and as the central area starts producing melt, the layer becomes more porous and permeable.

6.2.3 Methods of Fracture Pattern Analysis

Topology and Fracture Abundance

As our goal is to develop an understanding of the differences in fracture network patterns, we aim to characterise and quantify their geometry. These can be effectively described using topological features. In two dimensions, they can be modelled as a system of branches and nodes and topological features can be used to describe them in terms of dimensionless parameters (Sanderson & Nixon 2015). Topological analyses capture important features such as fracture interactions with each other and therefore are an effective tool to study a network's connectivity. The two fundamental elements of a fracture network are shown in Figure 6.4. A node is defined as the intersection between two fractures and a branch is the segment of a fracture between two nodes. A node can be of three types based on its connectivity: I node if it is an isolated tip, Y node if a fracture ends as an abutment against another fracture, or X node if it is formed by an intersection of two fractures (Manzocchi 2002, Sanderson & Nixon 2015). To visualise their relative occurrence, each fracture network can be plotted as a single point in the I-Y-X space of a ternary diagram. Other measures of fracture abundance include the number of branches in the system and their intensity (Dershowitz & Herda 1992), which is defined as:

$$B_{22} = N_B B_C^2 / A \tag{6.14}$$

where N_B is the total number of branches, B_C^2 the average branch length and A the area. The two numbers in 'B_{22}' follow the nomenclature in Sanderson & Nixon (2015) and refer to the dimensions of the sampling region (area) and of the sampled feature (length squared).

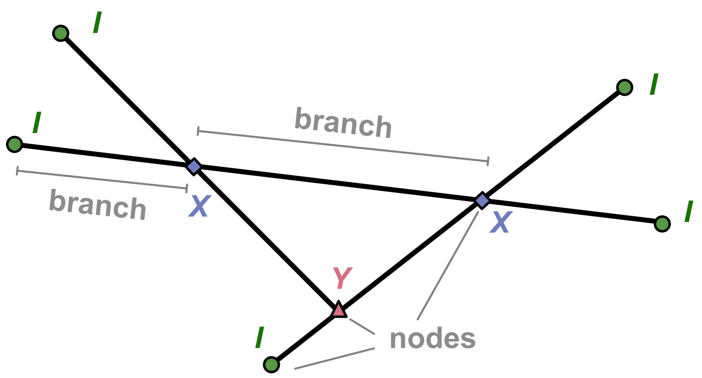

Figure 6.4: Schematic representation of the elements in a fracture network. A node is the intersection between two fractures and a branch is the segment between two nodes. The different symbols represent different types of nodes: I, Y and X.

Fracture Cluster Analysis using DBSCAN

To further characterise properties such as the permeability of a network, we perform a cluster analysis using the DBSCAN (Density-Based Spatial Clustering of Applications with Noise) algorithm. This technique is particularly useful for distinguishing patterns of localised fractures from isolated cracks and performing analyses that are independent of the grid geometry. Therefore, the goal of our analysis is to identify and quantify clusters of fractures, in particular when they form high-permeability channels. Figure 6.5 shows how it can be applied to the fracture data. In this example, the input data for the algorithm was the fracture distribution shown in Figure 6.5a, where each point was classified as 'fractured' (number of broken bonds ≥ 1) or 'not fractured' (no broken bonds, corresponding to the areas in black). In DBSCAN, clusters are defined as groups of closely packed points, represented by different colours in Figure 6.5b. The ellipses, overlaid on the clusters, represent the spatial extent and orientation of each cluster. They provide a simplified geometrical representation and were obtained from the eigenvectors and eigenvalues of the covariant matrix. The lengths of the major and minor axes of each ellipse correspond to the square roots of the largest and smallest

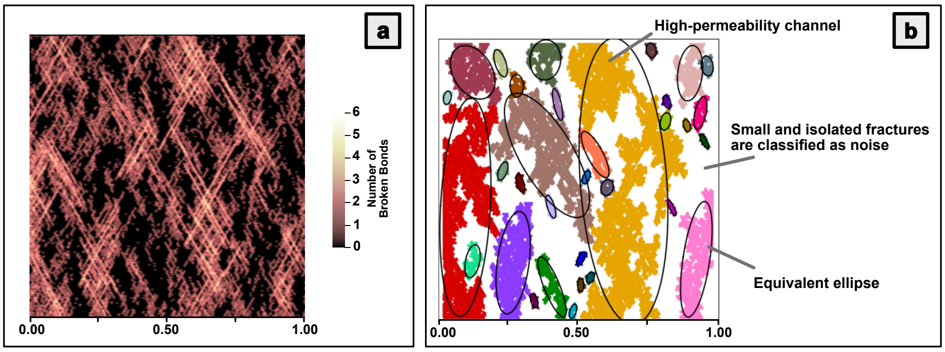

Figure 6.5: An example of the application of the DBSCAN algorithm to identify areas of high fracture density. (a): example of a fracture pattern from a numerical experiment. The colour represents the number of broken bonds around each particle of the numerical domain. (b): Fracture data classified into clusters according to the DBSCAN algorithm. The ellipses drawn over each cluster are obtained from the cluster shape and are a useful approximation to obtain parameters such as elongation and orientation.

eigenvalues, respectively. The orientation of each ellipse is determined by the angle of the eigenvector associated with the largest eigenvalue.

The DBSCAN algorithm has often been used in fracture analysis to categorise discontinuity planes into different classes, usually applied to a 3-dimensional cloud of points representing an outcrop (Riquelme et al. 2014). Our application is slightly different, as it is based on the location of the points and their physical proximity to their neighbours. It also focuses on classifying smaller fractures into individual fracture areas rather than fracture classes (e.g. sets of joints).

6.3 Results

6.3.1 Fracture Pattern Evolution with Time

As described in previous sections, the phase transition associated with partial melting results in an increase in fluid (melt) pressure. Once enough pressure has accumulated, fractures start forming in the host rock. Figure 6.6 shows two examples of fracture networks generated by melt overpressure and how they develop with time. The only

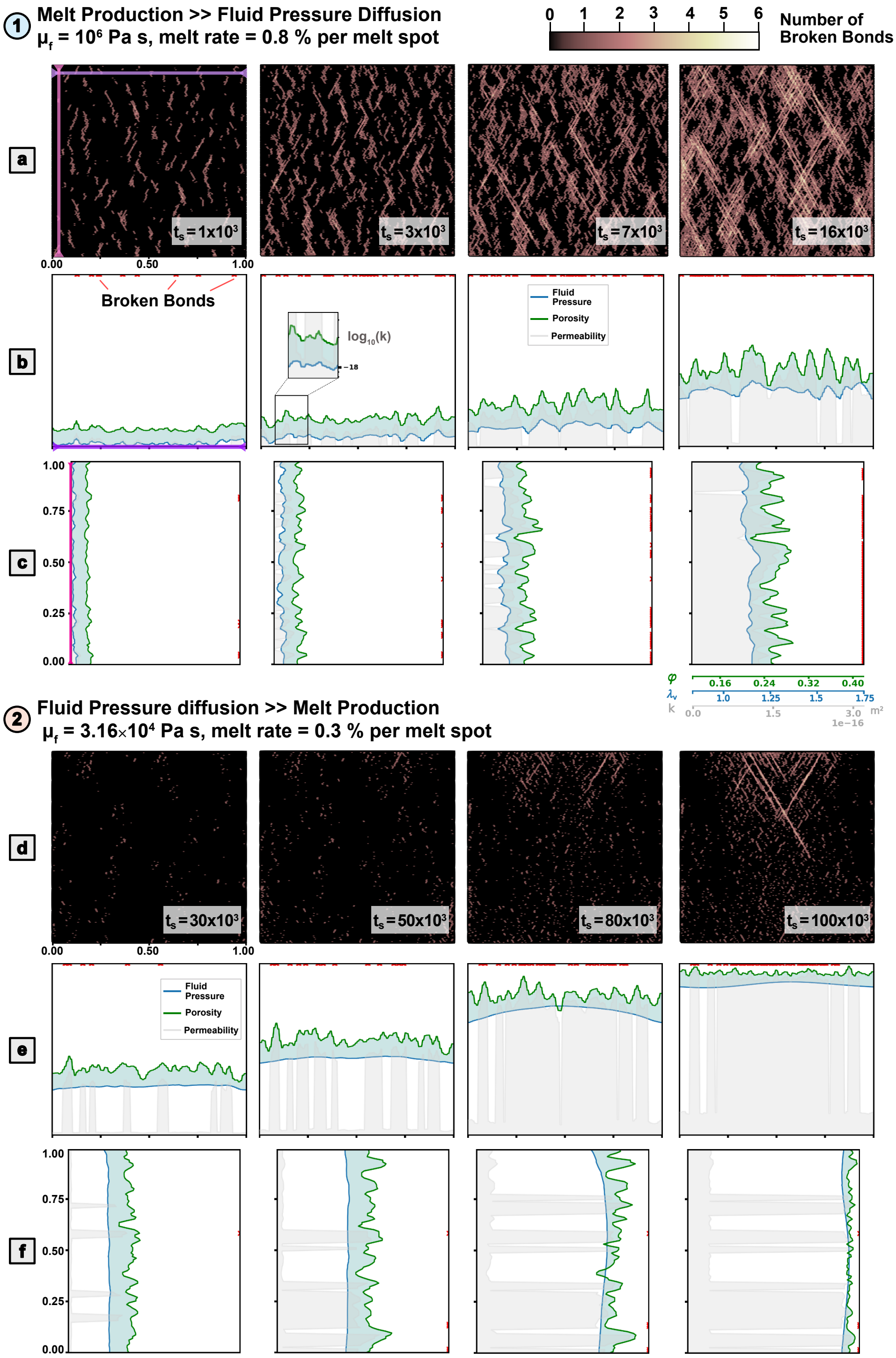

Figure 6.6: Evolution of fracture patterns with time for two ‘example’ cases: (1) $\mu_f = 10^6$Pa s, melt production = 0.008 (0.8%) per point per time step; (2) $\mu_f = 3.16 \times 10^4$Pa s, melt rate = 0.003 (0.3%) per point per time step. Fractures are visualised as the number of broken bonds around each solid particle, with a lighter colour showing a higher number and therefore more intense fracturing. The line plots (*a*, *c*, *e* and *f*) show melt pressure, porosity and permeability values from two lines, one horizontal (*b* and *e*) and one vertical (*c* and *f*). Their location is indicated by the lines in the first panel. Red crosses represent a fracture along the profile.

differences between the two cases are the values of melt viscosity and melt production rate. The first example (*case 1*, Figures 6.6a, 6.6b, and 6.6c) shows a system with a high-viscosity melt affected by a high melt production rate. In this case, the dominant process is the rate of melt production, while fluid pressure diffusion is, in comparison, slower. Fractures start forming at relatively early time steps (e.g. $t_s = 1000$), due to the fast accumulation of fluid pressure. At these initial times, short cracks are scattered homogeneously across the whole domain. Even though the melt spots are circular, fractures are elongated, roughly oriented vertically and show very few intersections between them. Their position corresponds to areas of particularly high melt pressure, whose distribution follows the location of the randomly chosen melting points. This correlation can also be seen in the pressure and porosity profiles (Figure 6.6b and 6.6c): In the first few time steps, there is very little fluid pressure diffusion and the two variables have very similar distributions. Permeability generally follows the porosity profile (see the zoomed-in logarithmic plot in Figure 6.6b, $t_s = 3000$), except for the areas where fractures open, where there is a significant increase. As time advances, the continuous production of excess fluid pressure has two main effects: it can make the fractured areas propagate at their tip and/or widen them, forming large clusters of cracks. The development of such structures greatly impacts permeability (Figure 6.6b and 6.6c, $t_s = 7000$), which shows the same profile as porosity where the rock is intact but greatly increases as a consequence of the numerous fractures. This makes the interaction between porosity and fluid pressure more complex: While porosity keeps a similar profile, fluid pressure starts showing the effect of diffusion and slowly becomes smoother. In the final time steps, the clusters grow to form large damage zones characterised by numerous fractures that cross-cut each other. Some fractures propagate outside the clusters, increasing the overall fluid connectivity. Fluid pressure diffuses at a much higher rate, aided by generally high permeability values, which causes its profile to be much smoother than the line representing porosity. Fracture connectivity can be seen from the ternary diagram of node proportion in Figure 6.7, where the blue points show the evolution of the relative number of I, Y and X. In the first time steps, most of the nodes are isolated (I), with only a few Y nodes. As the simulation progresses, Y nodes increase significantly and they become the dominant type at time step = 7000. At the same time, the number of X nodes also increases, though not as fast. The last time step in the figure shows a well-developed network with many X nodes.

The second example, *case 2* in Figures 6.6d, 6.6e and 6.6f, involves a low-viscosity melt (3.16×10^4 Pa s, or $10^{4.5}$ Pa s) and a low melt production rate (0.003 per spot per time step). This represents a case where fluid pressure diffusion is fast compared to the production of melt, i.e. the melt viscosity is low and can diffuse efficiently. The effect of fast pressure diffusion is clear in the fluid pressure plots, where the pressure profiles are already quite smooth in the first time steps of Figure 6.6e and pressure gradients are very small. As opposed to the first case, where fluid pressure diffusion was mainly a consequence of fracture formation, here the profiles are already flat even when there are still very few fractures. Porosity is also slightly more homogeneous because partial melting occurs in smaller amounts over a higher number of locations. Fractures only start to form after a much longer period of time, and once a higher melt content has been produced. In contrast with the first case, where a single high-pressure spot could generate an elongated fractured zone, cracks in Figure 6.6d remain small for a long time after they appear. Eventually, small fractures begin to merge ($t_s = 80 \times 10^3$), forming sets of long fissures that are locally parallel. Fractures are mostly localised in a central, vertical channel in an area near the top. This extremely low connectivity is particularly evident in the ternary plot for this case (in red in Figure 6.7) in the points corresponding to the first three time steps. Almost all the nodes are of type I, showing that cross-cutting fractures are rare. Only the last of the four reported time steps shows a modest increase in Y nodes and an even smaller one in X nodes.

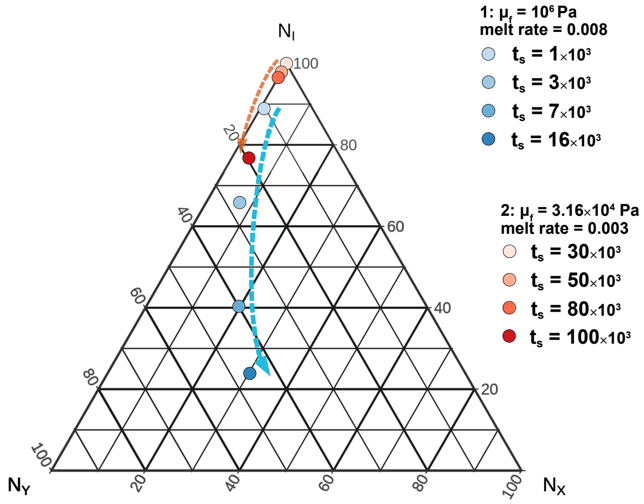

Figure 6.7: Ternary plot showing the evolution of fracture network connectivity with time through the relative abundance of I, Y and X nodes. Each point corresponds to a time step shown in Figure 6.6. Case [1], in blue, $\mu_f = 10^6$Pa s, melt production = 0.008 (0.8%) per point per time step; Case [2], in red, $\mu_f = 10^{4.5}$Pa s, melt rate = 0.003 (0.3%) per point per time step.

6.3.2 The Role of Viscosity and Melt Production Rate on Fracture Pattern Formation

Figure 6.8 shows the fracture patterns of selected combinations of melt production rate and melt viscosity values; all the other parameters are kept constant. All the panels in this figure are made after the same amount of melt was generated rather than after the same number of time steps have passed. Because higher melt production rates reach higher melt fractions faster, their fracture pattern shown in this figure corresponds to a shorter time since the start of the simulation. For example, as the reference time step chosen for Figure 6.8 is $t_{ref} = 100 \times 10^3$, the time step for a melt production rate of 0.004 is 25×10^3, half the time of the one with a melt rate of 0.002 ($t_s = 50 \times10^3$).

Every row in Figure 6.8 represents one value of melt production rate and a different value of melt viscosity. Melt viscosity strongly influences both the amount of fractures and the way they intersect each other. Low viscosity values produce isolated cracks that are distributed uniformly in the domain. Even when the melt production rate is high, fractures cannot propagate far from where they form. The resulting patterns consist of a random distribution of very short cracks that do not form clusters. The number of broken bonds around each solid particle can be used as an indicator of fracture aperture: Systems with a low melt viscosity are dominated by darker colours, showing that most of the fractures are narrow. On the other hand, high viscosity values are always associated with a higher number of fractures, which are also generally longer and wider. When the rate of melt production is also high, they can form clusters characterised by high fracture connectivity within themselves and with other clusters. These clusters can be defined as damage zones and are the places where the widest fractures are present. The higher the viscosity value, the stronger the localisation is, generating fracture clusters that have complex shapes.

Each column in Figure 6.8 includes numerical experiments that have the same rate of melt production. A slow rate results in very few, short fractures. Similar to the patterns described for low viscosity values, these short cracks are randomly scattered throughout the melting area. As the melt production rate increases (top rows of Figure 6.8), the number of fractures in the system increases. However, the fractures do not localise into clusters unless the melt viscosity is also high. The formation of damage zones with wide fractures (high number of broken bonds) and high fracture localisation can only occur if melt viscosity is sufficiently high. A higher degree of fracturing caused by a higher melt production rate is the consequence of the formation of new cracks rather than the growth of already existing ones.

6.3.3 Analysis of Fracture Patterns

Topological features and fracture abundance parameters are effective ways to describe a network of fractures (Figures 6.9 and 6.10). The plots in Figure 6.9 show how fracture parameters vary with melt viscosity and melt production rates: the first group of plots shows the number of branches (N_B), while the second one the dimensionless intensity. Each square or point in these plots represents a numerical experiment and therefore

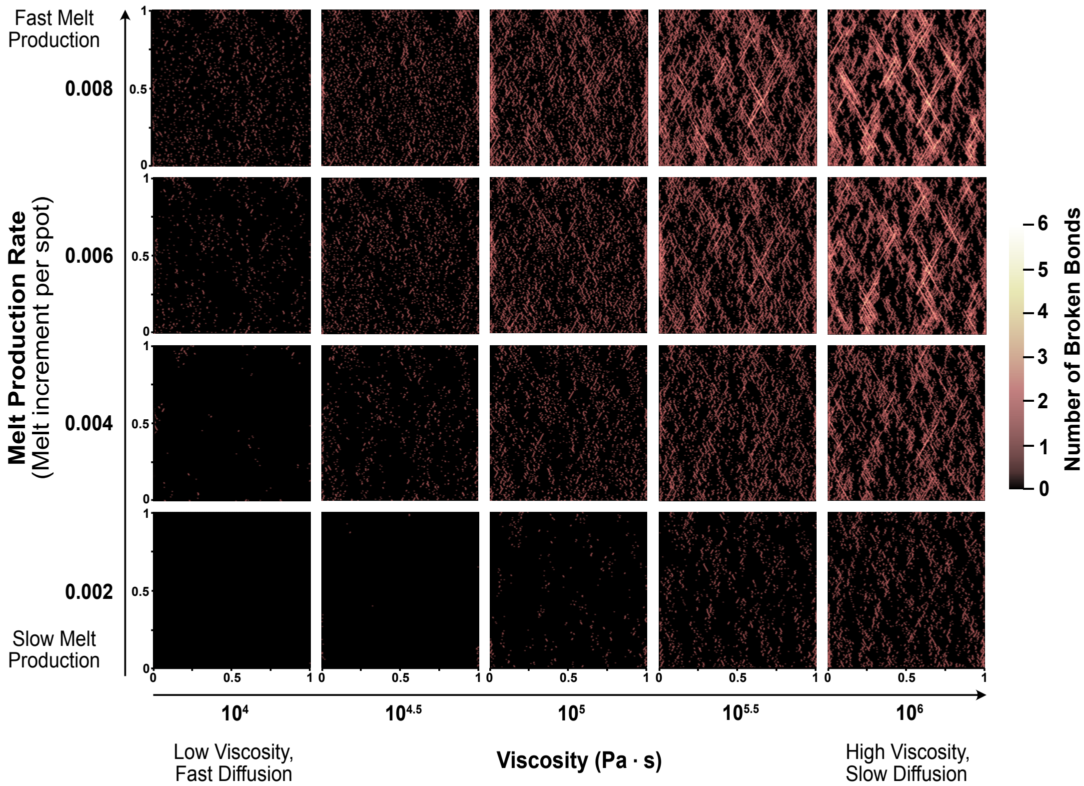

Figure 6.8: Fracture patterns resulting from varying melt viscosity (x-axis) and melt production rate (y-axis). Fractures are visualised using the number of broken bonds around each solid particle. All figures are taken after the same amount of melt has been produced. Reference time step $t_{ref} = 100 \times 10^3$.

a combination of melt production rate and viscosity. Heat maps (Figures 6.9a and 6.9d) can help visualise the simultaneous contributions of the two variables, while the other plots allow us to investigate them one at a time. Numerical experiments with $\mu_f = 10^{6.5}$ and a melt rate greater than 0.004 are missing because they did not reach the reference time due to the intense fracturing and complex particle movement. As described in section 6.3.2, the number of fractures is larger when the melt viscosity is higher (values on the right-hand side in Figure 6.9b). When the melt production rate is also high (pink, blue and green lines), the largest difference is observed at lower viscosity values (e.g. between $\mu_f = 10^4$ and $\mu_f = 10^5$). This shows that melt viscosity has a larger role in this range and a further increase does not affect the patterns. If the rate of melt production is high (i.e. the lines that are highest in the plot), N_B does not depend on the melt viscosity when the values of viscosity are high.

No fractures were observed at low melt viscosity values and low melt production rates (bottom left corner of Figure 6.9a). The lower the melt rate (e.g. the left-hand side of Figure 6.9c), the higher the viscosity value needs to be in order to observe fractures. In general, every line in Figure 6.9c shows an increase when the melt production rate is higher, indicating that this parameter has an important role in the fracture patterns. However, variations in the melt rate have the strongest effect on the number of fractures when the melt viscosity is high (blue and green line) and the melt rate is low. Lines representing systems with a high melt viscosity plateau after a certain melt production rate.

Dimensionless intensity (Figures 6.9d, 6.9e and 6.9f and defined in equation 6.14) is another useful parameter to describe fracture abundance in an area (e.g. Sanderson & Nixon 2015). In our numerical experiments, it increases with the melt viscosity (Figure 6.9e) with a similar trend to the number of branches (Figure 6.9b). High melt production rates create the largest differences in dimensionless intensity when different values of melt viscosity are applied (pink and blue lines in the central part of the plot). In comparison, the dimensionless intensity varies very little with melt viscosity when the production of melt is slow (bottom lines in Figure 6.9e). When considering the effect of the melt rate, trends in the dimensionless intensity (Figure 6.9f) are again similar to the ones in the number of branches (Figure 6.9c). However, this parameter still shows an increase at high melt rates (0.008 and 0.009, on the right-hand side of Figure 6.9f), capturing the fact that even if the number of branches is the same for different melt rates, their average length is higher.

Ternary diagrams for the classification of node types are widely used to characterise fracture networks, as they are useful to describe the connectivity of the systems. Figures 6.10a and 6.10b show the relative abundance of I, Y and X nodes and points are coloured by melt production rate (Figure 6.10a) and melt viscosity (Figure 6.10b). They show the network data split into ranges of the two variables. In general, the systems

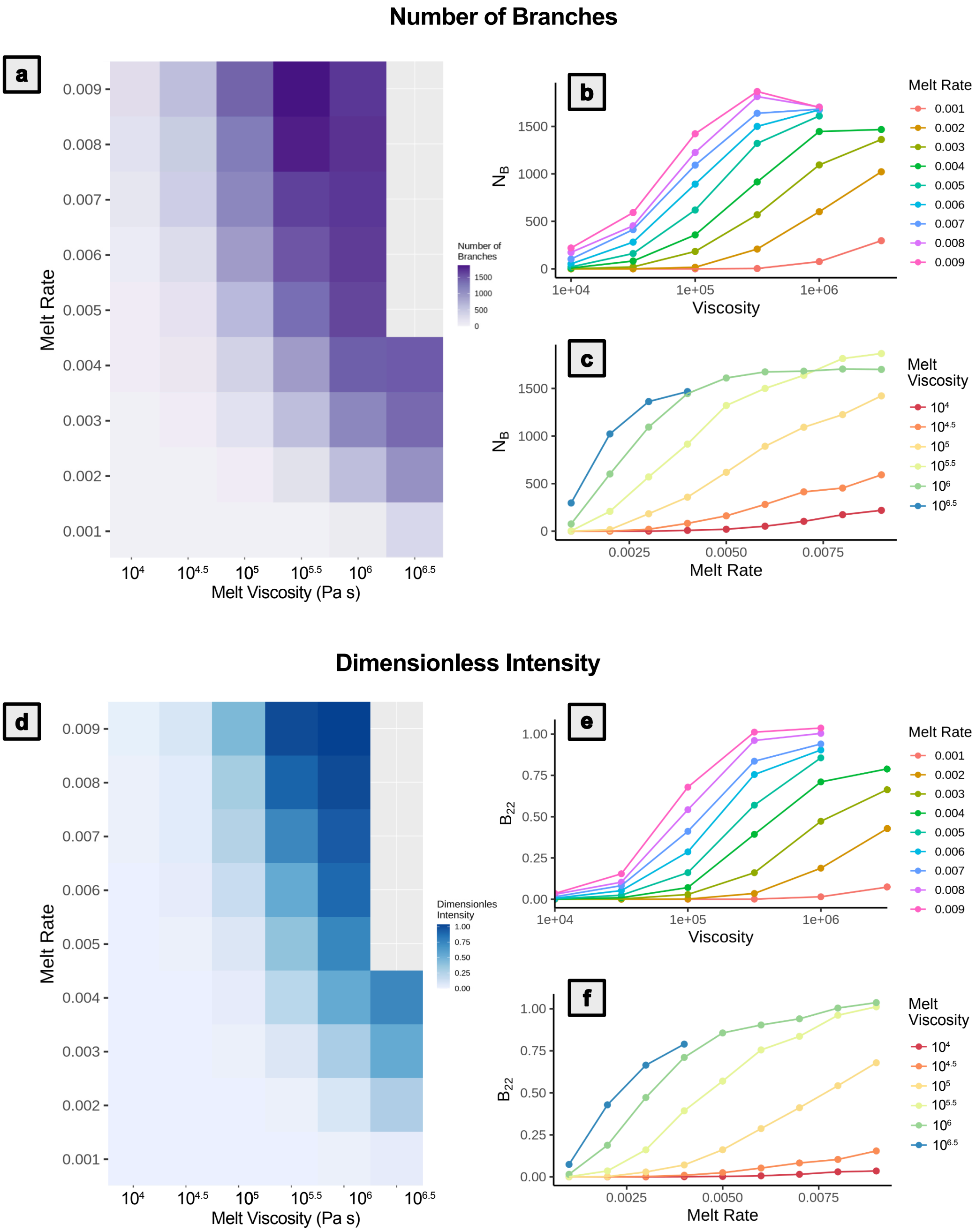

Figure 6.9: Diagrams showing how the extent of fracturing changes when melt viscosity and melt production rate are varied. (a), (b) and (c): Number of branches in each simulation as a function of each parameter. Each square in the heat map (a) represents a different numerical experiment, i.e. a combination of melt production rate and viscosity. Line plots show detailed trends of the fracture parameters with viscosity (b) and melt rate (c), where each colour represents a value of melt rate and viscosity respectively. (d), (e) and (f): same types of plots showing the dimensionless intensity (B_{22}). The heatmap (d) combines both variables, while the line plots (e and f) show them separately. The reference time $t_{ref} = 100 \times 10^3$ is the same as in Figure 6.8.

with the highest relative abundance of X and Y nodes are the ones with the highest viscosity values and melt production rates. In Figure 6.10a, four viscosity ranges have been defined. If the viscosity is low, the few fractures are isolated and their nodes are mostly of type I. At higher values of viscosity, the systems can potentially develop better-connected networks. The rate of melt production starts playing a more significant role: a higher melt rate results in a higher number of Y nodes (intermediate melt viscosity) and eventually in an increase in X nodes too (high and very high viscosity). At very high viscosity values, the same proportion of node types is achieved at lower melt production rates. Figure 6.10b shows four categories of melt production rate. When this is low, the only way to form Y nodes is to have a very high viscosity. We only start to observe X nodes at intermediate rates (panel 2), where high viscosity values create more connections between fractures. In this range, the role of melt viscosity is clear: high values create an abundance of Y nodes and some X nodes. A further increase in melt production rate does not have a major effect on the node types (panels 3 and 4). This is consistent with the plateau observed in the parameters in Figures 6.9a and 6.9b.

The DBSCAN algorithm was used to classify fractures into clusters based on their spatial distribution. These clusters are areas of high fracture density that we can define as damage zones. Figure 6.11 includes plots of a few parameters obtained by analysing the DBSCAN results and shows that the cluster occurrence, shape and spatial distribution are influenced by the melt viscosity and production rate. Figure 6.11a shows how the number of clusters changes when the melt viscosity and production rate are changed. No clusters are found when the viscosity is very low, even at high melt production rates. As viscosity increases, more and more clusters form (top panel of Figure 6.11a). This is true for any value of melt production rate for which data is available. The number of clusters also increases with the melt production rate, except for the highest values of viscosity. This decrease in the number of clusters is associated with a sharp increase in the cluster size (Figure 6.11b). Size is the parameter with the clearest correlation between the two variables. Clusters are larger when viscosity

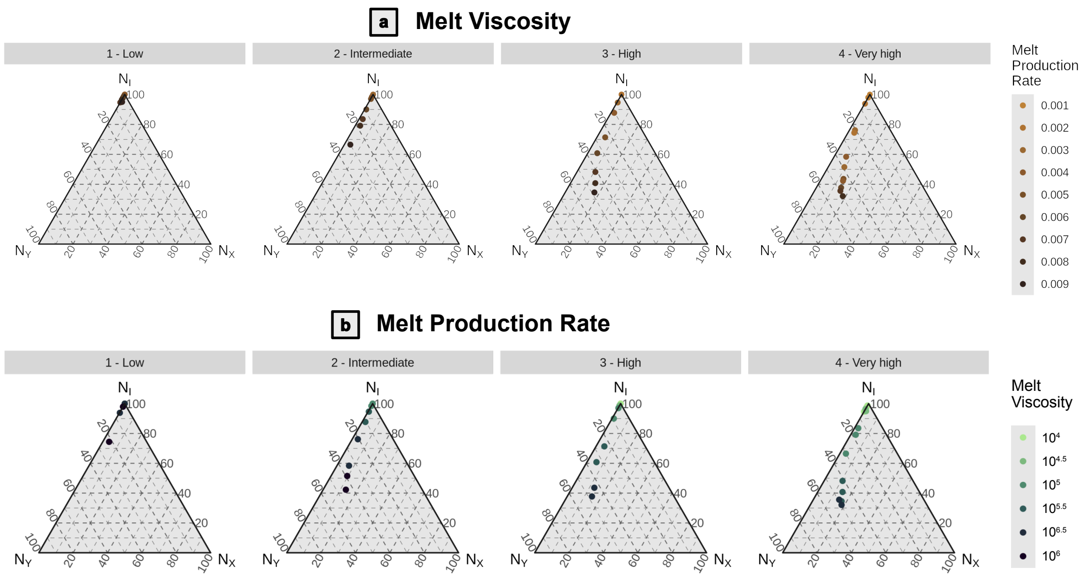

Figure 6.10: The role of melt viscosity and melt production rate on fracture connectivity quantified using the relative abundance of I, Y and X nodes. Each point represents a numerical experiment and is classified based on its melt production rate and melt viscosity value. (a): Melt viscosity values are split into four categories, and data points are coloured by their melt production rates. Low: $\mu_f = 10^4$ and $\mu_f = 10^{4.5}$, Intermediate: $\mu_f = 10^5$, High: $\mu_f = 10^{5.5}$, Very high: $\mu_f = 10^6$ and $\mu_f = 10^{6.5}$. (b): Data showing melt production rate categories and colour is the viscosity. Low: 0.1 and 0.2% per melting spot, intermediate: 0.3 and 0.4%, high: 0.5 and 0.6%, very high: 0.7, 0.8 and 0.9%. Data points correspond to the reference time step $t_{ref} = 100$ shown in Figure 6.8.

and melt production rates are higher and the melt rate has a larger impact on cluster size when the viscosity is high. The last two parameters shown in Figure 6.11 are how far the average cluster orientation is from the vertical direction (Figure 6.11c) and how elongated the clusters are (Figure 6.11d). Trends in these two parameters are not as clear as the ones observed in the first two plots (Figures 6.11a and 6.11b). In systems with a high viscosity and a high melt rate, there is a slight tendency to form clusters that are closer to vertical. Clusters also tend to be more elongated when the melt production rate and the melt viscosity are higher (right-hand side of the plots in Figure 6.11d). The average cluster elongation generally increases with melt viscosity but does not seem to depend on the melt production rate.

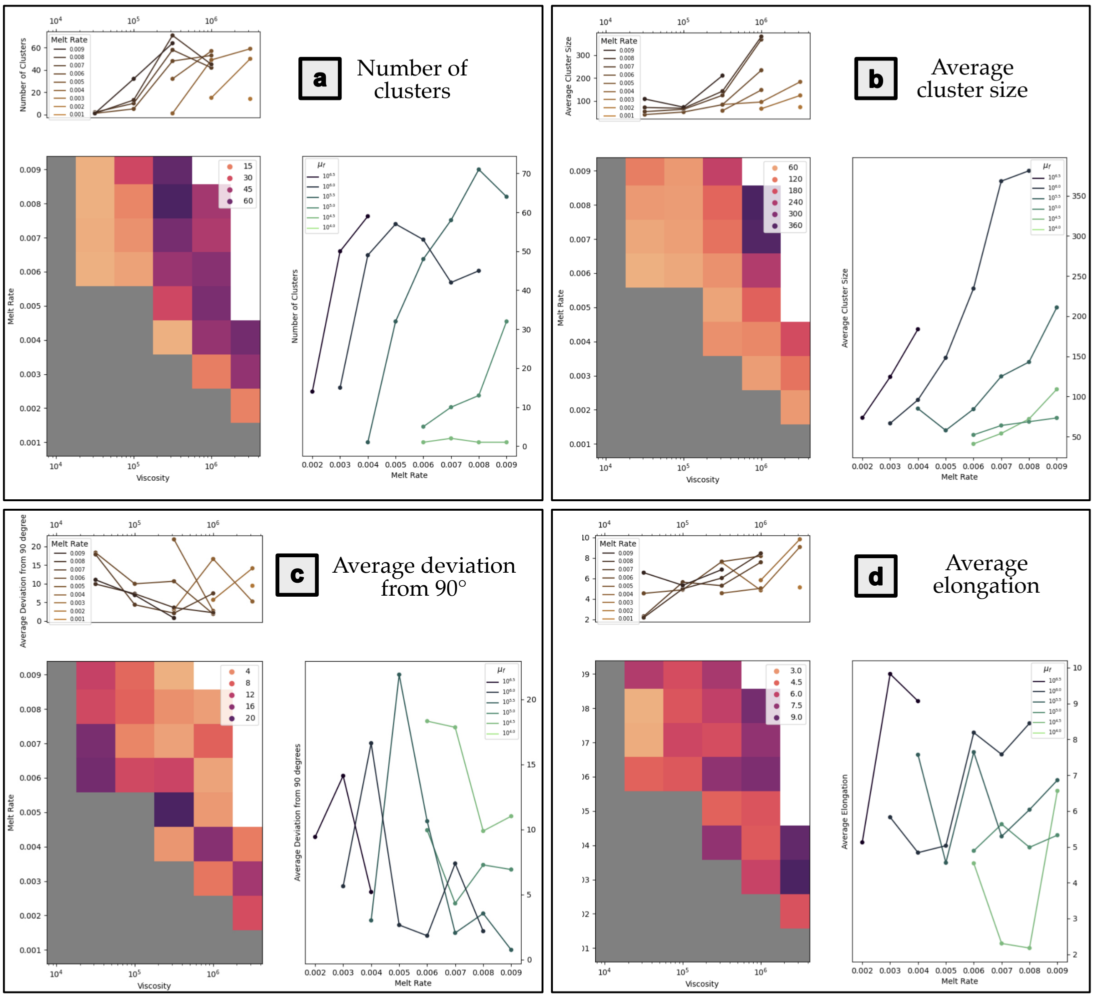

Figure 6.11: Parameters obtained applying the DBSCAN algorithm to the fracture distribution: (a) Number of fracture clusters, (b) Average cluster size, (c) Average deviation from vertical, weighted by the cluster size, (d) Average elongation of the clusters, weighted by their size.

6.3.4 Confined Production Zone

Figure 6.12 shows the results of two simulations with the same initial physical properties as the two cases in Figure 6.6 but partial melting is confined in a single layer in the central 50% of the numerical domain. Like in the two cases in Figure 6.6, the first example represents a system with a fast melt production while the second one shows a fast diffusion rate. Overall, the fracture network in Figure 6.12a is not too different from the patterns in case 1 in Figure 6.6. However, connectivity is slightly

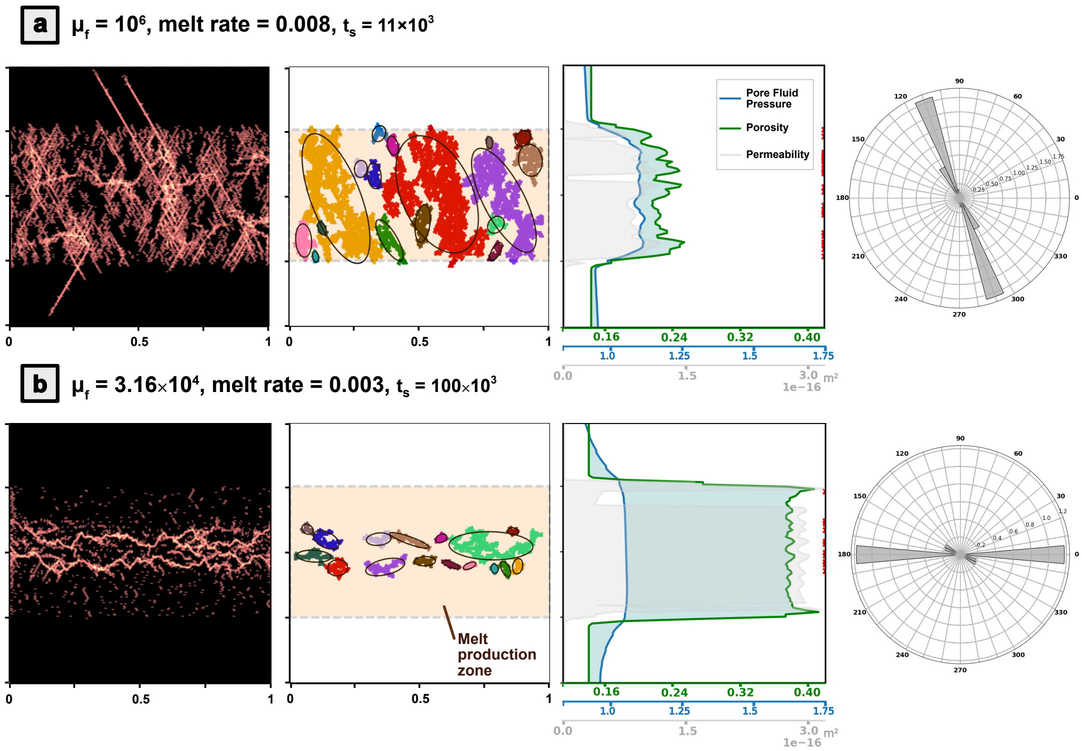

Figure 6.12: Two cases where partial melting is confined inside a layer. Fracture patterns, clusters identified by the DBSCAN algorithm, vertical profiles of three physical properties (fluid pressure, porosity, permeability) and rose diagrams showing the cluster orientation.

higher in this case and the fractures are more localised. The main difference is that in the non-confined case, damage zones were weakly connected by fractures with a ± 60°orientation; here, the larger damage zones are also connected horizontally by a more continuous network. The increase in fluid pressure and porosity in the melt-producing zone is clearly visible in the vertical profiles. This plot also confirms that pressure diffusion into the surrounding area is limited. When pressure diffusion is the fastest process (Figure 6.12b), the differences are much more evident. While there were very few fractures at t_s = 100×10³ in Figure 6.6d, here there is a well-developed, anastomosing set of fractures that runs for the entire width of the melting area. Despite the fractures being strongly localised into a few lines, some clusters were identified. Their orientation and shape show significant differences: clusters are mainly horizontal (parallel to the margins of the melting area) and have a higher elongation. In this case, fluid pressure has a smooth profile, indicating efficient diffusion into the adjacent layers.

6.4 Discussion

6.4.1 The Effect of the Relative Rates of Melt Pressure Diffusion and Melt Production Rate

Our numerical experiments show that fracture networks created by melt overpressure are very sensitive to variations in melt viscosity and rate of melt production. In particular, extensive fracture networks can develop if the rate of fluid pressure increase is sufficiently high to counter fluid pressure diffusion. In this system, melt viscosity controls the rate of pressure diffusion: when melt viscosity is low, the rates of pressure diffusion are high, while a high viscosity value makes diffusion slower (Petford 1995). The rate of melt production is one of the main factors that increase melt pressure; on the other hand, it also increases the porosity, which favours pressure diffusion (Etheridge et al. 2021). Therefore, during partial melting without external deformation, the rate of change of melt pressure is the result of the relative contribution of these processes. The opening and propagation of fractures depend on which process is faster, fluid pressure diffusion or the generation of melt.

A well-developed and connected network was only obtained when melt was generated at a high rate and fluid pressure was diffusing slowly (high melt viscosity). This situation favours a strong fluid pressure localisation that leads to melt-enhanced embrittlement (Davidson et al. 1994, Rushmer 2001).

When diffusion is highly efficient (case 2 in Figure 6.6), the system does not develop any major fractures and melt migration happens in the form of porous flow. This melt migration mechanism occurs along grain boundaries and, as suggested by Stuart et al. (2016) and Maierová et al. (2023), may not require to be driven by tectonic deformation.

If melt is generated at a high rate and diffusion is also fast, the pattern in the host rock fractures consists of very short cracks. In this case, a sudden increase in fluid pressure breaks the host rock, which causes the permeability to increase. The low melt viscosity combined with the fractures then allows the fluid pressure to be dissipated quickly and the fractures cannot propagate. The result is a pattern with fractures that are few, short, isolated and that cannot form clusters. In this scenario, the dominant process that allows melt to migrate from its source rock is diffuse porous flow (Scott & Stevenson 1986, Turcotte & Ahern 1978). A system with few fractures with a uniform distribution and no preferential orientation is compatible with the interpretation by Sawyer (2001) of an efficient melt diffusion.

On the other hand, a high viscosity value allows pressure to build up. Even if the production of melt is slow, which gives time for the fluid pressure to diffuse, fractures can propagate slightly more than a system with a high melt rate and low viscosity.

In both of these intermediate cases, fractures are short and their connectivity is low, but their presence is enough to favour pressure diffusion. Melt migration happens as a combination of porous flow aided by small cracks in the host rock, though without the development of a fracture network.

6.4.2 Quantification of Fracture Patterns

Fracture abundance in each simulation was measured using two parameters: the number of branches (Figures 6.9a, 6.9b and 6.9c) and the dimensionless intensity (equation 6.14, Figures 6.9d, 6.9e and 6.9f). Both clearly indicate that higher values in melt production and melt viscosity lead to the development of networks with a higher number of fractures and more intense fracturing. Although the two parameters show a very similar trend, they include a subtle difference. The dimensionless intensity in a 2-D system scales linearly with the number of branches and with the square of the average branch length. As described in section 6.3.3, points representing systems with a high melt rate show a plateau at high values of melt viscosity and vice versa

(Figures 6.9b and 6.9c). However, this behaviour is not present in plots reporting the dimensionless intensity (Figures 6.9e and 6.9f). This suggests that if two systems have the same (high) melt production rate and also have a high melt viscosity, they will have a similar number of branches but the average branch length will be higher in the one with a higher melt viscosity.

These parameters are effective at quantifying the extent of fracturing, but they are not sufficient to describe the effective permeability. Two fracture networks can have the same number of branches and fracture length (thus having the same intensity), but their permeability can be considerably different depending on how well connected the fractures are (Sanderson & Nixon 2015). Classifying nodes by their type is a useful measure of the connectivity of a fracture network. Our ternary plots show that when diffusion is fast, i.e. panels 1 in Figures 6.10a and 6.10b, almost all systems fall near the I vertex, with only a few systems developing Y nodes, and even fewer X nodes. This suggests that under these conditions melt migration mainly happens through porous flow. To obtain a well-developed network, the rate of melt generation needs to be faster than pressure diffusion. The fracture systems that show the highest connectivity are the ones with the highest melt viscosity and melt production rate. In general, our networks show a relatively higher number of Y nodes compared to X nodes. This might be explained by the fact that X nodes develop more easily if there are two sets of fracture orientations but also because they are slightly more difficult for our algorithm to detect. Nonetheless, Y nodes are still a good indicator of network connectivity.

The DBSCAN algorithm allows us to analyse fracture systems at a larger scale by defining damage zones as areas of localised fractures. Most parameters that describe the cluster of fractures show that an increase in viscosity or melt production rate corresponds to a larger number of clusters and a larger average size. In Figure 6.11a, the maximum number of clusters is observed for relatively high values of viscosity and melt rate but is followed by a decrease. When these variables are the highest, the fracture networks that develop are so well connected that they merge into larger and larger clusters (see the abundance of Y and X nodes in Figure 6.10), hence the decrease in the number of clusters. An advantage of classifying fractures into clusters is that, at a small scale, individual fractures follow the orientation of the elastic grid; therefore, many of them would show an orientation of ± 60°. However, by using a clustering algorithm, we obtain numerous clusters that show a 90° angle (Figure 6.11c), consistent with the orientation of hydrofractures (mode I fractures).

There have only been a few attempts to quantify the geometry of melt (Brown 2010). One of the most common ways to achieve this is used in outcrops with layer-parallel melt veins, where measurements of vein spacing and thickness are taken along one-dimensional line traverses perpendicular to the main foliation (Brown et al. 1995, Marchildon & Brown 2003, Brown 2010, Yakymchuk et al. 2013). This method measures the relationship between the thickness and spacing of the melt veins and has been used to tell if the layer geometry is the result of a self-organising system (follows an exponential distribution) or controlled by external factors, usually deformation (Marchildon & Brown 2003, Yakymchuk et al. 2013). As the protolith in our numerical experiments is isotropic and not subject to external deformation, the resulting fracture geometry does not resemble this pattern. Figure 6.12 confirms that a heterogeneous medium can develop patterns that are significantly different. However, the goal of our study is to assess the relative role of the rates of melt production and pressure diffusion, so a homogeneous and static solid medium allows us to isolate their contribution to the fracture network.

The amount of fracturing can be a good indicator of how easily melt can flow. However, melt migration is most efficient when it is able to segregate into larger structures (Sawyer 2001, Marchildon & Brown 2003). Therefore, we also need to consider how they are connected (ternary diagrams in Figure 6.10) and the orientation of the main structures (average cluster angle, Figure 6.11c). Larger structures are also less sensitive to small-scale anisotropy (Diener et al. 2014), which makes our results more robust, as we do not include a foliation in our setup.

Classifying fractures into clusters allows us to better link the occurrence of fractures to the rock's ability to drain melt and understand conditions that allow the transition from porous flow to channelised flow. For example, clusters with a higher elongation make melt migration more effective and are formed by more viscous melts (Figure 6.5d). These large-scale structures can be interpreted as the channels that allow efficient melt migration, suggesting that the opening of such structures requires a high fluid pressure increase compared to pressure diffusion.

6.4.3 Geological Implications

Whereas melt viscosity can be predicted based on composition, it is much harder to estimate the rate of melt production (Petford 1995, Etheridge et al. 2021). If it is possible to determine the viscosity in a natural migmatite, the length and localisation of fractures could be used as a factor to estimate the rate of melt generation.

Granitic melt compositions usually have a high viscosity and are considered to be fertile, meaning that they potentially have high melt production rates. They usually show more developed leucosome networks (Weinberg 1999, Petford 1995) and have a coarser grain size, which means that the melt distribution tends to be heterogeneous. The porosity distribution in Figures 6.6b and 6.6c is compatible with these features, showing high spatial variability in the melt fraction. Such localisation of fluid pressure favours the formation and propagation of fractures in the host rock.

Low-viscosity melts usually correspond to mafic compositions, which also tend to be less fertile and are characterised by a smaller grain size. Natural examples of mafic environments do not usually show long and continuous melt networks. These features are compatible with our numerical experiments that have a low melt production rate and a low viscosity. We observed that they do not form extensive fracture networks, so melt migration occurs preferentially through porous flow. The pressure and porosity profiles of case 2 in Figure 6.6 (sub-figures *e* and *f*, fast fluid pressure diffusion) are much more homogeneous than in case 1, a behaviour consistent with a mafic composition.

In these two simple cases, both viscosity and melt rate favour either fluid pressure localisation (first example) or diffusion (second example). However, when one of the factors facilitates localisation and the other pressure diffusion, the interpretation of the pattern is less straightforward. In the case of a high melt rate (but a low viscosity), we expect a pattern with short fractures scattered throughout the area of partial melting (top left corner of Figure 6.8). They correspond to the areas with the highest melt generation but their propagation was hindered by the fast melt diffusion. Conversely, if pressure build-up was caused by a high melt viscosity, we expect to see localised fractures. The fact that they did not propagate suggests that the melt rate was low. This combination corresponds to the numerical experiments in the bottom right corner of Figure 6.8.

Our numerical set-up includes an isotropic solid medium which is a significant simplification of a natural-occurring rock. Heterogeneities and anisotropic structures in the host rock are very common and have an important control over the melt geometry (e.g. Allibone & Norris 1992, Brown & Solar 1998, Yakymchuk et al. 2013, Ganzhorn et al. 2016). However, using such a simplified material gives us useful insights into the role of the two investigated parameters. Further investigations will involve a host rock showing compositional layering and are discussed in Chapter 8.

6.4.4 Partial Melting in a Layer

Patterns are significantly different between a system that is able to drain melt (Figure 6.6) and one where the area of melt production is confined (Figure 6.12). This is in line with what was reported by Koehn et al. (2020) in the case of a confined layer with fluid overpressure. In these systems, fast diffusion inside the confined area allows the fluid pressure to become very high without forming fractures. Once the fluid pressure overcomes the lithostatic stress, a horizontal hydrofracture starts forming in the middle of the high-pressure zone, which is similar to what was described by Cobbold & Rodrigues (2007). Although the system with fast melt generation (Figure 6.12a) has a few of these layer-parallel veins, Figure 6.12b is the one showing the clearest example of such a structure. The high-pressure layer develops a horizontal dilating zone dominated by a horizontal hydrofracture that is similar to the structure in Koehn et al. (2020) and is also known as *beef* veins (Cobbold & Rodrigues 2007).

The numerical experiments where the production zone is limited to a single layer show the importance of melt drainage. Whether or not fluid pressure can diffuse away from its source layer also changes the effect that the other parameters have on the fracture patterns. In the unconfined case, a fast pressure diffusion leads to few, short and uniformly distributed cracks; on the other hand, an efficient diffusion in a confined area leads to the formation of a high-pressure homogeneous layer that results in localised, layer-parallel fracturing. This highlights the importance of the materials surrounding the melting area: their behaviour and physical properties have a direct impact on the mobility and spatial distribution of melt.

6.5 Conclusions

In this chapter, we used a hybrid DEM-continuum numerical model to investigate the interplay between melt pressure diffusion and melt production in fracture network formation within zones of partial melting. The key findings from this study are the following:

1. When melt production outpaces pressure diffusion, melt pressure localises, leading to the formation of extensive, well-connected fracture networks. These networks facilitate melt migration through brittle failure, creating permeable pathways for melt transport.

2. In systems where pressure diffusion dominates, fewer and smaller fractures develop. Melt migration occurs primarily via porous flow rather than through fractures, limiting the formation of extensive networks.

3. These behaviours indicate that melt pressure diffusion and production rates are critical factors in determining whether melt migrates through an extensive

fracture network or via diffuse porous flow.

4. Even in the absence of external deformation, fracture networks consisting of well-connected fractures can develop, provided the melt production rate significantly exceeds the rate of melt pressure diffusion. These networks were quantified using branch and node analyses and fracture clustering, highlighting their capacity to form efficient melt pathways.

5. The role of fluid pressure diffusion is further emphasised in systems where melting is confined to a single horizontal layer. In this case, pressure confinement drives the development of the longest and most continuous fractures in this study.

Chapter 7

The Influence of Extension on the Characteristics of Fracture Networks: A Numerical Study of Fracture Systems in a Partially Molten Rock

7.1 Introduction

External deformation is known to have an important effect on melt distribution and has often been considered a mechanism that enhances melt migration (e.g. Brown 2004, Cruden & Weinberg 2018). In a homogeneous and isotropic material, the two main factors controlling the type of fractures and their orientation are the strain state and fluid pressure (Nicolas & Jackson 1982). Partial melting often causes a volume increase, which results in a pressure increase in the newly-forming fluid (Rushmer 2001, Connolly et al. 1997). This pressure increase is particularly efficient if the rate of melt escaping its source is slower than the pressure increase caused by partial melting (Dell'Angelo & Tullis 1988). Consequently, the effective normal stresses decrease by an equal amount, facilitating fracture formation. The Mohr circle touches the failure envelope in different regimes depending on the orientation of the principal stresses,

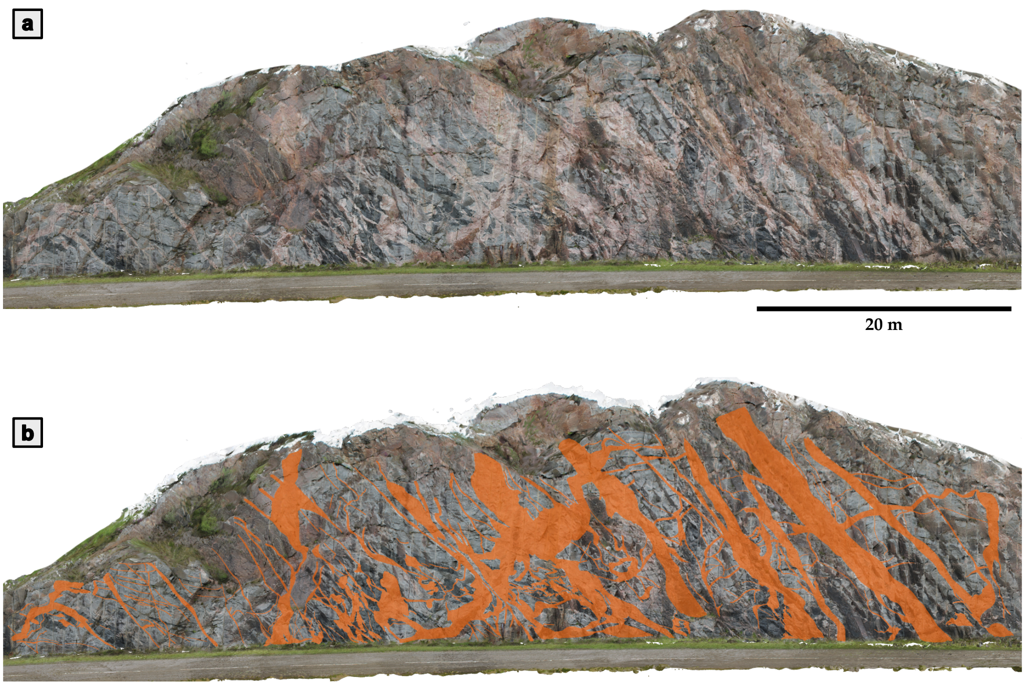

Figure 7.1: Photo of an outcrop situated at the boundary between the Laxfordian and the Rhiconich terranes, Scotland. (a) Full outcrop reconstructed using photogrammetry, (b) Same picture, with the (former) melt highlighted in orange.

the magnitude of the differential stress and the melt pressure. This mechanism can lead to the formation of well-developed fractures and dykes. Figure 7.1 is an example of a series of pegmatitic dykes found in the Laxfordian front at the boundary between the Assynt and the Rhiconich terrane, NW Scotland (Section 3.2 in Chapter 3).

If the fluid pressure is high and the deviatoric stress is small, the effective least principal stress moves to the left until it touches the failure envelope in the tensile region. This results in the opening of hydrofractures, which are typically vertical in a purely extensional environment (Bons et al. 2022). On the other hand, a large deviatoric stress and low fluid pressure result in shear fracturing. In extensional settings, fractures of this nature form at an angle of ±60° with σ_3, which is horizontal. If many fractures open, fluid pressure does not accumulate easily because the aperture of fractures allows a fast pressure diffusion and fractures are expected to remain relatively short (Nicolas & Jackson 1982). If both contributions from deviatoric stress and fluid pressure are significant, the failure criterion predicts that fractures have an angle between 60° and 90° (hybrid fractures, Bons et al. 2012). However, in complex environments such as melt production zones, fracture network patterns strongly depend on the interplay between pressure increase, stress state and the evolution of the porosity and permeability fields. These factors make the system highly dynamic, and it becomes essential to consider the feedback between the aperture of a fracture and the resulting pressure dissipation (Koehn et al. 2020). These principles are known in environments where the fluid is aqueous (e.g. Koehn et al. 2020) but can be even more complex when partial melting is involved, as it directly causes an increase in porosity and impacts the response of the solid fraction. Therefore, to accurately predict the effect of deformation, it should be considered together with pressure diffusion and melt production rate (Rushmer 2001).

Melt geometry has been used to interpret the stress state at the time of partial melting (e.g. Maaløe 1992). Another challenge involves the timing of melt and deformation, which means determining whether melting occurred during the whole deformation event, or in which phase it was active (Vanderhaeghe 2001). Many features have been used as evidence of synmigmatitic deformation. At the small (outcrop) scale, extensional deformation creates local pressure gradients that make melt move towards dilatant sites such as fractures and fold hinges (Brown & Solar 1998, Brown 2005). Small structures around larger leucosome layers can be used to determine the direction of shear (Maaløe 1992). Melt structures are used to understand their location relative to a larger fold (Allibone & Norris 1992). Foliation planes are a typical location for the localisation of melt (e.g. Vanderhaeghe 2001, Yakymchuk et al. 2013, Allibone & Norris 1992, Weinberg 1999) and can develop into melt-rich layers (Brown et al. 1999). However, the orientation of melt sheets at a larger scale is controlled by tectonic stresses and regional deformation (e.g. Sawyer 2001, Marchildon & Brown 2003). This causes melt-filled fractures to have consistent orientations and form conjugate sets (Davidson et al. 1994), allowing us to interpret the stress field (Brown & Solar 1998). Using field relations and the Mohr-Coulomb failure criterion, the angle between them has been used to estimate the differential stress (Davidson et al. 1994).

The link between melt distribution and the mechanisms that were active during partial melting is key to understanding under which conditions a migmatite formed. Deformation is considered a crucial mechanism that enhances melt migration, as it contributes to localisation (Brown & Solar 1998, Hasalová et al. 2008) and the formation of fractures (Davidson et al. 1994, Petford et al. 2000). However, melt migration has been observed to occur as a porous flow within both deforming and non-deforming settings (Stuart et al. 2016, Meek et al. 2019). This suggests that melt distribution patterns in tectonically active systems may share greater similarities with those in undeformed environments than commonly believed.

The goal of this chapter is to understand the relative effects of the deformation and melt production rates on the fracture patterns during partial melting. We performed systematic investigations that involved varying the two rates and performing numerical experiments for each combination of their values. The results were analysed using fracture network features and fracture orientations, and compared to field data.

7.2 Methods

The numerical code used in this chapter is the same as that described in Chapter 4 and Chapter 6, Section 6.2. Therefore, this section will focus on the differences from the previous chapter.

The primary addition to the setup of the numerical experiments is the inclusion of external deformation and for this study, we focus on extension. Figure 7.2 shows the boundary conditions used in this chapter (*a* and *b*) and the method of applying deformation (*c*). At each time step, the right-hand-side wall is displaced rightward at a constant rate, exerting stress on the solid particles. The other boundary conditions are the same as in Chapter 6.

Table 7.1 includes the values and ranges of the parameters used in this study. The first part of the table includes the parameters that were kept fixed in every simulation. The

Fixed Parameters

Parameter	Value	Units
Young's modulus[a]	3.5	GPa
Poisson's ratio[b]	1/3	-
Internal angle of friction[c]	30°	-
Tensile strength[d]	17	MPa
Rock density[e]	3000	kg/m^3
Melt density[f]	2500	kg/m^3
Melt viscosity[g]	10^5	Pa s
Initial Pore Fluid Pressure (λ_v) [h]	0.8333	-
Time step	10^8	s

Investigated Parameters

Parameter	Range	Units
Melt production rate[i]	0.1 - 0.9	% every melt spot (4 melt spots per time step)
External deformation (extension)[j]	10^{-16} - 9×10^{-16}	s^{-1}

[a] Koehn et al. (2019)

[b] Jaeger & Cook (1976), Flekkøy et al. (2002), Koehn et al. (2019)

[c] Jaeger & Cook (1976), Koehn et al. (2019)

[d] Koehn et al. (2019), Etheridge et al. (2021)

[e] Jackson et al. (2003)

[f] Jackson et al. (2003), gives a difference with the rock density of 500 kg/m^3 (Spiegelman 1993*b*)

[g] within the ranges in Spiegelman (1993*a*), Brown et al. (1995), Clemens & Petford (1999), Hack & Thompson (2011)

[h] derived from the density difference (Etheridge et al. 2021)

[i] gives 1% melt every $\sim 2.02 \times 10^4$ years, which is within the ranges calculated by Patiño Douce et al. (1990) and Jackson et al. (2003)

[j] Rutter (1997), Brown & Solar (1998)

Table 7.1: Parameters used in the model and sources for their values.

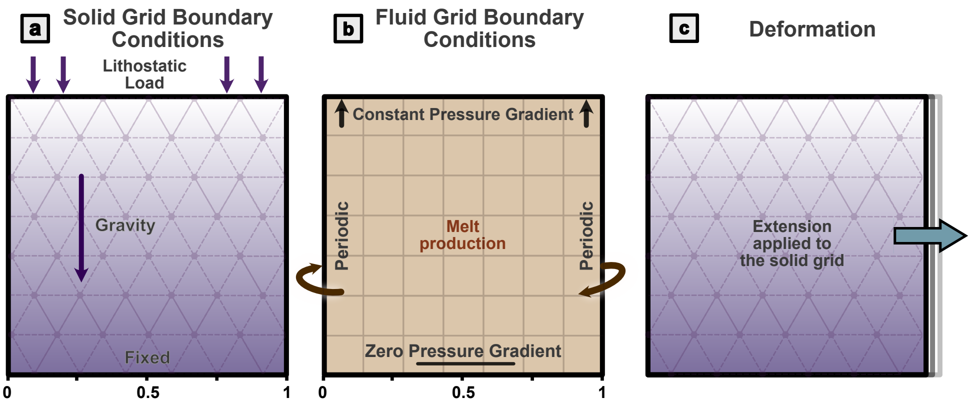

Figure 7.2: Boundary conditions for the two grids, (a) and (b), and deformation mechanism (c). Schematic representations of the solid particles (a and c) and fluid cells (b) represent the grid that the boundary and initial conditions are applied to.

second half of table 7.1 shows the ranges of the investigated parameters. Four points are chosen every time step to produce melt and each melt spot produces melt for 5 time steps. We performed numerical experiments for each combination of melt production and deformation rate but only report three representative examples in Figure 7.3, analysing them in detail in Figures 7.4 and 7.5. A selection of numerical experiments is shown in Figures 7.6, ordered by their melt production rate and deformation rate values, and 7.7, arranged so that each row displays the same finite strain.

7.2.1 Fracture Pattern Analysis

The fracture networks are analysed using the methods described in Sections 4.3.1 and 6.2.3. As the individual fractures are larger compared to the previous chapter, we do not consider clusters in our analysis. In this chapter, the orientation is calculated for each fracture instead of considering the orientation of a cluster of fractures. Rose diagrams are weighted by the fracture length.

7.3 Results

We varied the melt production rate and the deformation rate and ran a numerical experiment for each combination of parameter values. First, we show the evolution of three reference cases (Figure 7.3), one with a fast melt production but without external deformation (a), one with a slow melt production and fast extension (b), and one without melt production and only external deformation (c). Then we investigate the role of the two processes by showing a selection of melt rate and deformation rate values across their whole ranges (Figures 7.6 and 7.7). The fracture patterns are analysed using their orientation (Figure 7.7) and amount of fracturing (Figure 7.8).

7.3.1 Fracture development with time

Figure 7.3 shows the fracture pattern evolution with time for three cases at different extremes of the parameter ranges. Case a involves a system without external deformation but a fast melt rate (0.9% per melt spot per time step), case b is characterised by a slow melt production rate (0.1% per melt spot per time step) and a high deformation rate ($\dot{\varepsilon} = 9 \times 10^{-16}$ s^{-1}) and case c is a system only affected by external deformation but with no melt generation. Each scenario is shown at four different time steps, identified by their time step number (t_s).

In the first case (Figure 7.3a), fractures start as short and isolated (t_s = 10 ×10^3). Their location and orientation are mainly determined by the random distribution of melt points. As time advances (t_s = 15×10^3 and later), fractures grow and develop into larger clusters. In particular, the top half of the numerical domain shows the typical pattern of hydrofractures. Clusters grow in size and develop into a fracture network by propagating from individual high-pressure locations. In Figure 7.3a, the largest of these structures is found in the top left corner, highlighted by one of the green arrows in the t_s = 25×10^3 panel. Towards the end of the simulation, e.g. t_s = 25×10^3, some fractures have grown so much that they cover half of the size of the numerical domain. The lower half develops shorter cracks that show an orientation of ~60° or

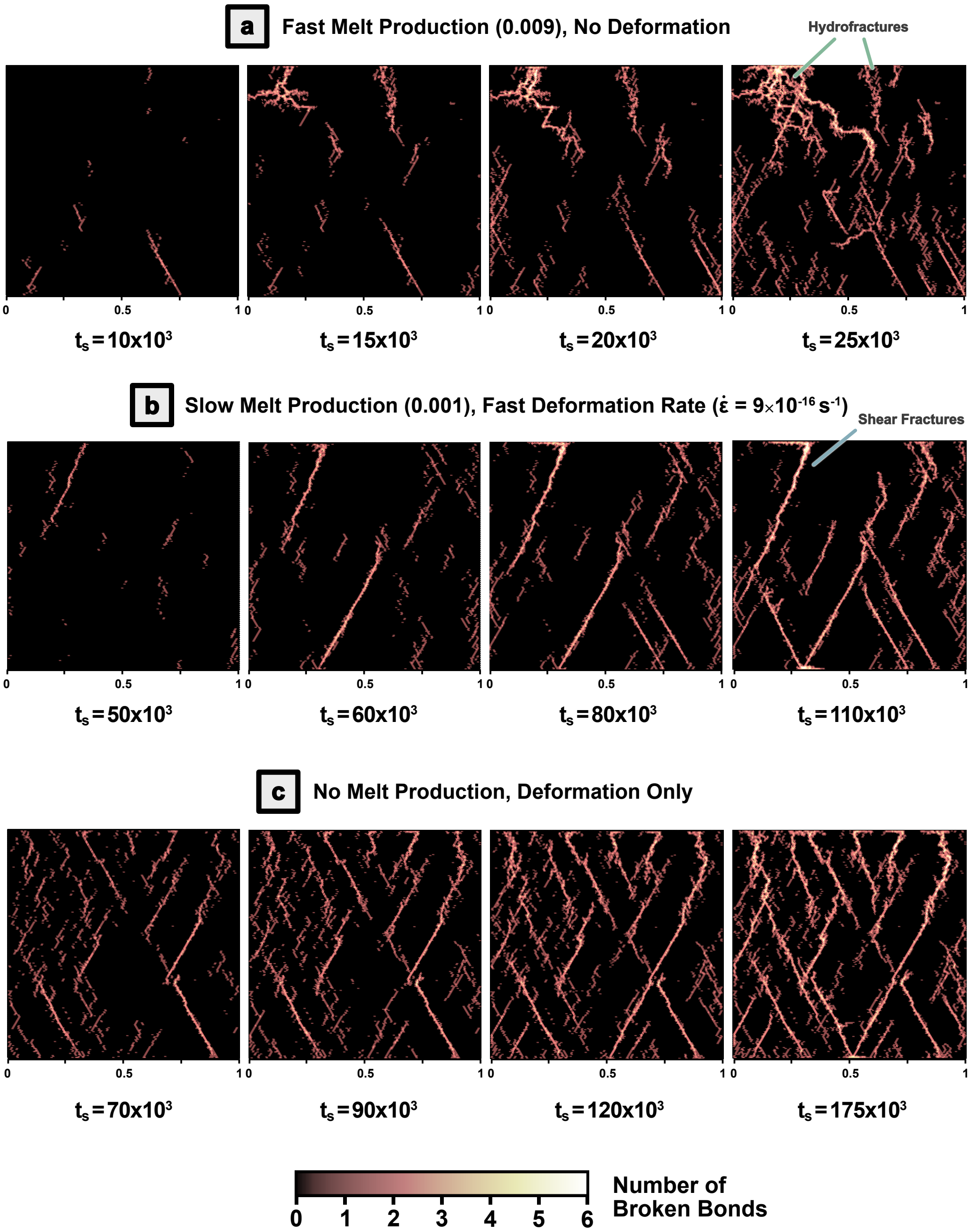

Figure 7.3: Fracture pattern evolution with time of three example cases. (a): fast melt production (0.9% per melt point per time step) and no deformation. (b): a system dominated by deformation and with a low melt production rate (0.1% per melt point per time step). (c): Only deformation is active, no melt production in the domain. Fractures are represented by the number of broken bonds around each elastic particle.

120°. Although some of these cracks are longer (e.g. the fracture in the middle of the $t_s = 10{\times}10^3$ panel), most of them remain short until at least $t_s = 20{\times}10^3$. The fracture patterns at $t_s = 15{\times}10^3$ and $t_s = 25{\times}10^3$ are also shown in Figure 7.4, together with the porosity field. At $t_s = 15{\times}10^3$, it is clearly visible that the fractures start forming in large areas of high melt fraction, especially in the upper half of the numerical domain. As time evolves (e.g. $t_s = 25{\times}10^3$), fractures propagate efficiently from the high-porosity spots, growing towards areas outside the initial melting areas.

The high correlation between porosity and fractures occurs in the lower half as well, though the propagation style is significantly different. In this case, fractures grow following a linear geometry at 60° and 120°.

The second case (Figure 7.3b) shows fractures that are again small in the initial time steps: the pattern at $t_s = 50{\times}10^3$ still shows short cracks except for a long fracture in the top left corner. At later time steps, e.g. $t_s = 60{\times}10^3$, the dominant geometry begins to change: Fractures are very straight and at a 60° angle, with few shorter fractures at 120°, making the fracture network strongly asymmetrical. This causes very few cross-cutting between fractures, as they are mostly parallel to each other. Some conjugate fractures start developing at $t_s = 80{\times}10^3$, as some 120° fractures start growing from the bottom-right area. The last time step shown in Figure 7.3b, $t_s = 110{\times}10^3$, shows long fractures that have a combination of both orientations. The main fractures are characterised by lighter colours, which indicate a higher number of broken bonds between particles and therefore a larger aperture. The system keeps forming new small cracks with time; however, these are rarely close to the main fractures. Figure 7.3b shows that in this case, the correlation between porosity and fractures is very low. Many locations have a high porosity, indicating partial melting, but are not affected by fractures. The porosity field is more heterogeneous compared to the one in case a.

Case c in Figure 7.3 shows a numerical experiment that undergoes extension without melt production. External deformation is applied at the same rate as in case b but, as the response of the solid grid is perfectly elastic, the rate does not affect the fracture

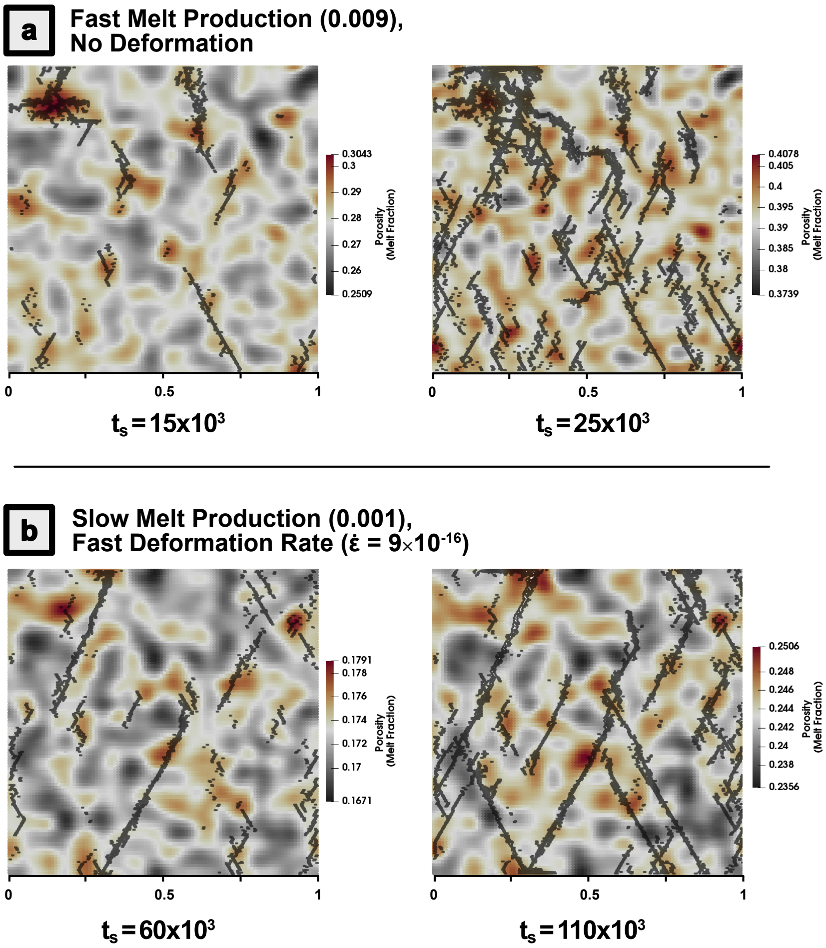

Figure 7.4: Porosity (background colour) and fracture pattern (black) for two of the time steps in Figure 7.3. (a): t_s = 15×10^3 and t_s = 25×10^3; (b): t_s = 60×10^3 and t_s = 110×10^3, corresponding to the second and fourth time steps in Figures 7.3a and 7.3b respectively. The colour palettes for porosity are different in each time step, as the differences are too large.

pattern. There are both short and long fractures and there isn't a dominant orientation, as both angles (60° and 120°) are equally present even at early time steps. The pattern is symmetrical in terms of fracture orientation and does not show areas with local preferential orientations.

Figure 7.5 shows the stress inside fractures of the three cases in Figure 7.3 at the last time step shown in each figure ($t_s = 25\times10^3$, $t_s = 110\times10^3$ and $t_s = 175\times10^3$ respectively). In case a, (Figure 7.5a) normal stress dominates fracture formation in many places. In

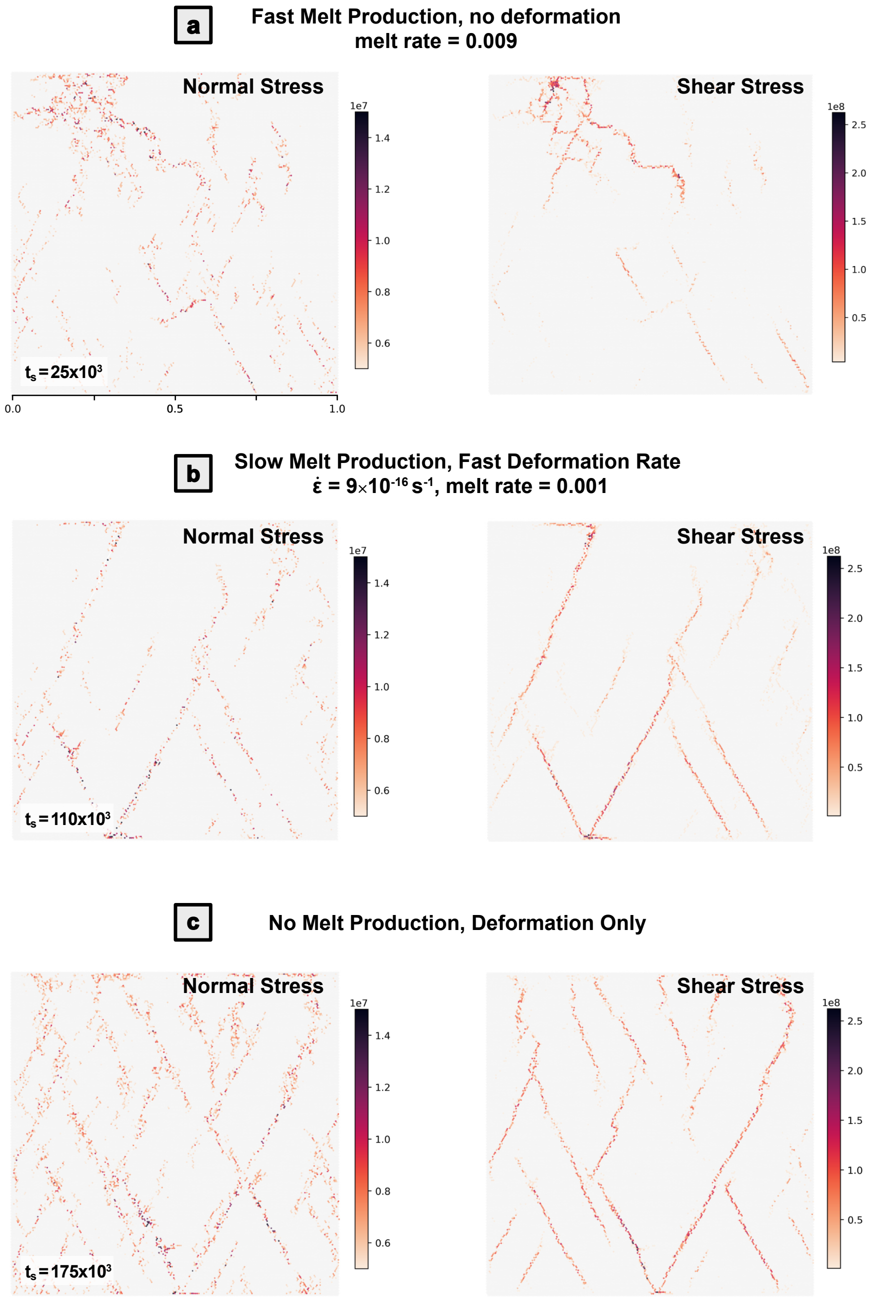

Figure 7.5: Stress inside fractures in Figure 7.3 for the three examples. The time steps correspond to the last time steps shown in Figure 7.3, so (a): $t_s = 25{\times}10^3$, (b): $t_s = 110{\times}10^3$, (c): $t_s = 175{\times}10^3$.

particular, normal stress is high in many of the hydrofractures in the upper half and in numerous smaller fractures. Shear stress is localised in the longer fractures only and is associated with fracture propagation.

Case b (fast deformation rate and some melt generation, Figure 7.5b) shows very high shear stress inside the long and straight fractures, while normal stress is higher in the broken bonds around the main fracture lines. Some of the fractures that are oriented roughly vertically also show normal stress only, while shear stress is limited to the continuous, 60° or 120° fractures.

Case c corresponds to a system with only extension (Figure 7.5c) and normal stress is relatively high in many places that correspond to fractures. However, such locations are discontinuous and often slightly off from the central line of each fracture. Instead, such a continuous line is visible in the shear stress panel, which shows clean traces of high values.

7.3.2 The Relative Roles of Extensional Deformation and Melt Production Rate

Figure 7.6 shows how the fracture patterns change as a function of the rates of deformation and melt production. Every square in Figure 7.6 represents a simulation which has a combination of a deformation rate value and a melt production rate value. Every column shares the same deformation rate, while every row has the same melt production rate and time step. The fraction of generated melt in every image is the same, so the time step is different between the four rows. However, keeping the time step constant on each row means that the finite strain in each numerical experiment depends on the deformation rate. A schematic representation of the finite strain for each panel is reported in Figure 7.6b, where each square represents a numerical experiment in Figure 7.6a.

At low deformation rates (left-hand side), fractures are mostly caused by melt production. They show patterns that are commonly associated with those of hydrofractures.

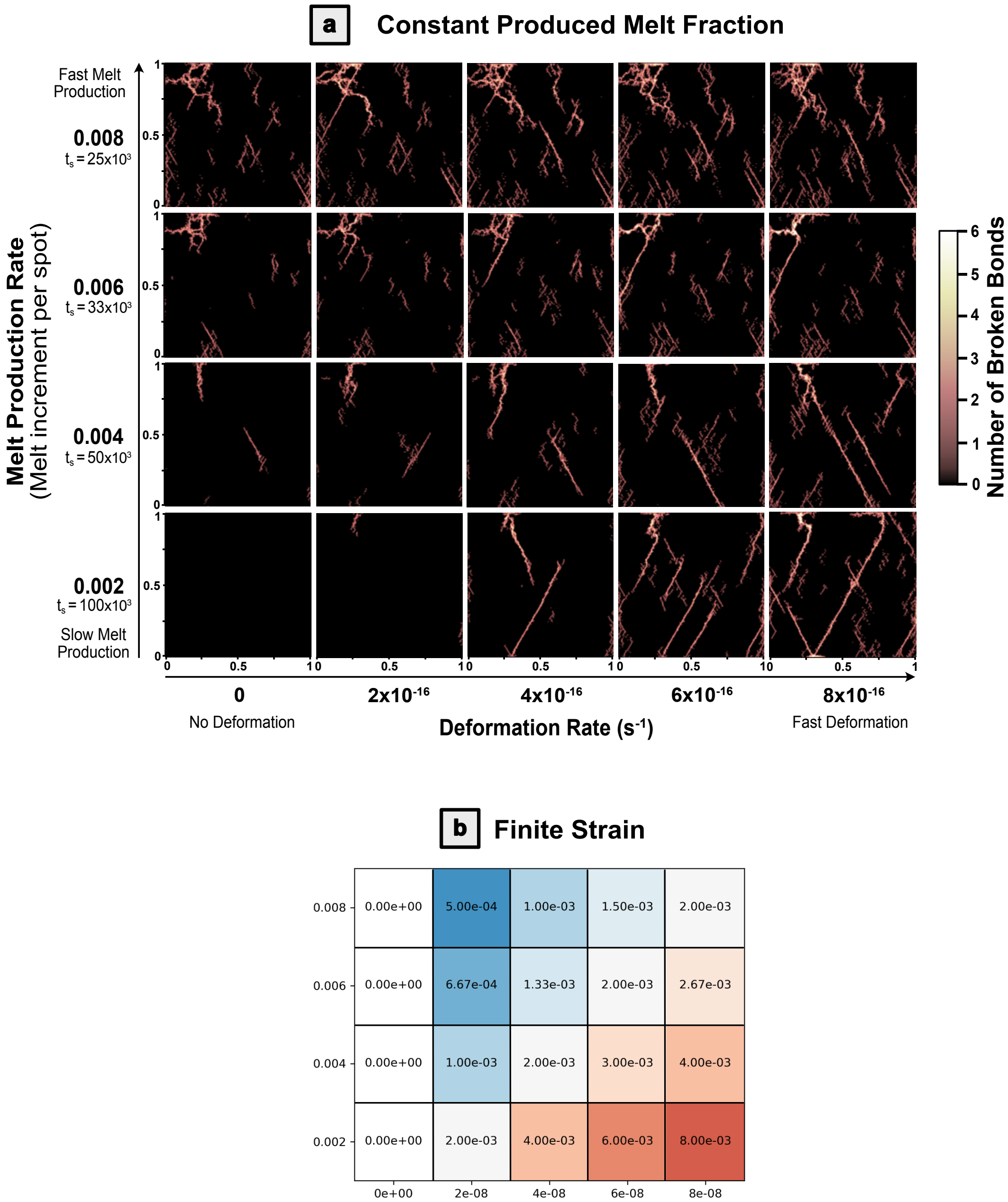

Figure 7.6: (a) Fracture patterns as a function of the deformation rate and the melt production rate. The images shown in the grid refer to different time steps in order to keep the amount of produced melt constant. (b): Diagram showing the finite strain of each of the above panels. As the deformation rate increases towards the right-hand side, the amount of strain in each row increases. $t_{ref} = 200 \times 10^3$.

This is especially visible in the upper half of each figure, as observed in Figure 7.3a, where a smaller amount of pore pressure is necessary to cause brittle failure. A fast melt production is associated with the formation of complex fracture networks (top rows, e.g. 0.008 per melt spot). Many fractures are clustered around a central point from which they originated and their orientation is random in these areas. When deformation is slow and the finite strain is small, such as in the top left corner, fractures are randomly clustered and do not have a dominant orientation. At higher rates of deformation (moving to the right-hand side), fractures start to show a preferred orientation, especially in the lower half of each figure. Lower values of melt rate (0.006 and 0.004) result in fractures that are highly elongated and have an orientation of either 60° or 120°.

Figure 7.7 shows numerical experiments that have produced the same amount of melt and have the same finite strain on each row. This is achieved by selecting simulations with the same melt rate to deformation rate ratio and the same finite strain (see Figure 7.7c). Figure 7.7a shows the resulting fracture networks, while Figure 7.7b includes the corresponding rose diagrams. Numerical experiments without melt production (d) and without external deformation (e) are also reported.

In the top rows of Figure 7.7a, melt production is fast compared to external deformation, making the ratio between the two rates high (e.g. ratio = 2.0 and ratio = 1.5). Fractures are clustered around a few locations, creating complex networks and exhibiting little fracture propagation. Although the most common values for their orientations are 60° and 120°, many secondary ones are also present (Figure 7.7b). At intermediate ratios, e.g. 1.0, a combination of hydrofractures and shear fractures is visible. The fracture network at $\dot{\varepsilon} = 4 \times 10^{-16}\ \mathrm{s}^{-1}$ includes a sub-vertical fracture in the top half of the domain that propagated downwards with little branching. At this value of $\dot{\varepsilon}$, some shear fractures start developing in the lower half. At high values of $\dot{\varepsilon}$ ($\geq 6 \times 10^{-16}\ \mathrm{s}^{-1}$), patterns become more and more affected by external deformation. They correspond to the peaks in the rose diagrams at 60° and 120°. These diagrams also show that as

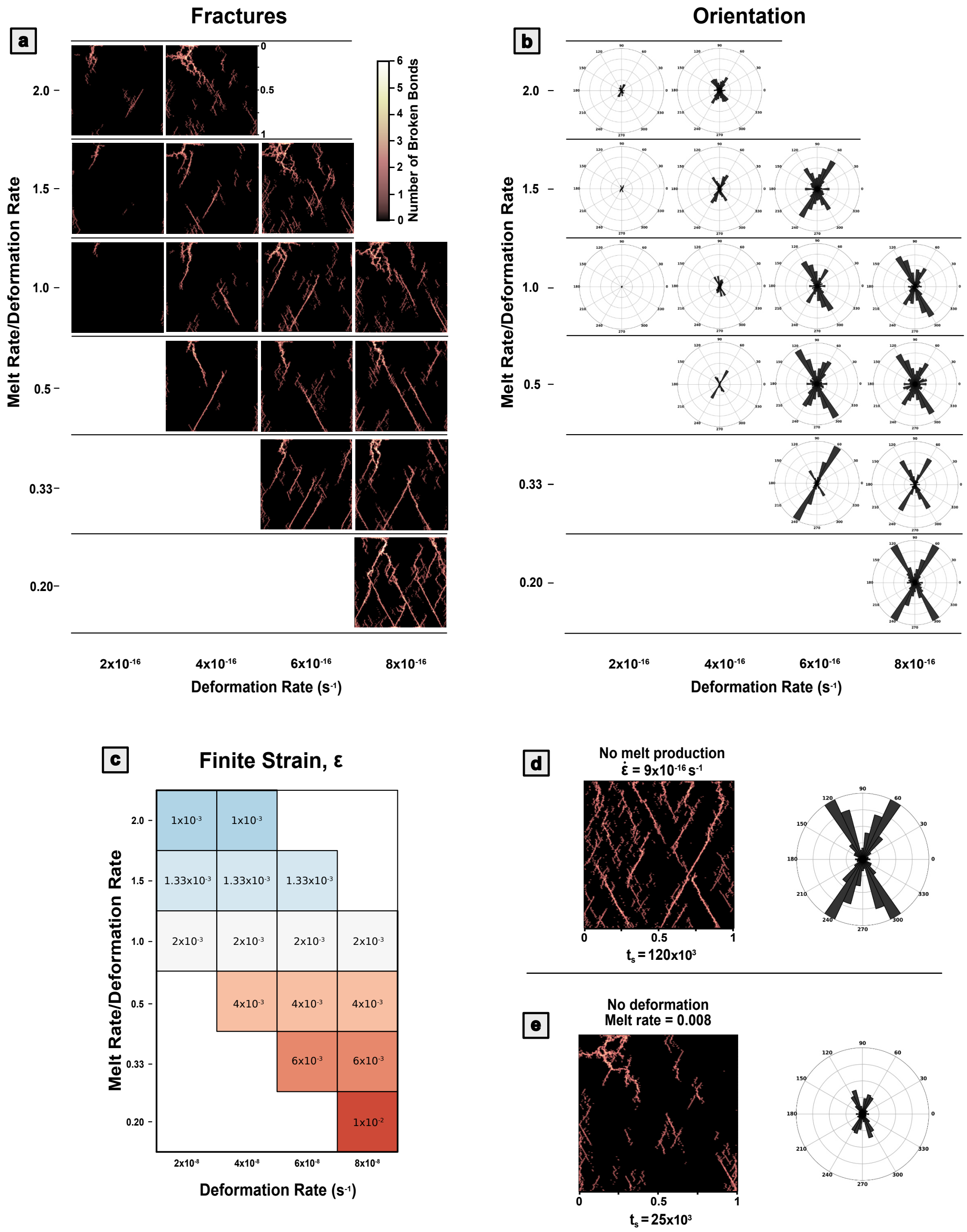

Figure 7.7: Fracture patterns and fracture orientation in a grid with the same generated melt fraction in all figures and the same finite strain on each row. (a): Fracture patterns showing the number of broken bonds around each particle of the solid grid. (b): Rose diagrams corresponding to each numerical experiment in (a). (c): Grid that shows the finite strain for the simulations shown in (a). D: Fracture network and its relative rose diagram in a system without melt production. The strain is the same as the highest strain in (a), i.e. the numerical experiment in the bottom right corner. E: Fracture network and rose diagram of a set-up without deformation. The generated melt fraction is the same as in the other panels and as in Figure 7.6.

the deformation rate increases, the patterns become more and more asymmetrical. In this type of network, shear fractures that form in the early stages randomly propagate in one of the possible orientations, which is then followed by the ones that develop later, causing one orientation to be more common than the other. Patterns that form at small ratios, i.e. the bottom rows of Figure 7.7a, include fractures that are highly elongated. Many of them include a system of parallel fractures with one dominant orientation, like the pattern with $\dot{\varepsilon} = 6 \times 10^{-16}$ s^{-1} and ratio = 0.33, which consists of many fractures with a 60° orientation. When the deformation rate is highest ($\dot{\varepsilon}$ = 8×10^{-16} s^{-1}) and the ratio is 0.20, the main orientation is 120°, the other value predicted by the failure criterion. Even though some fractures show the secondary orientation too, these are much shorter and discontinuous. They rarely cross-cut the longer ones, usually stopping when they encounter another fracture.

Fractures that form in a system without partial melting (Figure 7.7d) develop in both orientations predicted by the failure criterion in an extensional environment, 60° and 120°. They are elongated and form many cross-cuttings with each other.

Figure 7.7d shows a numerical experiment without external deformation and a fast melt production rate. The fracture network consists of clustered and shorter cracks with many different angles, usually closer to the vertical orientation.

The fracture networks were analysed in terms of the number of branches and dimensionless intensity (Figure 7.8). Each line in the plots consists of numerical experiments with the same melt rate/deformation rate ratio and corresponds to a row in Figure 7.7a. However, Figure 7.8 includes all the simulations, while previous figures only showed a selection.

When the deformation rate is low, the number of branches remains small (Figure 7.8a). If the deformation rate is higher, the number of branches significantly increases. This general trend is shared by most lines and is particularly strong for high ratios, which have a higher melt production rate. In particular, the higher the ratio, the higher the number of branches, with the exception of the lowest ratios. These are the numerical

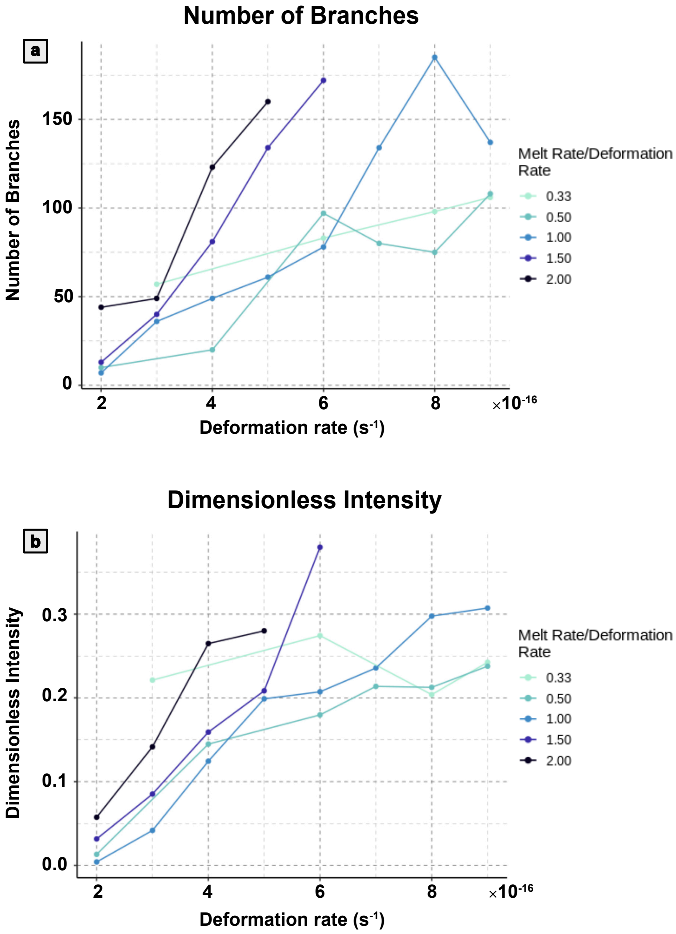

Figure 7.8: Number of branches and dimensionless intensity as a function of the deformation rate. Each data point represents a numerical experiment, with colours indicating the melt rate/deformation rate ratio. $t_{ref} = 200$.

experiments with the highest deformation rate relative to the melt production rate.

The dimensionless intensity parameter follows a similar trend: Slower deformation rates lead to smaller values of dimensionless intensity, while a faster deformation increases fracture intensity. However, systems with the lowest ratios are not affected by different rates of deformation.

7.4 Discussion

7.4.1 Fracture Network Development: Hydrofractures vs Shear Fractures

Our numerical experiments show that fractures develop different patterns depending on the rates of melt production and extensional deformation. The relative rates of these processes affect both the type of fracture and the networks that a system can develop.

Fractures generated by partial melting under static conditions have irregular shapes and a variety of orientations (Figure 7.3a). In the upper half of the domain, the system reaches failure conditions mainly because of the high pore fluid pressure: the stress state can be represented by a circle touching the failure envelope in the tensile region (red circle in Figure 7.9). Fractures in this area start from a central high-pressure point and grow radially. In the bottom half, where the confining pressure is higher, the fluid pressure alone is not high enough and shear stress contributes to the formation of fractures. This stress state corresponds to the purple circle in Figure 7.9.

The presence of different behaviours within the same region is a common occurrence, as natural migmatites often exhibit different modes of deformation even within the same outcrop (e.g. Davidson et al. 1994). A change in fracture style with depth has also been theorised on a larger scale, occurring when fractures propagate through different crustal levels (Weinberg & Regenauer-Lieb 2010, Sumita & Ota 2011). This variability is evidence of the sensitivity of migmatite patterns to pressure conditions and variations in the stress field.

The porosity field (Figure 7.4a) is mainly controlled by the melt spot locations and corresponds to the distribution of fluid pressure increase. The high correlation between porosity and fractures indicates that partial melting plays an important role in the initiation of the fractures. Although fractures in the lower part exhibit a 60° orientation, which could suggest the contribution of external deformation, the strong correlation between fractures and porosity in this region indicates that fluid pressure still plays a significant role. The significance of fluid pressure is confirmed by the stress inside the

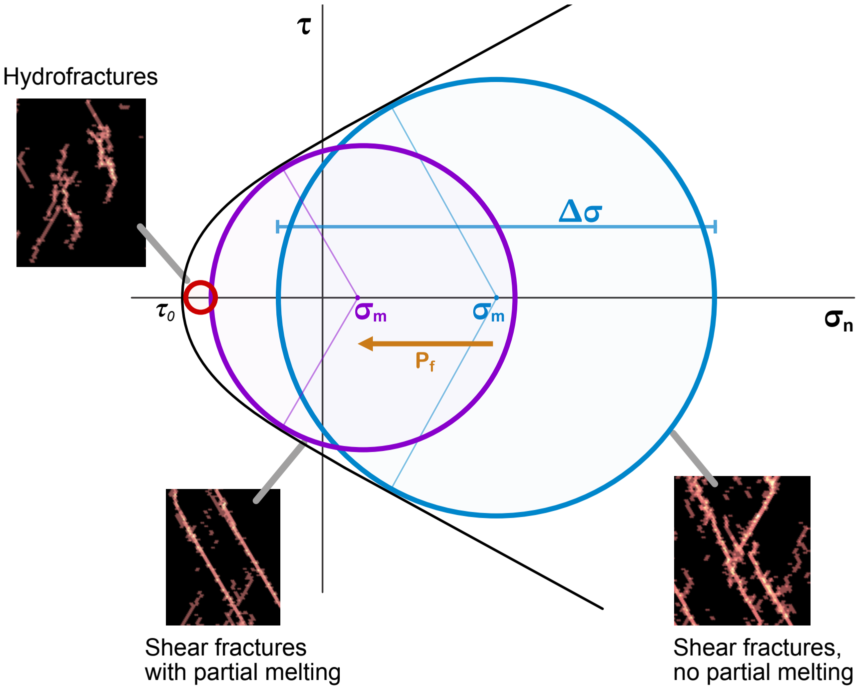

Figure 7.9: The different types of fracture linked to their position relative to the failure envelope. σ_n: Normal stress, σ_m: Mean stress, τ: Shear stress. P_f: Fluid pressure. Orange arrow: The effect of fluid pressure on the mean stress.

fractures (Figure 7.5a), which shows that the normal component is still prominent in the lower half.

If the host rock is not undergoing partial melting but is affected by extensional deformation (Figure 7.3c), the pattern consists of longer fractures that have both orientations predicted by the shear failure criterion. They propagate linearly in one direction and can form many cross-cuttings. Connectivity is created by fractures growing and cross-cutting each other rather than fractures developing radially from the same point. The stress state of fractures forming under these conditions can be described by the blue circle in Figure 7.9. In this scenario, fluid pressure does not contribute to fracture formation, therefore it takes a rather high differential stress ($\Delta\sigma$) to reach the failure criterion. As a consequence, fractures form at later time steps, after a larger amount of strain is applied to the system.

In systems where both deformation and partial melting contribute to the fracture patterns, a combination of hydrofracture and shear fracture styles is observed. When both mechanisms are active (case b), partial melting creates high-pressure spots that are the nucleation points of fractures. The external deformation then causes them to propagate, so most of the fracture growth is driven by the deformation. This behaviour is visible in Figure 7.4b, where the low correlation between fractures and porosity suggests that the contribution of the fluid pressure to fracture propagation was minimal.

Compared to case a, the porosity distribution is more heterogeneous. External deformation is known to favour the localisation of melt (e.g. Marchildon & Brown 2002), and the compaction of the host rock caused by the deformation can be interpreted as the mechanism that allows a stronger localisation of fractures. Partial melting also makes compaction more efficient, as it increases porosity. The combination of these two processes results in enhanced localisation of porosity and fractures. Compared to case c (deformation only), which shows a higher number of shorter cracks, case b (deformation and partial melting) exhibits fewer fractures per unit of area but with larger apertures, as indicated by the higher number of broken bonds.

Intermediate values of the two rates showed a progressive transition between hydrofractures and shear fractures (Figure 7.6). Rather than observing a distinct shift from one fracture style to another, patterns showed a gradual increase in the frequency of shear fractures with high deformation rates, and conversely, a higher incidence of hydrofractures as melting rates increased. Our numerical experiments do not indicate a specific threshold for a shift in fracture mode.

The relative contributions of deformation and melt production are also illustrated in Figure 7.7a, where the ratio between these processes is constant along each row. The higher the ratio, the stronger the contribution of melt production, with patterns including many hydrofractures. In rows with smaller ratios (i.e., bottom rows), the effect of deformation is more pronounced and leads to long and localised fractures.

Progressing from left to right along a row, both melt production and external deformation rates increase, outpacing the rate of pressure diffusion. In these systems, fracture patterns are complex and exhibit both shear and hydrofracture features. Conversely, panels on the left side of Figure 7.7a represent systems in which pressure diffusion rates are fast compared to those of melt production and external deformation. In these scenarios, rapid fluid pressure diffusion leads to the development of fewer fractures. However, once fractures begin to form, deformation processes facilitate their propagation, allowing these fractures to extend considerably.

7.4.2 The Influence of the Rates of Melt Production and Deformation on Fracture Orientation

When hydrofracture is the dominant fracture style, the resulting orientations tend to be more random or vertical (Figure 7.7e), aligning with fractures that develop in the tensile region of the failure criterion. This randomness in fracture orientation is caused by a very low differential stress. In this case, the stress state is effectively reduced to a point in Mohr space and the fractures exhibit no preferred orientation (Cosgrove 1995). As fractures open and grow, displacements in the host rock cause local stress perturbations. In the absence of a strong external stress field, these changes affect fracture growth, resulting in deviations from the theoretical orientations (Weinberg & Regenauer-Lieb 2010). This behaviour is exemplified in the upper regions of systems with elevated melt production rates and low deformation rates (e.g. Figure 7.3a). A high fluid pressure value has been associated with complex melt networks characterised by a high tortuosity (Brown et al. 1999) and chaotic networks (Reichardt & Weinberg 2012). Both geometries are similar to our numerical experiments where a high melt rate caused a high fluid pressure.

In scenarios dominated solely by deformation, without partial melting, both orientations predicted by the failure criterion are present (Figure 7.7d). The resulting patterns show several cross-cuttings. If the fluid pressure is low, fractures are expected to be short: The aperture of a fracture favours fluid pressure diffusion and inhibits fluid pressure build-up, which does not promote fracture propagation (Nicolas & Jackson 1982).

When both deformation and partial melting contribute to the fracture network, there are two possible angles (±60° if the fluid pressure is low, higher angles if the fractures are hybrid). However, we observed that one orientation may be slightly favoured. Once the first fracture has formed and developed, the volume of rock adjacent to the fracture compacts, which hinders the opening of fractures in the immediate proximity. The host rock compaction is enhanced by partial melting, as it increases porosity. As a consequence, the host rock can more easily accommodate the movement caused by the opening of a fracture. This increases the difficulty of fracture initiation in compacted areas. The sequence of processes involves (1) initial fracture formation, (2) compaction in the areas around the fracture, and (3) subsequent fracture formation that aligns parallel to the first, creating a consistent orientation pattern within the fracture network. This suggests that the first fracture to form determines which of the two possible orientations will be favoured in a specific area.

Melt-filled fractures with a preferred orientation have also been reported in the literature. Nicolas & Jackson (1982), argues that series of fractures with the same orientation (*en-echelon*) are common in systems with a relatively high melt pressure. Davidson et al. (1994) observed conjugate sets, suggesting that fracture orientation was controlled by external deformation, but one orientation was appearing more frequently than the other.

7.4.3 Application to field analysis: The example of the Laxfordian Front

We analysed the melt distribution in the outcrop in Figure 7.1, which corresponds to location S01 in Chapter 3, Figure 3.2. The melt geometry is analysed using the same methods applied to the numerical results and the orientations are shown using rose diagrams. The full area was divided into four smaller regions and the melt vein orientation is shown for each region individually, as well as in the whole area (bottom diagram). The angle that the foliation forms with the horizontal is reported in red in the last diagram. In general, dykes in this location show a dominant orientation and a secondary one, both cross-cutting the foliation. The presence of a main orientation is particularly visible in region *b* and *d*, where most dykes are parallel to each other. Their rose diagrams resemble the ones from the numerical experiments where both the external deformation and fluid pressure had an important role on the fracture network (Figure 7.7b, e.g. ratios 0.5 and 0.33). Region *c* shows a much wider variety of orientations. In this region, a large dyke with an orientation that is almost perpendicular to the main one cuts through the parallel dykes. The many orientations and the irregular shape of the cross-cutting dyke suggest the presence of higher melt pressure in this area.

Due to the orientations of the dykes with respect to the foliation, we can argue that melt was present during deformation, likely when the Laxfordian shear zone was active. Alternatively, this can be a signature of extensional deformation shortly after terrane amalgamation during which melt was generated. Continuity between most vein types suggests that the melt was part of the same network and the veins contained melt at the same time (Marchildon & Brown 2003, Weinberg & Regenauer-Lieb 2010, Yakymchuk et al. 2013).

7.5 Conclusions

This study has shown the relative roles of deformation and melt production in the development of fracture networks within partially molten rocks in the lower and middle crust. The key findings from our numerical experiments are as follows:

1. Systems dominated by melt production form unorganised networks of hydrofractures, mainly characterised by vertical or randomly oriented fractures. These result from high fluid pressure reducing the effective normal stress, favouring brittle fracturing.

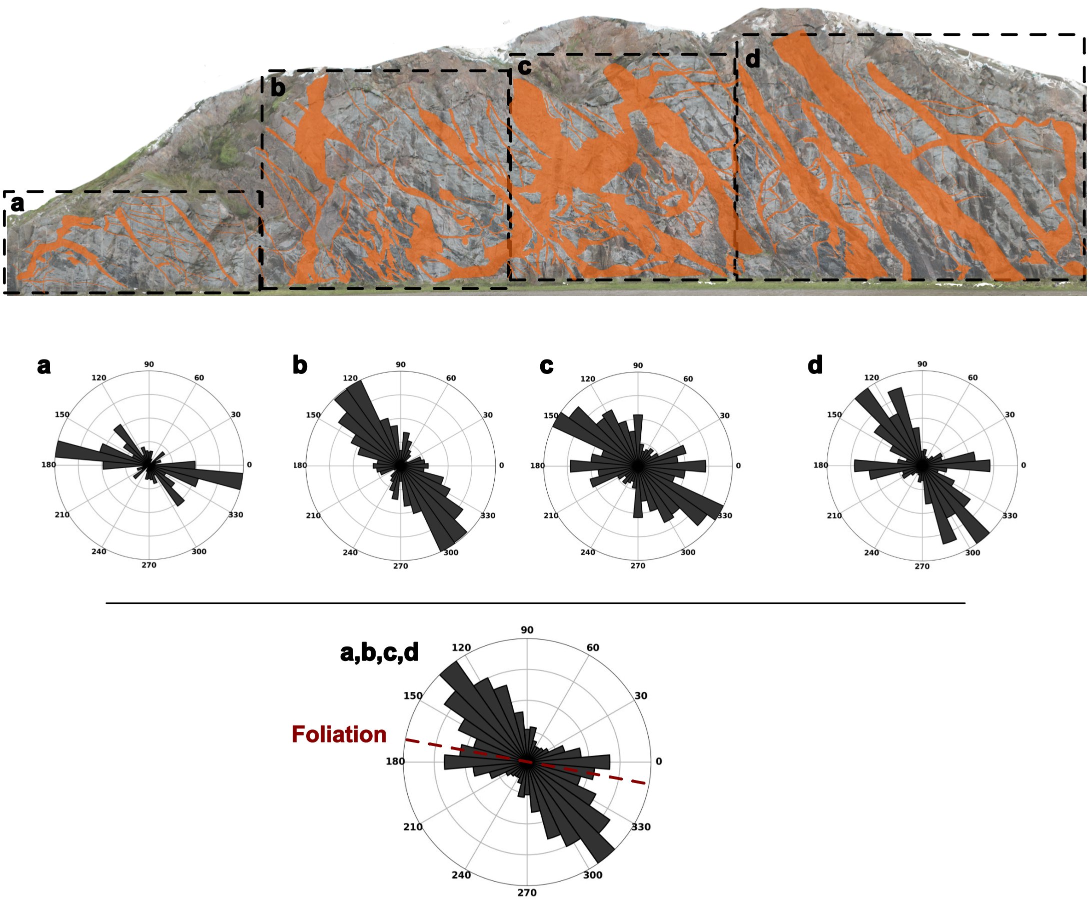

Figure 7.10: Interpretation of former melt of the outcrop showed in Figure 7.1 and analysis of melt orientation. The outcrop was divided into four smaller regions, whose rose diagram is reported under each section. The rose diagram at the bottom refers to the whole area.

2. When deformation is active in a zone of partial melting, the increased porosity enhances rock compaction, favouring fracture localisation, propagation and organisation. Fractures align into parallel rather than conjugate sets, resulting in asymmetrical structures. Fracture networks in these environments can include both hybrid and hydrofractures, with their proportion depending on the relative rates of melting and deformation.

3. Systems undergoing deformation without partial melting develop conjugate sets

of fractures that exhibit both possible orientations predicted by the failure criterion.

4. Based on our numerical experiments, we interpret the dyke network from an outcrop in the Laxfordian front, Scotland. The strong preferred orientation of the main set of dykes suggests an active role of both external deformation and high melt pressure. This supports the interpretation that the dykes formed while deformation was active.

Chapter 8

The Role of Compositional Layering in Fracture Networks of Partially Molten Rocks: A Numerical Study

8.1 Introduction

Compositional layering has often been considered a key parameter in the distribution of melt (e.g. Sawyer 2001, Marchildon & Brown 2003, Ganzhorn et al. 2016). Variations in composition lead to differing rates of melt production (Cruden & Weinberg 2018). These variations also translate into differences in permeability, as a faster melt production results in higher porosity and, consequently, increased permeability. Such layers can therefore act as preferential pathways for melt flow (Brown & Solar 1998).

Small-scale structures are often controlled by compositional or structural anisotropies, leading to the formation of stromatic migmatites (e.g. Diener et al. 2014, Marchildon & Brown 2003, Yakymchuk et al. 2013). Many studies have focused on the distribution of foliation-parallel melt veins, measuring spacing and thickness, showing that layer-parallel leucosomes can be scale-invariant and form a self-organized critical system (e.g. Tanner 1999, Marchildon & Brown 2003, Soesoo et al. 2004, Brown 2005, Bonamici & Duebendorfer 2010, Yakymchuk et al. 2013).

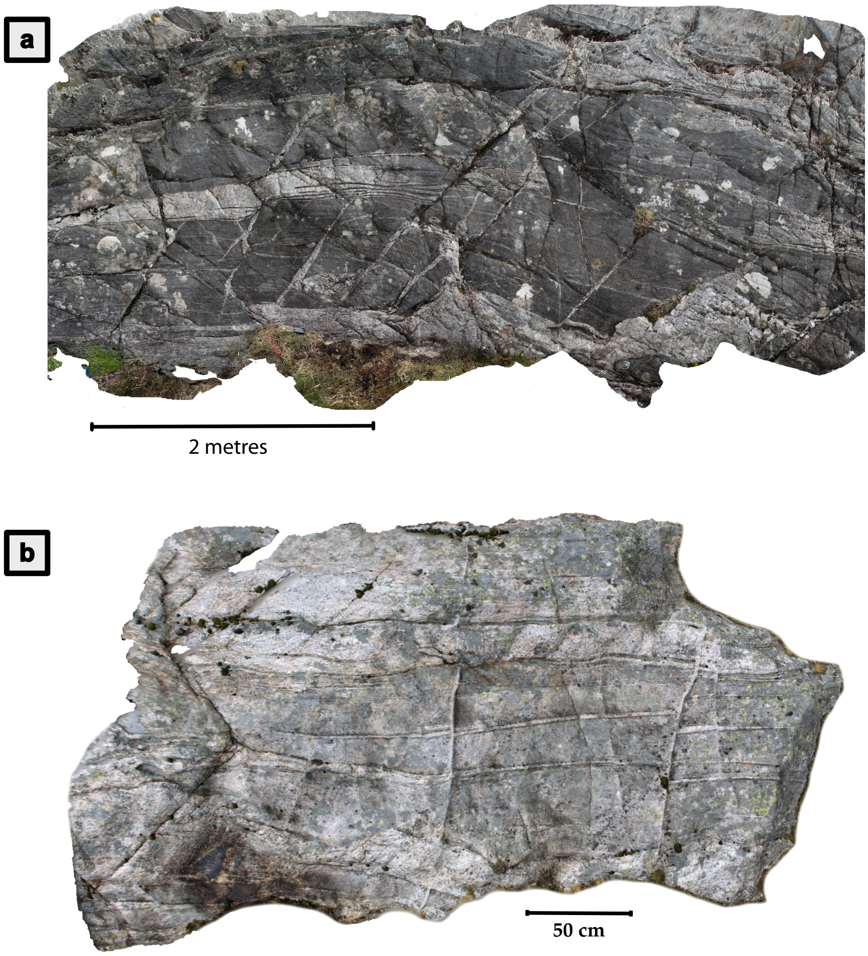

Figure 8.1: Examples of migmatites that show melt following compositional layering. (a) the main layers are horizontal and parallel to the foliation, but many veins follow a secondary orientation (NW Scotland). (b) Melt veins mainly following the foliation, with a few cross-cuttings (Rogaland region, Norway).

Layer-parallel melt can be cross-cut by discordant veins and these two types of melt bodies often exhibit petrographic continuity, meaning that they have similar mineralogy and microstructures (Yakymchuk et al. 2013, Marchildon & Brown 2003, Diener et al. 2014). This feature suggests that they hosted melt at the same time and therefore formed a single melt-extraction network.

Figure 8.1 includes two examples of migmatites where the location of the leucosome was strongly influenced by the structure of the host rock. In the first one (Figure 8.1a), the melt structure is characterised by large horizontal layers that follow the foliation. Smaller melt veins connect the main ones following secondary orientations. Most of these smaller structures exhibit the same angle, with only a few conjugate fractures. The second example (Figure 8.1b) comprises very thin foliation-parallel veins cut by high-angle veins.

In systems where melt distribution is controlled by planar structures, layer-parallel melt is considered ineffective at moving melt over large distances. Therefore, the presence of larger-scale cross-cutting dykes greatly increases the melt network's connectivity and ability to drain melt (Marchildon & Brown 2003, Yakymchuk et al. 2013). These larger dykes have been observed to be less sensitive to the local anisotropies and are controlled by the regional stress instead (Oliver & Barr 1997, Brown 2005).

Less attention has been given to the relationship between layer-parallel and cross-cutting leucosomes. In this study, we investigate the conditions that control the formation of layer-parallel and cross-cutting veins. We performed numerical experiments of layered rocks, with and without extensional deformation. The strength of the compositional layering was controlled by the contrast in melt production rate between different horizontal layers. For each compositional layer setup, simulations with different melt rates were run. We observed that the fracture pattern is the result of the relative contribution of these two factors. A high melt production difference between fertile and infertile layers favours layer-parallel localisation of fractures, while scenarios controlled by deformation exhibit numerous cross-cutting fractures.

8.2 Methods

The numerical code used in this chapter, *Latte*, is described in Chapter 4 and 6.2. The set-up and parameters are the same as in Chapter 7, table 7.1. The primary difference in this study is the set-up for melt generation. Compositional layering was introduced by imposing a melt rate contrast between horizontal layers, as illustrated in Figure 8.2. Layers with higher melt production rates (*fertile* layers, labelled A in

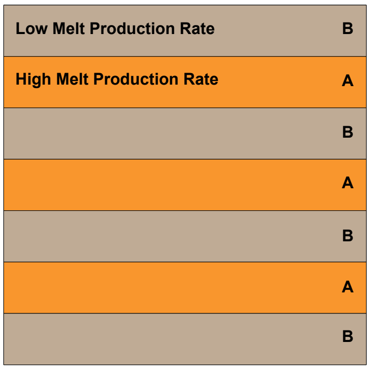

Figure 8.2: Set up of melt rates for the numerical experiments.

Figure 8.2) alternate with layers of lower melt production rates (labelled B). The melt rate contrast is expressed as the ratio of the rates between the two layer types, R_A/R_B where R_A represents the higher rate and R_B the lower rate. The average melt rate in the whole numerical domain remains fixed across all simulations and is distributed between the layers to achieve different contrasts. This means that for the same time step, all simulations will have produced the same melt fraction, regardless of the melt rate contrast.

8.3 Results

Figure 8.3 includes three scenarios and the time evolution of their fracture patterns. Three time steps are shown for each case, with each time step displaying the distribution of broken bonds and vertical profile of porosity (green), pore fluid pressure (blue) and the sum of broken bonds along each row (red).

In the first scenario (Figure 8.3a), the melting rate of the fertile layers is three times higher than the rate in the other layers. The faster rate causes fluid pressure to accumulate in the fertile layers, leading to increased differences in porosity and permeability, as illustrated in the vertical profiles. The first fractures that begin to open (e.g. $t_s = 1{\times}10^4$) are predominantly parallel to the layer boundaries, though some vertical fractures are also observed. As time advances, these fractures propagate horizontally, occasionally also developing some high-angle offshoots ($t_s = 10^4$). Only when the fractures have reached a significant length do they start growing outside of the layers with the fast melt production ($t_s = 18 \times 10^3$). In this scenario, most of the fractures develop inside the fast-producing layer, which is also shown in the vertical profile on the right-hand side of Figure 8.3a. These vertical profiles also show how the contrast in porosity and pore fluid pressure keeps growing with time. The red lines display the sum of fractured bonds in the solid grid on each row. This profile shows the clear difference between the amount of fracturing inside and outside the fertile layers.

Scenario *b* involves a fast deformation (extension) rate and a small contrast in melt production rate. Fractures start opening at a 60° or 120°angle ($t_s = 8 \times 10^3$), indicating that they are shear fractures caused by the applied extension. Fractures are locally parallel. Fractures parallel to the layer boundaries, similar to the ones in scenario *a* only start forming at later time steps, when shear fractures are already well developed. As the melt rate contrast is only 1.5, the porosity and pressure profiles (on the right-hand side) exhibit smaller variations. The amount of fracturing is only slightly higher in the fertile layers, as shown in the small peaks in the red line.

The third scenario (Figure 8.3c) is a combination of the first two. Here, both the melt production contrast and the deformation rate are high. The fracture patterns show behaviours linked both to high contrast (horizontal) and to a fast deformation (60° and 120°). In the initial time steps (e.g. $t_s = 8 \times 10^3$), many shear fractures are already developing, but they are not as straight as the ones visible in scenario *b*. They always start from a layer with a fast melt production.

Two types of fractures are present. The first one is nearly vertical and perpendicular to the layer boundaries. When the first type propagates into the less fertile zone, its orientation switches to the one typical of a shear fracture, 60° or 120°. This happens as soon as the fracture propagates outside the innermost region of the fertile layer. The second type opens parallel to the layer boundary. These horizontal fractures are only present in the fertile layers. Although these fractures are similar to the ones in scenario

b, they have a much higher tortuosity. As the time steps increase ($t_s = 10 \times 10^3$), this fracture type starts propagating outside their source layer too. Similarly to the first type, the orientation of the fractures once they propagate outside the innermost zone is roughly 60° or 120°. At advanced time steps, the combination of all of these different fractures and their orientation creates a complex network. Fractures between layers tend to have the same orientation, forming locally parallel sets. The vertical profiles of porosity and pore fluid pressure show great variability again, like in the first scenario. The fractures are also highly localised, however, they show a more gradual transition at the boundaries between fast and slow-producing layers.

8.3.1 The Role of the Melt Production Rate Contrast and the Deformation Rate

Figure 8.4 includes a larger selection of numerical experiments with varying deformation rates and melt rate contrasts. Figure 8.4a shows the fracture patterns, Figure 8.4b their corresponding orientations, with orange representing fractures inside fertile layers and grey fractures outside such layers.

At the lowest melt rate contrast, $R_A/R_B = 1$, there is no difference in melt production between layers, resulting in a homogeneous host rock. In this case, deformation is the dominant process and only shear fractures form. At higher deformation rates, the number and length of the fractures increase.

With an intermediate contrast, $R_A/R_B = 2$, and a low deformation rate, fractures predominantly follow the layer orientation and only a few fractures extend beyond the layers. At higher deformation rates, shear fractures between the fertile layers become more prominent. These discordant fractures maintain a roughly consistent orientation when they propagate and are only slightly affected by the presence of the layers. Rose diagrams 8.4b illustrate this trend. At $\dot{\varepsilon} = 0$, fractures are mainly sub-horizontal and within the fast-melting layers (in orange). At $\dot{\varepsilon} = 1{\times}10^{-15}$ s^{-1}, horizontal fractures remain dominant, but fractures at 120°also begin to develop, predominantly within

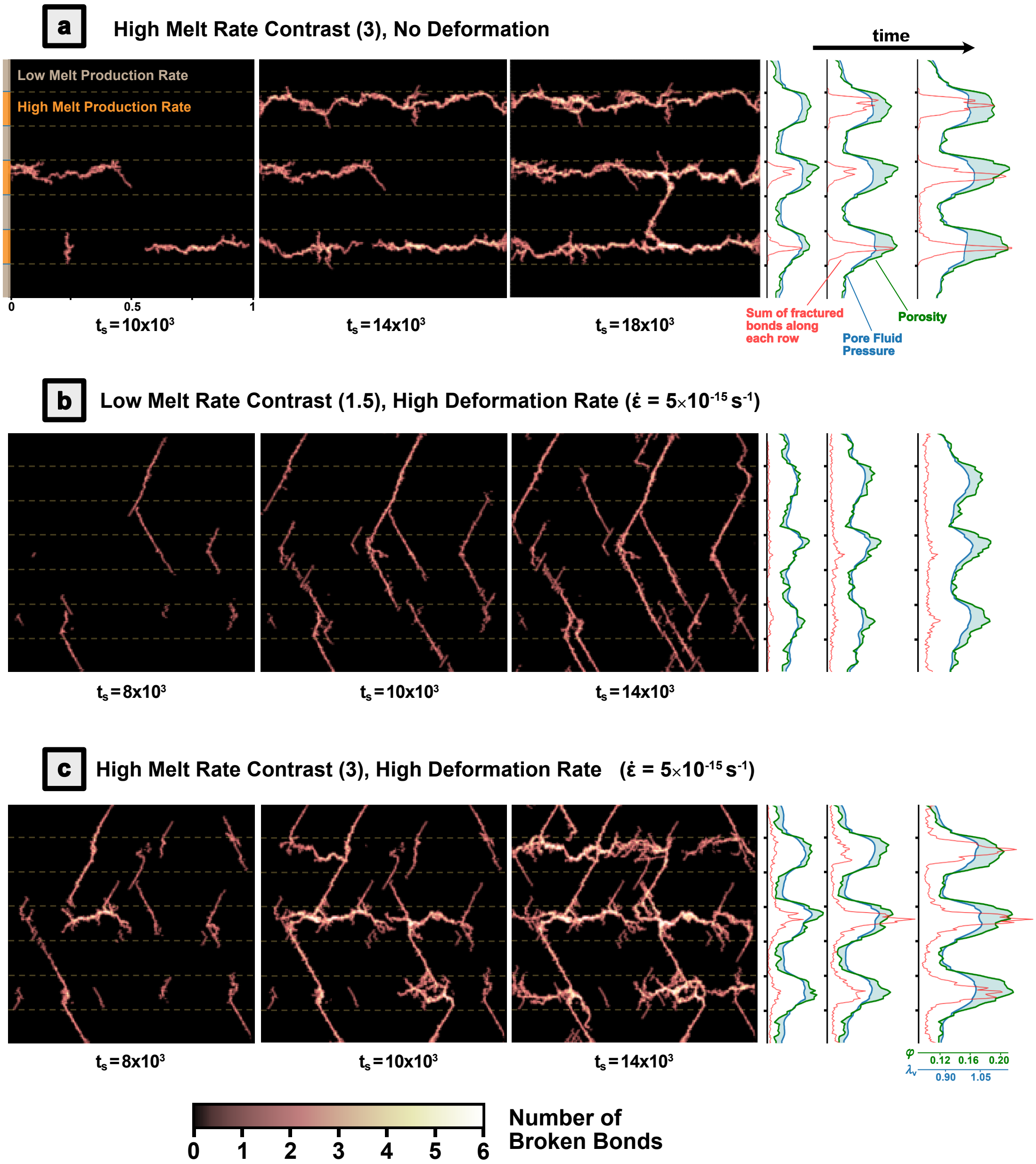

Figure 8.3: Time evolution of fracture patterns in three scenarios involving layers with different melting rates. Dashed lines indicate the boundaries between the different types of layers. Fracture patterns are shown for three selected time steps. On the right-hand side, the corresponding vertical profiles of porosity (green) and pore fluid pressure (blue) are shown, along with the total number of fractured bonds for each row. (a) High melt rate contrast: The melt rate is three times higher in the fertile layers. (b): Low melt rate contrast with a high deformation rate. (c) High melt rate contrast combined with a high deformation rate.

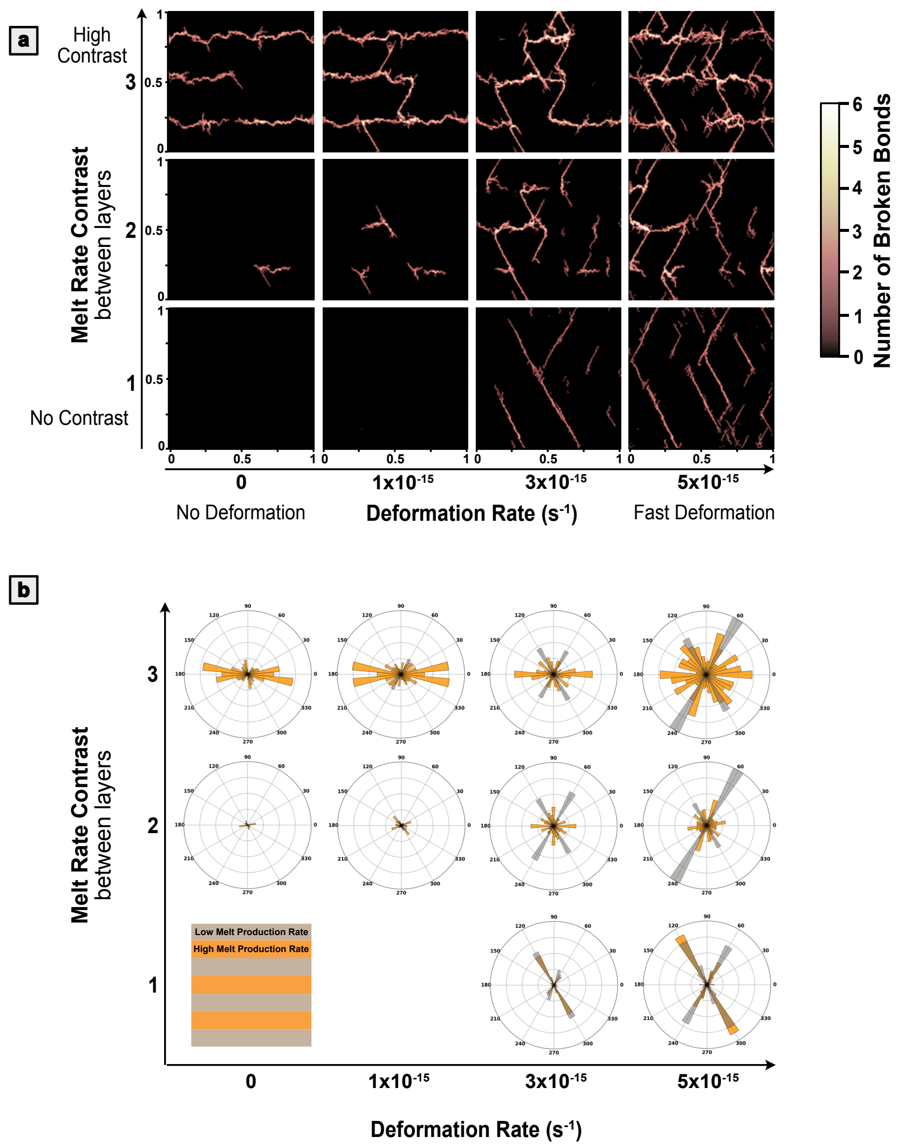

Figure 8.4: (a) A selection of figures showing fractures for different melt rate contrasts and deformation rates. (b) the corresponding rose diagram showing the orientation of the fractures. Orange bars represent fractures in the fertile layers, grey bars the ones with a lower melt production rate. All figures are from the same time step, $t_s = 14 \times 10^3$.

the layers. At higher deformation rates ($\dot{\varepsilon} = 3{\times}10^{-15}$ and $\dot{\varepsilon} = 5{\times}10^{-15}$ s^{-1}), fractures increasingly occur outside the layers, with orientations clustered around ±60°. In particular, when the deformation is high ($\dot{\varepsilon} = 5{\times}10^{-15}$ s^{-1}), shear fractures outside the fertile layers are the most common type. Fractures within the layers show a wider range of orientations rather than being solely parallel to the boundaries.

At the highest melt contrast, $R_A/R_B = 3$, in the absence of deformation ($\dot{\varepsilon} = 0$), most fractures are parallel to the layer boundaries. The corresponding rose diagram displays no grey bars that would indicate fractures outside the layers. Orientations are primarily sub-horizontal with a minor peak at 90° representing a few vertical fractures. As the deformation rate increases, shear fractures within the fertile layers develop. These fractures increase the network's tortuosity and branching, making the fracture patterns more complex. The distribution of fracture orientations within these layers progressively switches from completely sub-horizontal to include a variety of orientations. Outside the fertile layers, fractures are clustered around ±60°. At the highest deformation rate, $\dot{\varepsilon} = 5{\times}10^{-15}$ s^{-1}, which is also shown in Figure 8.3c, fractures within the fast-producing layers display highly heterogeneous orientations. In contrast, fractures outside these layers show a strong preferred orientation at 60° with a secondary peak at 120°.

Figure 8.5 was created by classifying the fracture data by layer type and calculating the percentage of fractures occurring outside the fertile layers. This metric provides an indication of how the fracture network develops independently of, or breaks away from, the compositional layering.

The ratio of fractures occurring in the slow-melting layers to the total number of fractures increases with the deformation rate and decreases with the melt rate contrast. Higher melt rate contrasts, represented by lines in lighter colours, lead to fewer fractures forming outside the fast-melting layers. Higher deformation rates in such systems increase the number of fractures in the slow-melting layers, though this remains relatively low compared to scenarios with a low melt rate contrast (darker lines). For example, at low contrasts ($R_A/R_B = 1.5$ or 2), the percentage of fractures outside the fertile layers already reaches 20-30% at deformation rates of $\dot{\varepsilon} = 1 \times 10^{-15}$ s^{-1} or $\dot{\varepsilon} = 2 \times 10^{-15}$ s^{-1}.

In the case of a homogeneous protolith ($R_A/R_B = 1$), the fracture ratio reaches 57.7%

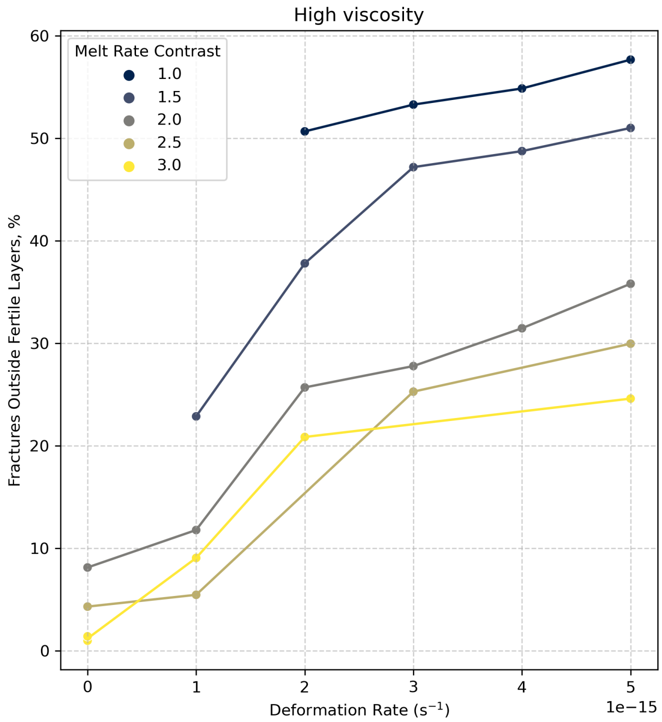

Figure 8.5: Percentage of fractures outside the fertile layers as a function of the deformation rate (x-axis) and for different melt rate contrasts (line colour). The time step is the same as the one used in Figure 8.4, $t_s = 14 \times 10^3$

at $\dot{\varepsilon} = 5{\times}10^{-15}$ s^{-1}, which is consistent with a spatial distribution of fractures that is independent of compositional layering. This value is very close to the proportion of the area occupied by the four slow-producing layers relative to the total area (57.1%).

8.3.2 Variations in Layer Geometry: Thickness and Spacing

The layer thickness and spacing were investigated in a few scenarios, shown in Figure 8.6. Two contrasts in melt production rate were chosen: in the first case (top half of the figure), the fertile layers melt three times faster than the other layers, and in the second case the contrast is only 1.5.

The first variation of the geometry involves modifying the thickness of layers. Instead of three layers with high melt rates, two thicker layers were defined, with their combined area set equal to that of the original three-layer configuration. This setup was chosen so that the total melt production was the same for both cases. In this case, wider fractures develop, as indicated by their lighter colour in the figure. In the second configuration, the central layer is removed, which causes fracturing to become more localised. The fractures are more parallel and less wavy, with fewer bifurcations compared to the original geometry.

When deformation is introduced, the fracture networks remain strongly influenced by the high melt rate contrast in both cases. For thicker layers, fractures exhibit numerous ramifications and high tortuosity within the layers, though the overall pattern is not substantially different from the reference case. In the scenario without the middle layer, deformation is more localised within the remaining layers and straight shear fractures propagate through the infertile region.

For low melt rate contrast, $R_A/R_B = 1.5$, without deformation, thicker layers exhibit stronger fracture localisation and higher tortuosity. The absence of the central layer leads to a similar fracture geometry but with more continuous fracturing within individual layers.

When deformation is added, the thicker layers show a relatively similar pattern to the reference case. Many shear fractures form between the layers, most of them cutting through the layers. Additionally, layer-parallel fractures develop where larger cross-cutting fractures encounter the layer boundaries. In the scenario with thin layers and no central layer, deformation is most strongly localised within the remaining layers. The resulting fracture network in the area between the two layers consists of only two long cross-cutting fractures. The top layer develops an extensive layer-parallel fracture accompanied by numerous shear fractures propagating from the central horizontal fracture.

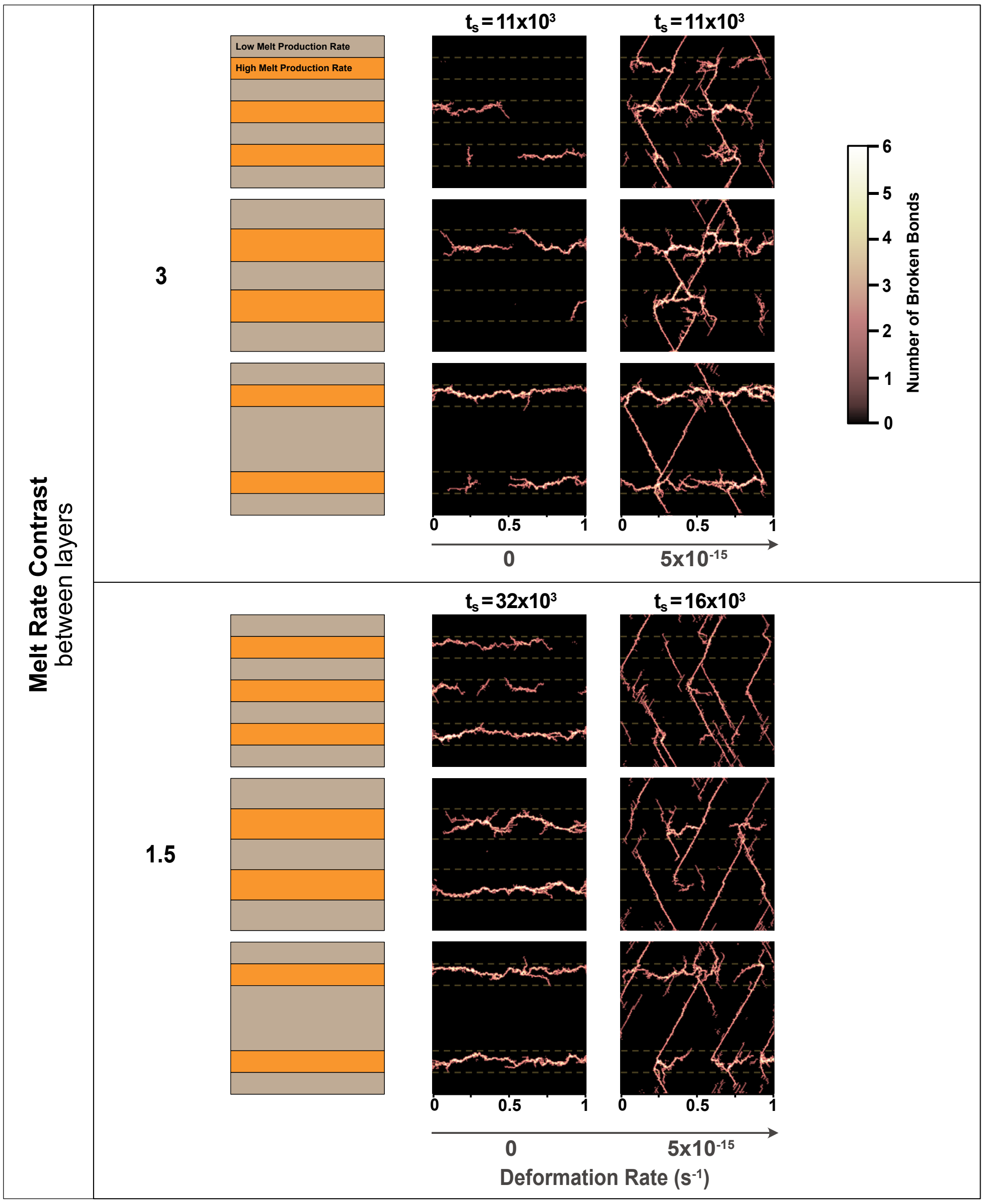

Figure 8.6: Fracture patterns for different layer geometries. Two melt production rate contrasts are used (3 and 1.5). The first geometry is the one used in previous figures, the second case includes thicker layers, the third case is the same as the first one but the middle layer is missing. Note that the time step is different between sets of figures.

8.4 Discussion

Our results investigate the distinct and characteristic signatures that compositional layering and deformation rate leave in the fracture networks within a melt-producing zone. In general, our numerical experiments show that a strong contrast in melt production rates between layers leads to the development of layer-parallel melt structures. Conversely, when deformation is dominant, the fracture network becomes less sensitive to compositional layering, resulting in discordant shear fractures.

In cases where the melt production rate varies significantly between layers (e.g. vertical profiles in Figure 8.3a and 8.3c), this contrast also translates into differences in permeability. As melting progresses, fertile layers become increasingly porous and permeable, enhancing the permeability contrast. The fertile layers become sealed between low-permeability layers and are unable to effectively drain melt, leading to fluid pressure accumulation. Once this pressure exceeds the lithostatic stress, the system develops a horizontal dilating zone dominated by a horizontal hydrofracture that is similar to the structure in Koehn et al. (2020) and is also known as *beef* veins (Cobbold & Rodrigues 2007). These phenomena are observed in scenario *a* (Figure 8.3a), where layer-parallel fractures develop first, followed by shear fractures propagating from the fertile, fast-producing layers. Shear fractures only form after the horizontal fractures are well-established, resulting in extensive layer-parallel fracturing and only a few discordant structures. In scenario *a*, the geometry of the migmatite is strongly controlled by the compositional structure. This pattern is consistent with observations by Bonamici & Duebendorfer (2010), who described well-developed compositional layering with minimal cross-cutting dykes at high angles. Their study also noted that low-angle dykes often form anastomosing structures, bending and adjusting their orientation to align with the compositional layering. Similar behaviour is observed in our numerical experiments, particularly in cases with thicker layers (Figure 8.6, middle case) or where the melt rate contrast is relatively low (Figure 8.6, contrast between layers 1.5).

Scenario *b*, dominated by extensional deformation due to the high deformation rate,

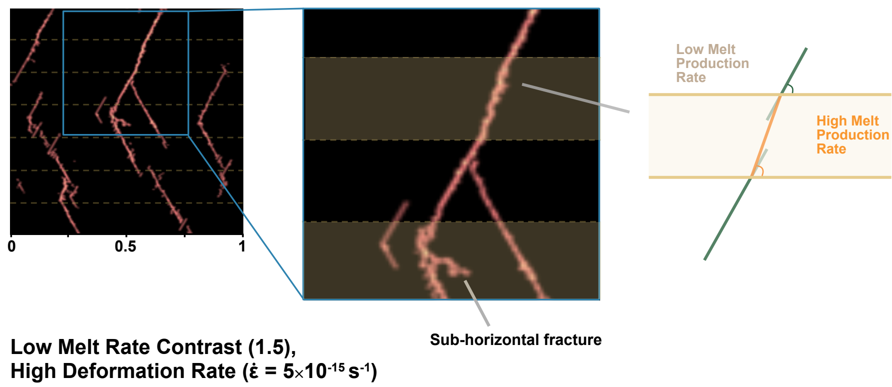

Figure 8.7: Magnified view and schematic drawing of shear fracture behaviour when it intersects a fertile layer. The figure corresponds to $t_s = 10 \times 10^3$) of case b in Figure 8.3, characterised by a moderate melt rate contrast (1.5), and a high deformation rate ($\dot{\varepsilon} = 5 \times 10^{-15}$ s^{-1}).

shows a different behaviour. In this case, shear fractures form first, creating an extensive network of discordant veins. When a fracture intersects a layer, two phenomena can occur (simultaneously or independently) and they are illustrated in Figure 8.7. The first possibility is the formation of a new fracture branching from the main shear fracture. This secondary fracture propagates subparallel to the layer boundary, resulting in a high angle relative to the main shear fracture. The mechanism behind this fracture is similar to that observed in scenario a. The second phenomenon involves a change in fracture orientation as the fracture propagates within the fertile layer (shown on the right-hand side of Figure 8.7). The increased contribution from melt pressure causes its angle to steepen, making it closer to a vertical hydrofracture. Overall, since deformation is the dominant process, the influence of layering is reduced. This phenomenon is frequently observed in larger structures that cut through structural anisotropy (Sawyer 2001, Marchildon & Brown 2003). Changes in dyke propagation angles when crossing the interface between materials with differing properties have also been described in the literature, e.g. Maccaferri et al. (2010), Rivalta et al. (2015).

Scenario c combines aspects of the first two cases, producing a complex network of both horizontal hydrofractures and discordant shear fractures. The shear fractures, which cross-cut layers, facilitate melt drainage from the high-pressure layers, enabling some melt pressure diffusion. As a result, fracturing within the fertile layers is less pronounced compared to the case without deformation and the horizontal fractures are less continuous.

As discussed in previous sections, when the difference in melt production rates between layers is high, fracture networks predominantly consist of horizontal structures. This is evident in the rose diagrams in Figure 8.4b, which also illustrate a transition from predominantly horizontal orientations to progressively higher angles as deformation increases.

Shear fractures forming in infertile layers often exhibit parallel orientations within the same area. This behaviour is interpreted as being similar to observations in Chapter 7, where the presence of melt promotes the development of a dominant orientation between the two possible shear fracture directions. This preferential orientation is particularly pronounced in scenarios where melt generation significantly influences the fracture network, such as in the upper half of the high deformation rate ($\dot{\varepsilon} = 5\times10^{-15}\ \mathrm{s}^{-1}$) and high melt contrast ($R_A/R_B = 3$) case shown in Figure 8.4a.

Melt distributions that predominantly follow compositional layering do not lead to efficient upward melt migration (Bonamici & Duebendorfer 2010). While this type of structure can facilitate small-scale melt migration, it lacks the connectivity required for larger-scale transport. Efficient upward migration relies on discordant veins that intersect layer-parallel veins, enabling melt to migrate upwards (Marchildon & Brown 2003). These discordant structures serve as efficient conduits for melt extraction, eventually forming larger, interconnected networks capable of transporting melt to higher crustal levels.

Our numerical experiments highlight the significant role of external deformation in the development of these discordant veins. For instance, shear fractures that cross-cut fertile layers create critical pathways for melt to escape otherwise isolated layers. This process shifts melt flow from predominantly layer-parallel structures to discordant conduits, promoting upward migration and supporting the development of larger vein systems.

8.4.1 The Influence of Layer Thickness

We made small adjustments to the layer setup to study how these geometries influence the fracture network. Thicker layers tend to produce more waviness in fractures, while thinner layers promote greater localisation due to their more confined geometry. In thinner layers, the stress switch is more pronounced, enhancing the development of localised fracture networks, as described in Koehn et al. (2020) and Cobbold & Rodrigues (2007). Conversely, thicker layers behave more like scenarios without layering, where fracture geometry and orientation are more similar to those of hydrofractures.

Under conditions of high deformation, however, the influence of layer thickness is less pronounced. The numerical experiments with the modified geometries did not differ from the reference cases in a significant way. Fracture patterns are primarily dominated by discordant shear fractures, with only minor contributions from smaller, layer-parallel structures.

8.4.2 Interpreting Natural Migmatites: Importance of Considering Presence of Compositional Layers with Different Melt Fertility

Our numerical experiments demonstrate the strong influence that compositional differences have on the melt distribution patterns. This finding provides an explanation for the frequent occurrence of compositionally parallel melt veins, which may not necessarily result from intrusion or the exploitation of pre-existing pathways. Rather than being driven by the stress regime, as proposed for some migmatites, these patterns are more likely a consequence of pre-existing heterogeneities within the rock.

Figure 8.8 shows the outcrop in Figure 8.1a, alongside an interpretation of its melt

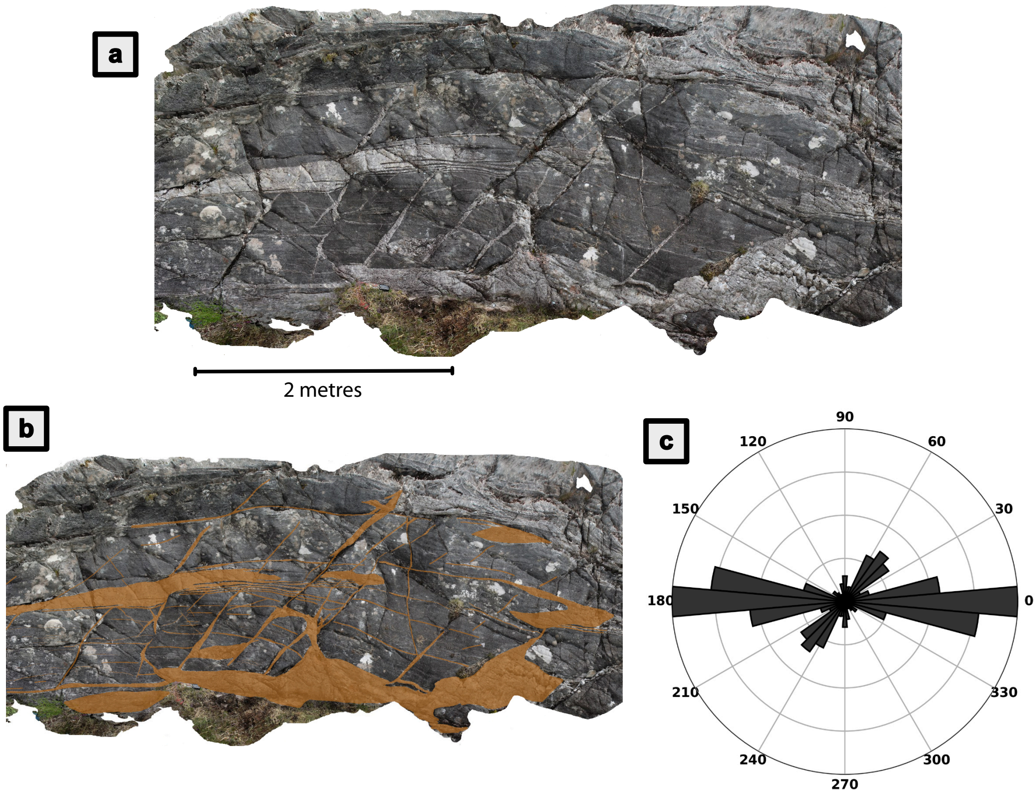

Figure 8.8: (a) Photo of the outcrop in Figure 3.4a. (b) Interpretation of the melt distribution sketched on top of the original photo. (c) Orientation of the melt veins. Angle = 0° corresponds to the orientation of the main layers.

distribution (b) and the orientation of the melt veins (c). This outcrop shows a few horizontal melt layers and several offshoots propagating from the main layers into the host rock. The orientation was analysed with the same method used on the fractures in the numerical experiments and the angles are measured from the thicker layers. In this diagram, we can identify a dominant horizontal orientation and a single additional peak in vein orientation. Our numerical results suggest that such a configuration likely requires significant deformation combined with relatively high melt pressure.

Figure 8.9 presents a second example of melt following compositional layering. This outcrop, located in the Rogaland area of Norway, features a foliated host rock with multiple melt bodies. The largest of these are pegmatitic veins that follow the ori-

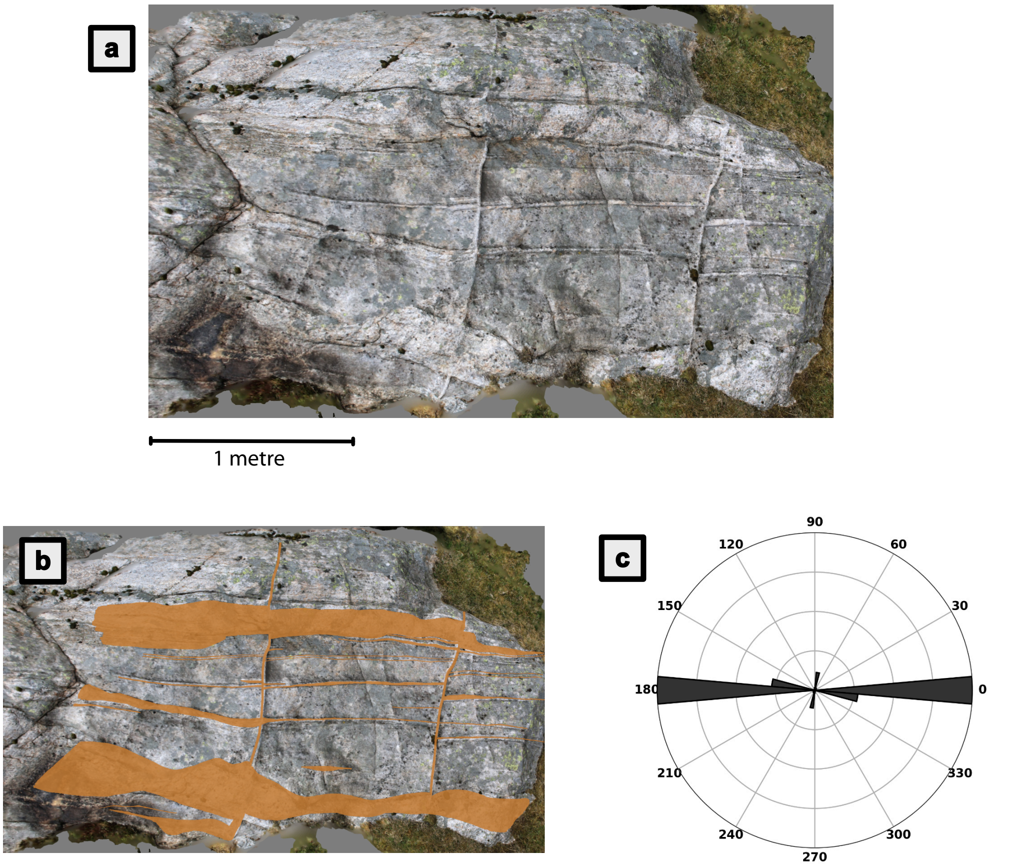

Figure 8.9: (a) Photo of the outcrop in Figure 3.10b (Rogaland region, Norway). (b) Interpretation of the melt distribution sketched on top of the original photo. (c) Orientation of the melt veins. Angle = 0° corresponds to the orientation of the foliation.

entation of the foliation. Figure 8.9c confirms that the melt pattern exhibits a strong dominant orientation parallel to the foliation and the larger layers. The limited presence of cross-cutting veins and their high angles relative to the foliation suggest only modest deformation. This is further supported by the small offsets observed along the fractures.

As discussed in Chapter 3, the region containing this outcrop experienced extensional deformation. However, based on the melt observed melt structures and the limited presence of discordant veins, we interpret that this specific location underwent significantly less deformation than locations N02 and N03 (Figure 3.7 and 3.8). In our numerical experiments, the high localisation of melt along host rock structures is associated with elevated melt pressure. These conditions are compatible with the interpretations reported in the literature (Goodenough et al. 2010), which say that, due to prolonged high-temperature conditions, a substantial volume of melt was formed. These conditions also mean that the melt fraction remained local. This behaviour is consistent with our interpretation of layer-parallel structures that show few discordant melt veins. They are networks that favour short-distance melt accumulation, such as along foliation planes, rather than extensive melt migration over long distances, hence the permanence of melt in the area.

A potential limitation of our analysis could come from the difference between the model and the field data: in the numerical experiments, we analyse fractures, which likely leads to an underestimation of the melt extent in the fertile layers. Furthermore, the rose diagrams in Figure 8.4b display the angles of fractures in fertile layers in a separate bar from other fracture angles. This separation likely contributes to the secondary orientation peaks appearing smaller.

8.5 Conclusions

This study has shown how fracture network development in partially molten rocks is strongly influenced by the relative roles of compositional layering and external deformation (extension). The key insights that can be gained from our numerical experiments are:

1. Impact of melt production rate contrast: If the difference between the melt production rate the fertile layers and the rate of the infertile layers is large, the fracture networks mainly develop layer-parallel (horizontal) fractures within the fertile layers. These structures promote local melt flow but, as they lack connectivity between layers, are not efficient at large-scale melt transport.

2. Role of deformation: In systems dominated by a high deformation rate, shear fractures become prevalent and cross-cut compositional layers. These discordant fractures enhance the connectivity of the melt network and allow upward migration of melt. They often form in locally parallel sets favouring one of the two possible shear orientations.

3. Interaction between compositional layers and external deformation: When both factors contribute to the fracture networks, the resulting patterns exhibit signatures of both processes. The combination of shear and layer-parallel fractures leads to complex and interconnected fracture networks. When shear fractures intersect a fertile layer, their orientation becomes slightly steeper, reflecting the larger contribution of melt pressure.

4. The effect of layer thickness: Thinner layers enhance fracture localisation, creating continuous and linear fractures. On the other hand, thicker layers lead to tortuous, branching fractures.

5. The discrete-continuum numerical model used in this study proved to be an effective method for simulating complex melt-producing zones affected by deformation and compositional layers. Comparisons with field data from migmatites in NW Scotland and the Rogaland region in Norway validated the numerical findings demonstrating the model's relevance to natural systems. Our increased understanding of the effect of the different processes allows us to make better interpretations of structures in layered systems.

Chapter 9

Discussion and Conclusions

9.1 The Use of *Latte* in Modelling Melt-Rock Systems

The work presented in this thesis shows that hybrid DEM-continuum models can be a powerful tool to investigate fracture patterns in zones of partial melting. The model *Latte* effectively captures the interaction between the solid and fluid phases and the influence that multiple processes have on the resulting fracture networks. Extensive testing in simplified setups (Chapter 5) was conducted to assess whether grid sizing and geometry influenced the results, ensuring the reliability of the model. This foundation allows confidence in the results generated from more complex simulations where multiple processes interact concurrently. This level of systematic testing had not been performed in previous studies and represents a valuable advancement in verifying the accuracy of the results in the numerical experiments. The tests also identified the parameter ranges where the code is most robust, providing a basis for selecting appropriate values for the simulations. In addition, improvements in the code performance significantly improved computational efficiency, which also allowed the model to be run on HPC facilities.

However, the model exhibits some limitations in fracture orientation, with certain angles being slightly favoured over others during the opening of an individual fracture. This bias must be considered when interpreting orientation data, as it could lead to the under-representation of certain angles, such as vertical orientations. In Chapter 6, this issue does not arise as we consider the orientation of clusters of fractures, rather than calculating the angle of individual ones. In Chapters 7 and 8, the algorithm that identifies the fracture geometry from the 2-D data merges smaller fractures into larger ones, calculating orientations that reflect the combination of the individual segments. These composite fractures typically form at angles that do not align with the directions of the solid grid such as vertical fractures. Nonetheless, the number of vertical fractures can still be relatively low (for instance, Figure 7.7b).

9.2 Enhanced Embrittlement and Network Formation for Highly Viscous Melt and Fast Melt Production

The first scientific research chapter involves a setup that could be considered a simplification of a natural migmatite, as it features a structurally and compositionally homogeneous rock under static conditions. However, these simplifications allow for the investigation of parameters such as melt viscosity and melt production rate, providing valuable insights into their individual roles, isolated from the influence of other factors. In this setup, our numerical experiments showed that fracture networks formed by melt overpressure are highly sensitive to melt viscosity and the rate of melt production. Extensive, well-connected networks only develop when melt is generated at a high rate and fluid pressure diffusion (through porous flow) is limited, conditions that favour strong fluid pressure localisation and melt-enhanced embrittlement (Davidson et al. 1994, Rushmer 2001).

When diffusion is highly efficient due to low melt production rates and low melt viscosity, the system struggles to develop fractures, and melt migration occurs through porous flow along grain boundaries, consistent with mechanisms suggested by Stuart et al. (2016) and Maierová et al. (2023). In this scenario, porous flow remains the dominant melt migration mechanism, and if fractures develop, they remain short, poorly connected, and insufficient to form a network. Melt migration occurs as a combination of porous flow and small-scale fracturing, which facilitates pressure diffusion but does not produce extensive fracture networks.

9.3 Unorganised Hydrofractures vs. Organised Networks: The Impact of Deformation

Our numerical experiments in Chapter 7 show that fracture patterns in partially molten rocks are strongly influenced by the relative rates of melt production, melt pressure diffusion and extensional deformation. Systems with high melt production rates under static conditions and low differential stress develop hydrofractures due to elevated fluid pressure. The resulting fractures have an irregular shape and form fracture networks with random orientations.

Systems dominated by extensional deformation without partial melting develop conjugate sets where fractures propagate linearly with both orientations. In contrast, when both deformation and partial melting are active, the interaction between these processes often results in asymmetrical networks where one orientation is favoured. A preferred orientation can be observed both in the homogeneous systems in Chapter 7 and, locally, between fertile layers in Chapter 8.

The transition from hydrofractures to shear fractures is not characterised by a sharp regime change. Instead, systems where both mechanisms are active exhibit both fracture styles simultaneously. The progression occurs gradually through a combination of both fracture styles, reflecting the relative contributions of fluid pressure and deformation in forming hybrid fractures. Fracture style is very sensitive to local stress variations, leading to fractures with varying angles within the same area. As observed in Chapter 8, this combination of fracture types is particularly evident in systems where fractures cross high-pressure layers: the fractures angle becomes steeper inside the fertile layer, highlighting the influence of elevated melt pressure in these zones.

9.4 Fracture Networks in Systems with Compositional Layering

Chapter 8 explores the role of compositional layering in the formation of fracture networks. In systems where the layers have a high contrast in melt production rate, layer-parallel fractures are favoured. If the rate of deformation is high, it can significantly affect the fracture network by favouring discordant shear fractures. The difference between the effects of the two factors, layers and deformation, is that the former promotes melt pressure accumulation inside the fertile layers, while the latter favours melt migration away from the layers.

Scenarios combining aspects of compositional layering and deformation result in complex fracture networks with both layer-parallel veins and discordant veins. The geometry of layers also affects the fracture network. Thicker layers produce less localised fractures, whereas thinner layers enhance stress localisation, promoting confined fracture patterns.

9.5 Interplay of Processes and their Relative Rates

Chapter 6 showed that the fracture network in a melt production zone is primarily governed by the balance between the rates of melt production and melt pressure diffusion. A fast rate of melt production has a similar impact on the network as a slow rate of melt pressure diffusion. Overall, the fracture network style and the type of fractures do not change significantly, indicating that it is the relative rate between these processes that plays a critical role.

On the other hand, adding external deformation can change the type of fractures observed in the networks, favouring shear fractures. The combined effect of high melt production and external deformation often leads to the development of parallel shear fractures. In these systems, conjugate sets with both angles may form, but one orientation typically becomes dominant.

We found that systems not affected by external deformation are able to develop interconnected networks, provided that the melt pressure is high. In this case, the networks are characterised by chaotic structures that do not exhibit preferred orientations (Reichardt & Weinberg 2012). However, a small amount of differential stress is sufficient to develop hybrid fractures oriented between 60° and 90°.

Pre-existing structures such as compositional layering leave an important signature on the melt network. Without strong external deformation, it is highly unlikely that the system will develop a fully connected network. In such cases, external deformation is essential for the formation of an efficient melt network, as it facilitates the connectivity needed for upward melt migration on a larger scale.

9.6 Strenghts and Limitations of our Methods of Fracture Analysis

In this thesis, fracture networks have been quantified using a few different methods. The use of rose diagrams for the representation of dyke orienation is well-established and quite common in the literature (e.g. Reichardt & Weinberg 2012). The analysis of melt networks with topological features is a novel approach. While effective in our numerical data, it can presents challenges when applied to melt distributions that deviate strongly from linear geometries, such as those with highly variable thickness. We found it effective for describing variations in fracture networks as a function of the investigated parameters and a useful tool for identifying trends. This approach is particularly effectuve when comparing a large number of networks that are relatively similar in appearance, as it ensures consistency in feature extraction across different cases.

An example of the challenges of applying this method to different fracture networks is the following. Our algorithm tends to break down fractures into short segments. The dimensionless intensity B_{22} can be considered as a measure of the relative total length over the number of branches:

$$B_{22} = \frac{N_B B_C^2}{A} \tag{9.1}$$

and, because $B_C = \Sigma L_B / N_B$, it is also:

$$B_{22} = \frac{\Sigma L_B}{N_B A}. \tag{9.2}$$

This parameter is quite sensitive to the definition of a branch. When characterising a fracture network, if many small branches are identified, N_B will be large and B_{22} will get smaller. For example, our values of B_{22} (Figures 6.9 and 7.8) are quite small compared to Sanderson & Nixon (2015), who used an example network with few large fractures. However, our method of detecting branches and nodes is consistent throughout the analyses of this study and therefore it is a good tool for identifying trends.

Our methods of analysis do not account for two-dimensional shape features, such as variations in thickness. Although the number of broken bonds can be used as a proxy for fracture aperture, it does not provide a fully accurate measure of vein thickness. Consequently, the interpretation of our results is limited to one-dimensional features, such as fracture length and orientation.

9.7 Using Results from Numerical Experiments to Interpret Structures in Natural Examples

In Chapters 7 and 8 we have shown that several features emerging from our numerical experiments can be recognised in natural migmatites, suggesting that our model provides valuable insights for their interpretation.

For example, the outcrop described in Chapter 7, Figures 7.1 and 7.10, includes several of such key features. The left-hand side of this outcrop displays both structures linked to deformation and geometries controlled by compositional layering (features discussed in Chapter 8). This area, identified in Figure 7.10 as region *a*, stands out as it is the only area where most veins are aligned with the foliation. This region also contains the lowest melt content, a feature consistent with reports in the literature that melt typically cross-cuts pre-existing anisotropy only when it organises into larger structures (Sawyer 2001, Marchildon & Brown 2003). The rose diagram of melt orientations for this region closely resembles the results from our numerical experiments with pre-existing structures (Figures 8.4 and 8.6): It includes a primary peak corresponding to features parallel to the anisotropy and a secondary peak representing a discordant set of fractures.

In contrast, the other regions contain large discordant dykes that exhibit behaviours predicted by our numerical results. Areas with more chaotic fracture networks, such as region *c*, are interpreted to have experienced higher fluid pressure. However, the overall area is dominated by large-scale dykes that cross-cut smaller-scale structures and display a single dominant orientation.

9.8 Model Limitations and Future Work

The main limitations presented by the model used in this study are the following:

1. The model is two-dimensional, which means that three-dimensional effects are not included and three-dimensional structures cannot be investigated. However, by orienting the simulated plane parallel to the principal stresses, the key mechanisms are still captured.

2. The model focuses on brittle-elastic behaviour and ductile deformation of the host rock is not incorporated. While this means it cannot simulate regimes where ductile deformation is significant, it is well-suited for studying systems dominated by brittle processes.

3. Thermal effects are not present in the model, and we assume a constant tem-

perature across the domain and over time. Temperature effects are incorporated into the material properties and behaviour, but they remain fixed throughout the numerical experiments. As a result, the model does not account for temperature-dependent solidification of the molten fraction, nor changes in rheology (Clemens 1998).

4. The model assumes a constant melt production rate with time, independent of the amount of melt already formed. In reality, the rate of melt production is highly variable and depends on specific reactions and rock types (Etheridge et al. 2021, Rushmer 2001). For example, most melt is produced over narrow temperature intervals during the breakdown of dominant hydrous phases, such as muscovite (White & Powell 2002).

5. While natural melts can exhibit complex a rheology (Clemens & Petford 1999), the model uses a purely Newtonian viscosity and does not account for the role of suspended solids or other phases.

Future directions to expand the model and explore more complex systems include:

1. Incorporating ductile deformation: Including viscous deformation would extend the model's applicability to systems where ductile processes play a significant role. Observations, such as those in Figure 3.12, highlight the potential insights that could be gained.

2. Expanding the deformation style to include different regimes, such as compression or simple shear.

3. Exploring different geometries: Chapter 8 includes a preliminary investigation of variations in layer geometries. A more detailed study could include changes in the angle of layers relative to principal stresses or discontinuities in the layers. Different geometries have been shown to create significantly different fracture patterns in systems with aqueous fluids (Koehn et al. 2020).

4. Varying physical properties between layers: While the current setup includes

differences in melt production rates (implying different lithologies), future work could incorporate mechanical differences between layers to model different rock types more accurately.

5. Simulating mechanical anisotropy: This would allow the model to simulate smaller-scale structures, such as foliation, providing a closer approximation to natural systems. Chapter 8 provides insights into larger-scale layered structures, which could complement studies focusing on finer-scale features.

9.9 Conclusions

The work presented in this thesis demonstrates that hybrid discrete-continuum models are an effective tool for investigating fracture patterns in zones of partial melting. This thesis represents a novel and systematic investigation into how patterns evolve in complex environments where multiple processes interact. After conducting thorough testing on the numerical code *Latte* and adapting it for melt-rock mixture environments, we conducted systematic studies on the effects of the relative rates of melt pressure diffusion, melt generation and extensional deformation. This work extends our ability to interpret geometrical patterns in rock-melt mixtures and link them to the processes that were active when such structures formed.

Our results show that when melt production is significantly faster than other processes, the system predominantly develops hydrofractures due to melt-induced embrittlement. These fractures can evolve into well-connected networks, even in the absence of external deformation. In fine-grained, brittle materials, such as those simulated in Chapter 6, clusters of relatively small cracks form. More heterogeneous and coarser-grained lithologies (Chapter 7) tend to develop longer fractures that grow into complex, unorganised networks.

If extensional deformation is present, the fracture network includes shear fractures too, and the prevalence of shear fractures increases with higher deformation rates.

Enhanced porosity created by partial melting favours rock compaction, fracture localisation and organisation. Fractures align into parallel sets rather than conjugate sets, resulting in asymmetrical structures. These networks may include both hybrid and hydrofractures, with their proportions determined by the relative rates of melting and deformation. These systems differ from deformation-only environments, where conjugate fracture sets with both failure orientations form.

When the melt production is localised in a series of fertile layers, layer-parallel fractures dominate. Such structures are efficient at local melt flow but lack connectivity between layers, limiting large-scale melt transport. In systems characterised by high deformation rates, shear fractures cross-cut compositional layers, enhancing melt network connectivity and upward melt migration. These fractures often align in locally parallel sets. Systems influenced by both compositional banding and external deformation lead to complex, interconnected fracture networks.

The numerical findings were validated and used to interpret field structures from two study areas, one near the boundary between the Rhiconich and the Assynt terranes, NW Scotland, and the other in the Rogaland region, Norway. We interpret the preferred orientation of large-scale dykes as evidence of active deformation when melt was present. The presence of discordant veins between layer-parallel melt veins was used to interpret the relative contribution of melt pressure and external deformation.

Bibliography

Aleksans, J., Koehn, D., Toussaint, R. & Daniel, G. (2020), 'Simulating Hydraulic Fracturing: Failure in Soft Versus Hard Rocks', *Pure and Applied Geophysics* **177**(6), 2771–2789.

Allibone, A. H. & Norris, R. (1992), 'Segregation of leucogranite microplutons during synâĂŘanatectic deformation: an example from the Taylor Valley, Antarctica', *Journal of Metamorphic Geology* **10**(4), 589–600.
URL: *https://onlinelibrary.wiley.com/doi/10.1111/j.1525-1314.1992.tb00107.x*

Anderson, T. B. & Jackson, R. (1967), 'Fluid mechanical description of fluidized beds: Equations of Motion', *Industrial and Engineering Chemistry Fundamentals* **6**(4), 527–539.
URL: *https://pubs.acs.org/doi/abs/10.1021/i160024a007*

ANSYS Inc. (n.d.).
URL: *https://www.ansys.com*

Ashworth, J. R. (1985), *Migmatites*, Blackie, Glasgow and London.

Barton, C. C. & Hsieh, P. A. (1989), Physical and hydrologic-flow properties of fractures, *in* '28th International Geological Congress: Environmental, Engineering and Urban Geology in the United States 2, Field Trip Guidebook T385', American Geophysical Union (AGU), Washington, DC, p. 36.

Beacom, L. (1999), 'The kinematic evolution of reactivated and non-reactivated faults

in basement rocks, NW Scotland.', *Doctoral dissertation, Queen's University of Belfast* .
URL: *https://ethos.bl.uk/OrderDetails.do?uin=uk.bl.ethos.394604*

Bell, T. H. & Etheridge, M. A. (1973), 'Microstructure of mylonites and their descriptive terminology', *Lithos* **6**(4), 337–348.

Berre, I., Doster, F. & Keilegavlen, E. (2019), 'Flow in Fractured Porous Media: A Review of Conceptual Models and Discretization Approaches', *Transport in Porous Media* **130**(1), 215–236.
URL: *https://doi.org/10.1007/s11242-018-1171-6*

Bingen, B., Davis, W. J., Hamilton, M. A., Engvik, A. K., Stein, H. J., Skår, Ã. & Nordgulen, Ã. (2008), 'Geochronology of high-grade metamorphism in the Sveconorwegian belt, S. Norway: U-Pb, Th-Pb and Re-Os data', *Norsk Geologisk Tidsskrift* **88**(1), 13–42.

Bingen, B., Skår, Ã., Marker, M., Sigmond, E. M., Nordgulen, Ã., Ragnhildstveit, J., Mansfeld, J., Tucker, R. D. & Liégeois, J. P. (2005), 'Timing of continental building in the Sveconorwegian orogen, SW Scandinavia', *Norsk Geologisk Tidsskrift* **85**(1-2), 87–105.

Blereau, E., Johnson, T. E., Clark, C., Taylor, R. J., Kinny, P. D. & Hand, M. (2017), 'Reappraising the P-T evolution of the Rogaland-Vest Agder Sector, southwestern Norway', *Geoscience Frontiers* **8**(1), 1–14.
URL: *http://dx.doi.org/10.1016/j.gsf.2016.07.003*

Bonamici, C. E. & Duebendorfer, E. M. (2010), 'Scale-invariance and self-organized criticality in migmatites of the southern Hualapai Mountains, Arizona', *Journal of Structural Geology* **32**(8), 1114–1124.
URL: *http://dx.doi.org/10.1016/j.jsg.2010.06.019*

Bons, P. D. D., Arnold, J., Elburg, M. A., Kalda, J., Soesoo, A. & van Milligen, B. P. (2004), 'Melt extraction and accumulation from partially molten rocks', *Lithos* **78**(1-2), 25–42.

Bons, P. D. D., Becker, J. K., Elburg, M. A. & Urtson, K. (2009), 'Granite formation: Stepwise accumulation of melt or connected networks?', *Earth and Environmental Science Transactions of the Royal Society of Edinburgh* **100**(1-2), 105–115.

Bons, P. D. D., Cao, D., de Riese, T., González-Esvertit, E., Koehn, D., Naaman, I., Sachau, T., Tian, H. & Gomez-Rivas, E. (2022), 'A review of natural hydrofractures in rocks', *Geological Magazine* pp. 1–26.

Bons, P. D. D., Druguet, E., Castaño, L. M. & Elburg, M. A. (2008), 'Finding what is now not there anymore: Recognizing missing fluid and magma volumes', *Geology* **36**(11), 851–854.

Bons, P. D. D., Elburg, M. A. & Gomez-Rivas, E. (2012), 'A review of the formation of tectonic veins and their microstructures', *Journal of Structural Geology* **43**, 33–62.
URL: *http://dx.doi.org/10.1016/j.jsg.2012.07.005*

Bons, P. D. D., Koehn, D. & Jessell, M. W. (2008), *Microdynamics Simulation*, Springer-Verlag Berlin.

Bons, P. D. D. & van Milligen, B. P. (2001), 'New experiment to model self-organized critical transport and accumulation of melt and hydrocarbons from their source rocks', *Geology* **29**(10), 919–922.

Bottinga, Y. & Weill, D. F. (1972), 'The viscosity of magmatic silicate liquids; a model calculation', *American Journal of Science* **272**(5), 438–475.
URL: *https://ajsonline.org/article/59543*

Brown, M. (1994), 'The generation, segregation, ascent and emplacement of granite magma: the migmatite-to-crustally-derived granite connection in thickened orogens', *Earth Science Reviews* **36**(1-2), 83–130.

Brown, M. (2004), 'The mechanism of melt extraction from lower continental crust of orogens', *Special Paper of the Geological Society of America* **389**(1999), 35–48.

Brown, M. (2005), 'Synergistic effects of melting and deformation: An example from the Variscan belt, western France', *Geological Society Special Publication* **243**, 205–226.

Brown, M. (2007), 'Crustal melting and melt extraction, ascent and emplacement in orogens: Mechanisms and consequences', *Journal of the Geological Society* **164**(4), 709–730.

Brown, M. (2010), 'The spatial and temporal patterning of the deep crust and implications for the process of melt extraction', *Philosophical Transactions of the Royal Society A: Mathematical, Physical and Engineering Sciences* **368**(1910), 11–51.

Brown, M. (2013), 'Granite: From genesis to emplacement', *Bulletin of the Geological Society of America* **125**(7-8), 1079–1113.

Brown, M. A., Brown, M., Carlson, W. D. & Denison, C. (1999), 'Topology of syntectonic melt-flow networks in the deep crust: Inferences from three-dimensional images of leucosome geometry in migmatites', *American Mineralogist* **84**(11-12), 1793–1818.

Brown, M., Averkin, Y. A., McLellan, E. L. & Sawyer, E. W. (1995), 'Melt segregation in migmatites', *Journal of Geophysical Research* **100**(B8).

Brown, M., Korhonen, F. J. & Siddoway, C. S. (2011), 'Organizing melt flow through the crust', *Elements* **7**(4), 261–266.

Brown, M. & Rushmer, T. (2006), *Evolution and differentiation of the continental crust*, Cambridge University Press (CUP).

Brown, M. & Solar, G. S. (1998), 'Granite ascent and emplacement during contractional deformation in convergent orogens', *Journal of Structural Geology* **20**(9-10), 1365–1393.

Bürgmann, R. & Dresen, G. (2008), 'Rheology of the lower crust and upper mantle: Evidence from rock mechanics, geodesy, and field observations', *Annual Review of Earth and Planetary Sciences* **36**, 531–567.

Burnham, C. W. (1979), The importance of volatile constituents, *in* 'Evolution of the

Igneous Rocks', Princeton University Press, pp. 439–482.
URL: *https://www.degruyter.com/document/doi/10.1515/9781400868506-017/html*

Carman, P. C. (1937), 'Fluid flow through granular beds', *Transactions, Institution of Chemical Engineers, London* **15**, 150–166.
URL: *http://dx.doi.org/10.1016/S0263-8762(97)80003-2*

Carman, P. C. (1956), *Flow of Gases through Porous Media*, Academic Press, New York.
URL: *https://ci.nii.ac.jp/naid/10003529006*

Carolan, D., Tuković, Å., Murphy, N. & Ivanković, A. (2013), 'Arbitrary crack propagation in multi-phase materials using the finite volume method', *Computational Materials Science* **69**, 153–159.
URL: *https://linkinghub.elsevier.com/retrieve/pii/S0927025612007124*

Clemens, J. D. (1998), 'Observations on the origins and ascent mechanisms of granitic magmas', *Journal of the Geological Society* **155**(5), 843–851.

Clemens, J. D. & Mawer, C. K. (1992), 'Granitic magma transport by fracture propagation', *Tectonophysics* **204**(3-4), 339–360.

Clemens, J. D. & Petford, N. (1999), 'Granitic melt viscosity and silicic magma dynamics in contrasting tectonic settings', *Journal of the Geological Society* **156**(6), 1057–1060.
URL: *http://jgs.lyellcollection.org/*

Clemens, J. D. & Stevens, G. (2016), 'Melt segregation and magma interactions during crustal melting: Breaking out of the matrix', *Earth-Science Reviews* **160**, 333–349.
URL: *http://dx.doi.org/10.1016/j.earscirev.2016.07.012*

Cobbold, P. R. & Rodrigues, N. (2007), 'Seepage forces, important factors in the formation of horizontal hydraulic fractures and bedding-parallel fibrous veins ('beef' and 'cone-in-cone')', *Geofluids* **7**(3), 313–322.

Connolly, J. A. D., Holness, M. B., Rubie, D. C. & Rushmer, T. (1997), 'Reaction-induced microcracking: An experimental investigation of a mechanism for enhancing anatectic melt extraction', *Geology* **25**(7), 591–594.

Connolly, J. A. D. & Podladchikov, Y. Y. (1998), 'Compaction-driven fluid flow in viscoelastic rock', *Geodinamica Acta* **11**(2-3), 55–84.

Corfu, F., Heaman, L. M. & Rogers, G. (1994), 'Polymetamorphic evolution of the Lewisian complex, NW Scotland, as recorded by U-Pb isotopic compositions of zircon, titanite and rutile', *Contributions to Mineralogy and Petrology* **117**(3), 215–228.

Cosgrove, J. W. (1995), 'The expression of hydraulic fracturing in rocks and sediments', *Geological Society, London, Special Publications* **92**(1), 187–196.
URL: *https://www.lyellcollection.org/doi/10.1144/GSL.SP.1995.092.01.10*

Cox, S. (2005), 'Coupling between Deformation, Fluid Pressures, and Fluid Flow in Ore-Producing Hydrothermal Systems at Depth in the Crust', *Society of Economic Geologists, Inc. Economic Geology 100th Anniversary Volume* pp. 39–75.

Cruden, A. R. & Weinberg, R. F. (2018), Mechanisms of Magma Transport and Storage in the Lower and Middle Crust - Magma Segregation, Ascent and Emplacement, *in* 'Volcanic and Igneous Plumbing Systems', Elsevier, pp. 13–53.
URL: *http://dx.doi.org/10.1016/B978-0-12-809749-6/00002-9*

Cundall, P. A. & Strack, O. D. (1979), 'A discrete numerical model for granular assemblies', *Geotechnique* **29**(1), 47–65.
URL: *https://experts.umn.edu/en/publications/discrete-numerical-model-for-granular-assemblies*

Daczko, N. R. & Piazolo, S. (2022), 'Recognition of melferite – A rock formed in syn-deformational high-strain melt-transfer zones through sub-solidus rocks: A review and synthesis of microstructural criteria', *Lithos* **430-431**(May), 106850.

Dannberg, J. & Heister, T. (2016), 'Compressible magma/mantle dynamics: 3-D, adaptive simulations in ASPECT', *Geophysical Journal International* **207**(3), 1343–1366.

Dash, B. (1969), 'Structure of the Lewisian rocks between Strath Dionard and Rhiconich, Sutherland, Scotland', *Scottish Journal of Geology* **5**(4), 347–374.

Dash, B. & Bowes, D. R. (2014), 'Lewisian Complex of Strath Dionard-Rhiconich and its significance in the early history of the NW Highlands of Scotland', *Scottish Journal of Geology* **50**(1), 27–47.

Davidson, C., Schmid, S. M. & Hollister, L. S. (1994), 'Role of melt during deformation in the deep crust', *Terra Nova* **6**(2), 133–142.
URL: *https://onlinelibrary.wiley.com/doi/10.1111/j.1365-3121.1994.tb00646.x*

Dell'Angelo, L. N. & Tullis, J. (1988), 'Experimental deformation of partially melted granitic aggregates', *Journal of Metamorphic Geology* **6**, 495–515.

Dershowitz, W. S. & Herda, H. H. (1992), 'Interpretation of fracture spacing and intensity'.

Diener, J. F. A. & Fagereng, Ã. (2014), 'The influence of melting and melt drainage on crustal rheology during orogenesis', *Journal of Geophysical Research: Solid Earth* **119**(8), 6193–6210.
URL: *https://agupubs.onlinelibrary.wiley.com/doi/10.1002/2014JB011088*

Diener, J. F., White, R. W. & Hudson, T. J. (2014), 'Melt production, redistribution and accumulation in mid-crustal source rocks, with implications for crustal-scale melt transfer', *Lithos* **200-201**(1), 212–225.
URL: *http://dx.doi.org/10.1016/j.lithos.2014.04.021*

Drüppel, K., Elsäßer, L., Brandt, S. & Gerdes, A. (2013), 'Sveconorwegian mid-crustal ultrahigh-temperature metamorphism in Rogaland, Norway: U-Pb LA-ICP-MS geochronology and pseudosections of sapphirine granulites and associated paragneisses', *Journal of Petrology* **54**(2), 305–350.

Ester, M., Kriegel, H.-P., Sander, J. & Xu, X. (1996), 'A Density-Based Algorithm for Discovering Clusters in Large Spatial Databases with Noise', *Proceedings of the Second In-*

ternational Conference on Knowledge Discovery and Data Mining (KDD-96) p. 226âĂŞ231.
URL: *https://cdn.aaai.org/KDD/1996/KDD96-037.pdf*

Etheridge, M. A., Daczko, N. R., Chapman, T. & Stuart, C. A. (2021), 'Mechanisms of melt extraction during lower crustal partial melting', *Journal of Metamorphic Geology* **39**(1), 57–75.
URL: *https://doi.org/10.1111/jmg.12561*

Flekkøy, E. G., Malthe-Sørenssen, A. & Jamtveit, B. (2002), 'Modeling hydrofracture', *Journal of Geophysical Research* **107**(B8), 1–11.

Friend, C. R. & Kinny, P. D. (1995), 'New evidence for protolith ages of Lewisian granulites, northwest Scotland', *Geology* **23**(11), 1027–1030.

Friend, C. R. & Kinny, P. D. (2001), 'A reappraisal of the Lewisian Gneiss Complex: Geochronological evidence for its tectonic assembly from disparate terranes in the Proterozoic', *Contributions to Mineralogy and Petrology* **142**(2), 198–218.

Fyfe, W. (1978), *Fluids In The Earth's Crust*, Elsevier, Amsterdam.

Ganzhorn, A. C., Trap, P., Arbaret, L., Champallier, R., Fauconnier, J., Labrousse, L. & Prouteau, G. (2016), 'Impact of gneissic layering and localized incipient melting upon melt flow during experimental deformation of migmatites', *Journal of Structural Geology* **85**, 68–84.
URL: *http://dx.doi.org/10.1016/j.jsg.2016.02.004*

Ghani, I., Koehn, D., Toussaint, R. & Passchier, C. W. (2013), 'Dynamic Development of Hydrofracture', *Pure and Applied Geophysics* **170**(11), 1685–1703.

Ghani, I., Koehn, D., Toussaint, R. & Passchier, C. W. (2015), 'Dynamics of hydrofracturing and permeability evolution in layered reservoirs', *Frontiers in Physics* **3**(September), 1–16.

Goodenough, K. M., Crowley, Q. G., Krabbendam, M. & Parry, S. F. (2013), 'New U-Pb age constraints for the Laxford Shear Zone, NW Scotland: Evidence for tectono-

magmatic processes associated with the formation of a Paleoproterozoic supercontinent', *Precambrian Research* **233**, 1–19.
URL: *http://dx.doi.org/10.1016/j.precamres.2013.04.010*

Goodenough, K. M., Park, R. G., Krabbendam, M., Myers, J. S., Wheeler, J., Loughlin, S. C., Crowley, Q. G., Friend, C. R., Beach, A., Kinny, P. D. & Graham, R. H. (2010), 'The Laxford shear zone: An end-Archaean terrane boundary?', *Geological Society Special Publication* **335**, 103–120.

Gueguen, Y. & Dienes, J. (1989), 'Transport properties of rocks from statistics and percolation', *Mathematical Geology* **21**(1), 1–13.

Hack, A. C. & Thompson, A. B. (2011), 'Density and viscosity of hydrous magmas and related fluids and their role in subduction zone processes', *Journal of Petrology* **52**(7-8), 1333–1362.

Hagberg, A. A., Schult, D. A. & Swart, P. J. (2008), Exploring Network Structure, Dynamics, and Function using NetworkX, *in* 'Proceedings of the 7th Python in Science Conference', pp. 11–15.
URL: *https://doi.curvenote.com/10.25080/TCWV9851*

Handy, M. R., Mulch, A., Rosenau, M. & Rosenberg, C. L. (2001), 'The role of fault zones and melt as agents of weakening, hardening and differentiation of the continental crust: A synthesis', *Geological Society Special Publication* **186**, 305–332.

Harris, N., Ayres, M. & Massey, J. (1995), 'Geochemistry of granitic melts produced during the incongruent melting of muscovite: implications for the extraction of Himalayan leucogranite magmas', *Journal of Geophysical Research* **100**(B8).

Hasalová, P., Schulmann, K., Lexa, O., Štípská, P., Hrouda, F., Ulrich, S., Haloda, J. & Týcová, P. (2008), 'Origin of migmatites by deformation-enhanced melt infiltration of orthogneiss: A new model based on quantitative microstructural analysis', *Journal of Metamorphic Geology* **26**(1), 29–53.

Healy, D., Rizzo, R. E., Cornwell, D. G., Farrell, N. J., Watkins, H., Timms, N. E., Gomez-Rivas, E. & Smith, M. (2017), 'FracPaQ: A MATLABâĎć toolbox for the quantification of fracture patterns', *Journal of Structural Geology* **95**, 1–16.

Hermans, G., Tobi, A., Poorter, R. & Maijer, C. (1975), 'The high-grade metamorphic Precambrian of the Sirdal-Ørsdal area, Rogaland/Vest-Agder, south-west Norway', *Norges Geologiske Undersøkelse Bulletin* **318**, 51–74.

Hobbs, B. E. & Ord, A. (2010), 'The mechanics of granitoid systems and maximum entropy production rates', *Philosophical Transactions of the Royal Society A: Mathematical, Physical and Engineering Sciences* **368**(1910), 53–93.
URL: *https://royalsocietypublishing.org/doi/10.1098/rsta.2009.0202*

Holness, M. B., Cesare, B. & Sawyer, E. W. (2011), 'Melted rocks under the microscope: Microstructures and their interpretation', *Elements* **7**(4), 247–252.

Holtzman, B. K., Groebner, N. J., Zimmerman, M. E., Ginsberg, S. B. & Kohlstedt, D. L. (2003), 'Stress-driven melt segregation in partially molten rocks', *Geochemistry, Geophysics, Geosystems* **4**(5).

Holyoke, C. W. & Rushmer, T. (2002), 'An experimental study of grain scale melt segregation mechanisms in two common crustal rock types', *Journal of Metamorphic Geology* **20**(5), 493–512.

Hubbert, M. K. & Rubey, W. W. (1959), 'Role of Fluid Pressure in Mechanics of Overthrust Faulting', *Geological Society of America Bulletin* **70**, 167.

Hubbert, M. K. & Willis, D. G. (1957), 'Mechanics of hydraulic fracturing', *Mechanics of Hydraulic Fracture* **210**.

Itasca Consulting Group (n.d.), 'UDEC - Universal Distinct Element Code'.

Jackson, M. D. & Cheadle, M. J. (1998), 'A continuum model for the transport of heat, mass and momentum in a deformable, multicomponent mush, undergoing solid-liquid phase change', *International Journal of Heat and Mass Transfer* **41**(8-9), 1035–1048.

Jackson, M. D., Cheadle, M. J. & Atherton, M. P. (2003), 'Quantitative modeling of granitic melt generation and segregation in the continental crust', *Journal of Geophysical Research: Solid Earth* **108**(B7).

Jaeger, J. C. & Cook, N. G. W. (1976), *Fundamentals of Rock Mechanics*, Vol. 114, xviii edn, Geological Magazine, London.

Jessell, M. W., Bons, P. D. D., Evans, L., Barr, T. & Stüwe, K. (2001), 'Elle: The numerical simulation of metamorphic and deformation microstructures', *Computers and Geosciences* **27**(1), 17–30.

Jing, L. & Stephansson, O. (1997), 'Network Topology and Homogenization of Fractured Rocks', *Fluid Flow and Transport in Rocks* pp. 191–202.
URL: *https://link.springer.com/book/10.1007/978-94-009-1533-6*

Kinny, P. D. & Friend, C. R. (1997), 'U-Pb isotopic evidence for the accretion of different crustal blocks to form the Lewisian Complex of northwest Scotland', *Contributions to Mineralogy and Petrology* **129**(4), 326–340.

Kinny, P. D., Friend, C. R. & Love, G. J. (2005), 'Proposal for a terrane-based nomenclature for the Lewisian Gneiss Complex of NW Scotland', *Journal of the Geological Society* **162**(1), 175–186.

Koehn, D., Arnold, J. & Passchier, C. W. (2005), 'Fracture and vein patterns as indicators of deformation history: A numerical study', *Geological Society Special Publication* **243**(1985), 11–24.

Koehn, D., Piazolo, S., Sachau, T. & Toussaint, R. (2020), 'Fracturing and Porosity Channeling in Fluid Overpressure Zones in the Shallow Earth's Crust', *Geofluids* .

Koehn, D., Steiner, A. & Aanyu, K. (2019), 'Modelling of extension and dyking-induced collapse faults and fissures in rifts', *Journal of Structural Geology* **118**(October 2018), 21–31.
URL: *https://doi.org/10.1016/j.jsg.2018.09.017*

Kohlstedt, D. L. & Zimmerman, M. E. (1996), 'Rheology of partially molten mantle rocks', *Annual Review of Earth and Planetary Sciences* **24**, 41–62.

Kozeny, J. (1927), 'Ueber kapillare Leitung des Wassers im Boden', *Sitzungsber Akad. Wiss.Wien* **136**, 271–306.

Laporte, D. & Watson, E. B. (1995), 'Experimental and theoretical constraints on melt distribution in crustal sources: the effect of crystalline anisotropy on melt interconnectivity', *Chemical Geology* **124**(3-4), 161–184.

Lee, D., Cardiff, P., Bryant, E. C., Manchanda, R., Wang, H. & Sharma, M. M. (2015), A New Model for Hydraulic Fracture Growth in Unconsolidated Sands with Plasticity and Leak-Off, *in* 'SPE Annual Technical Conference and Exhibition', Vol. 2015-Janua, SPE, pp. 1300–1320.
URL: *https://onepetro.org/SPEATCE/proceedings/15ATCE/15ATCE/D021S015R005/180305*

Leitch, A. M. & Weinberg, R. F. (2002), 'Modelling granite migration by mesoscale pervasive flow', *Earth and Planetary Science Letters* **200**(1-2), 131–146.

Long, J. C., Remer, J. S., Wilson, C. R. & Witherspoon, P. A. (1982), 'Porous media equivalents for networks of discontinuous fractures', *Water Resources Research* **18**(3), 645–658.
URL: *https://agupubs.onlinelibrary.wiley.com/doi/10.1029/WR018i003p00645*

Louis-Napoleon, A., Bonometti, T., Gerbault, M., Martin, R. & Vanderhaeghe, O. (2022), 'Models of convection and segregation in heterogeneous partially molten crustal roots with a VOF method - I: Flow regimes', *Geophysical Journal International* **229**(3), 2047–2080.

Maaløe, S. (1992), 'Melting and diffusion processes in closed-system migmatization', *Journal of Metamorphic Geology* **10**(4), 503–516.
URL: *https://onlinelibrary.wiley.com/doi/10.1111/j.1525-1314.1992.tb00101.x*

Maccaferri, F., Bonafede, M. & Rivalta, E. (2010), 'A numerical model of dyke propagation in layered elastic media', *Geophysical Journal International* **180**(3), 1107–1123.

Maierová, P., Hasalová, P., Schulmann, K., Štípská, P. & Souček, O. (2023), 'Porous Melt Flow in Continental Crust - A Numerical Modeling Study', *Journal of Geophysical Research: Solid Earth* **128**(8), 1–25.
URL: *https://agupubs.onlinelibrary.wiley.com/doi/10.1029/2023JB026523*

Maillot, B., Nielsen, S. & Main, I. (1999), 'Numerical simulation of seismicity due to fluid injection in a brittle poroelastic medium', *Geophysical Journal International* **139**(2), 263–272.

Malthe-Sørenssen, A. (1998), 'Modeling and characterization of fracture patterns in the Vatnajokull glacier', *Geology* **26**(10), 931–934.

Malthe-Sørenssen, A., Walmann, T., Feder, J., Jøssang, T., Meakin, P. & Hardy, H. H. (1998), 'Simulation of extensional clay fractures', *Physical Review E - Statistical Physics, Plasmas, Fluids, and Related Interdisciplinary Topics* **58**(5), 5548–5564.

Malthe-Sørenssen, A., Walmann, T., Jamtveit, B., Feder, J. & Jøssang, T. (1999), 'Simulation and characterization of fracture patterns in glaciers', *Journal of Geophysical Research: Solid Earth* **104**(B10), 23157–23174.

Manzocchi, T. (2002), 'The connectivity of two-dimensional networks of spatially correlated fractures', *Water Resources Research* **38**(9), 1–1.

Marchildon, N. & Brown, M. (2002), 'Grain-scale melt distribution in two contact aureole rocks: Implications for controls on melt localization and deformation', *Journal of Metamorphic Geology* **20**(4), 381–396.

Marchildon, N. & Brown, M. (2003), 'Spatial distribution of melt-bearing structures in anatectic rocks from Southern Brittany, France: Implications for melt transfer at grain- to orogen-scale', *Tectonophysics* **364**(3-4), 215–235.

Marsh, B. D. (1982), 'On the mechanics of igneous diapirism, stoping, and zone melting.'.

Martini, A., Bitencourt, M. d. F., Weinberg, R. F. & De Toni, G. B. (2019), 'Melt-collecting structures and the formation of extraction dykes during syntectonic anatexis of the Camboriú Complex, south Brazil', *Journal of Structural Geology* **127**(July), 103866.
URL: *https://doi.org/10.1016/j.jsg.2019.103866*

Mason, A. J. (2016), 'The Palaeoproterozoic anatomy of the Lewisian Complex, NW Scotland: Evidence for two 'Laxfordian' tectonothermal cycles', *Journal of the Geological Society* **173**(1), 153–169.

McKenzie, D. (1984), 'The Generation and Compaction of Partially Molten Rock', *Journal of Petrology* **25**(3), 713–765.
URL: *https://academic.oup.com/petrology/article-lookup/doi/10.1093/petrology/25.3.713*

Meek, U., Piazolo, S. & Daczko, N. R. (2019), 'The field and microstructural signatures of deformation-assisted melt transfer: Insights from magmatic arc lower crust, New Zealand', *Journal of Metamorphic Geology* **37**(6), 795–821.

Nermoen, A., Galland, O., Jettestuen, E., Fristad, K., Podladchikov, Y., Svensen, H. & Malthe-Sørenssen, A. (2010), 'Experimental and analytic modeling of piercement structures', *Journal of Geophysical Research: Solid Earth* **115**(10), 1–15.

Nicolas, A. & Ildefonse, B. (1996), 'Flow mechanism and viscosity in basaltic magma chambers', *Geophysical Research Letters* **23**(16), 2013–2016.

Nicolas, A. & Jackson, M. (1982), 'High temperature dikes in peridotites: Origin by hydraulic fracturing', *Journal of Petrology* **23**(4), 568–582.

Nyberg, B., Nixon, C. W. & Sanderson, D. J. (2018), 'NetworkGT: A GIS tool for geometric and topological analysis of two-dimensional fracture networks', *Geosphere* **14**(4), 1618–1634.

Oliver, N. H. S. & Barr, T. D. (1997), 'The geometry and evolution of magma pathways through migmatites of the Halls Creek Orogen, Western Australia', *Mineralogical Magazine* **61**(404), 3–14.

Paquet, J., Francois, P. & Nedelec, A. (1981), 'Effect of partial melting on rock deformation: Experimental and natural evidences on rocks of granitic compositions', *Tectonophysics* **78**, 545–565.

Park, R. G. & Tarney, J. (1987), 'The Lewisian complex: A typical Precambrian high-grade terrain?', *Geological Society Special Publication* **27**(27), 13–25.

Patiño Douce, A. E., Humphreys, E. D. & Dana Johnston, A. (1990), 'Anatexis and metamorphism in tectonically thickened continental crust exemplified by the Sevier hinterland, western North America', *Earth and Planetary Science Letters* **97**(3-4), 290–315.

Pedregosa, F., Varoquaux, G., Gramfort, A., Michel, V., Thirion, B., Grisel, O., Blondel, M., Prettenhofer, P., Weiss, R., Dubourg, V., Vanderplas, J., Passos, A., Cournapeau, D., Brucher, M., Perrot, M. & Duchesnay, E. (2011), 'Scikit-learn: Machine Learning in Python', *Journal of Machine Learning Research* **12**, 2825–2830.

Petford, N. (1995), 'Segregation of Tonalitic-Trondhjemitic Melts in the Continental Crust : Relatively Melt Porosities Relatively Viscosity Melts', *Journal of Geophysical Research* **100**(B8), 735–743.

Petford, N., Cruden, A. R., McCaffrey, K. J. & Vigneresse, J. L. (2000), 'Granite magma formation, transport and emplacement in the Earth's crust', *Nature* **408**(6813), 669–673.

Petford, N. & Koenders, M. A. (1998), 'Self-organisation and fracture connectivity in rapidly heated continental crust', *Journal of Structural Geology* **20**(9-10), 1425–1434.

Piazolo, S., Bons, P. D. D., Griera, A., Llorens, M. G., Gomez-Rivas, E., Koehn, D., Wheeler, J., Gardner, R., Godinho, J. R., Evans, L., Lebensohn, R. A. & Jessell, M. W. (2019), 'A review of numerical modelling of the dynamics of microstructural

development in rocks and ice: Past, present and future', *Journal of Structural Geology* **125**, 111–123.
URL: *https://doi.org/10.1016/j.jsg.2018.05.025*

Powell, R., Guiraud, M. & White, R. W. (2005), 'Truth and beauty in metamorphic phase-equilibria: Conjugate variables and phase diagrams', *Canadian Mineralogist* **43**(1), 21–33.

Rees Jones, D. W. & Katz, R. F. (2018), 'Reaction-infiltration instability in a compacting porous medium', *Journal of Fluid Mechanics* **852**, 5–36.

Reichardt, H. & Weinberg, R. F. (2012), 'The dike swarm of the Karakoram shear zone, Ladakh, NW India: Linking granite source to batholith', *Bulletin of the Geological Society of America* **124**(1-2), 89–103.

Ribe, N. M. (1985), 'The deformation and compaction of partial molten zones', *Geophysical Journal International* **83**(2), 487–501.
URL: *https://academic.oup.com/gji/article-lookup/doi/10.1111/j.1365-246X.1985.tb06499.x*

Riquelme, A. J., Abellán, A., Tomás, R. & Jaboyedoff, M. (2014), 'A new approach for semi-automatic rock mass joints recognition from 3D point clouds', *Computers and Geosciences* **68**, 38–52.
URL: *http://dx.doi.org/10.1016/j.cageo.2014.03.014*

Rivalta, E., Taisne, B., Bunger, A. P. & Katz, R. F. (2015), 'A review of mechanical models of dike propagation: Schools of thought, results and future directions', *Tectonophysics* **638**(C), 1–42.
URL: *http://dx.doi.org/10.1016/j.tecto.2014.10.003*

Rosenberg, C. L. & Handy, M. R. (2000), 'Syntectonic melt pathways during simple shearing of a partially molten rock analogue (Norcamphor-Benzamide)', *Journal of Geophysical Research: Solid Earth* **105**(B2), 3135–3149.

Rubin, A. M. (1993), 'Dikes vs. diapirs in viscoelastic rock', *Earth and Planetary Science Letters* **119**(4), 641–659.

Rushmer, T. (1991), 'Partial melting of two amphibolites: contrasting experimental results under fluid-absent conditions', *Contributions to Mineralogy and Petrology* **107**(1), 41–59.
URL: *http://link.springer.com/10.1007/BF00311184*

Rushmer, T. (2001), 'Volume change during partial melting reactions: Implications for melt extraction, melt geochemistry and crustal rheology', *Tectonophysics* **342**(3-4), 389–405.

Rutter, E. H. (1997), The influence of deformation on the extraction of crustal melts: A consideration of the role of melt-assisted granular flow, *in* M. Holness, ed., 'Deformation-enhanced fluid transport in the EarthâĂŹs crust and mantle', Chapman and Hall, London, p. 82âĂŞ110.

Rutter, E. H. & Mecklenburgh, J. (2006), The extraction of melt from crustal protoliths and the flow behavior of partially molten crustal rocks: an experimental perspective, *in* M. Brown & T. Rushmer, eds, 'Evolution and Differentiation of the Continental Crust', Cambridge University Press, Cambridge, pp. 385–430.

Rutter, E. H. & Neumann, D. H. (1995), 'Experimental deformation of partially molten Westerly granite under fluid-absent conditions, with implications for the extraction of granitic magmas', *Journal of Geophysical Research* **100**(B8).

Sachau, T. & Koehn, D. (2013), 'A new mixed-mode fracture criterion for large scale lattice models', *Geosci. Model Dev. Discuss.* **6**, 4327–4343.

Sanderson, D. J. & Nixon, C. W. (2015), 'The use of topology in fracture network characterization', *Journal of Structural Geology* **72**, 55–66.
URL: *http://dx.doi.org/10.1016/j.jsg.2015.01.005*

Sangnimnuan, A., Li, J. & Wu, K. (2021), 'Development of coupled two phase flow and

geomechanics model to predict stress evolution in unconventional reservoirs with complex fracture geometry', *Journal of Petroleum Science and Engineering* **196**(October 2020), 108072.
URL: *https://doi.org/10.1016/j.petrol.2020.108072*

Sawyer, E. W. (2001), 'Melt segregation in the continental crust: Distribution and movement of melt in anatectic rocks', *Journal of Metamorphic Geology* **19**(3), 291–309.

Sawyer, E. W. & Brown, M. (2008), 'Working with Migmatites: Nomenclature for the Constituent Parts', *Mineralogical Association of Canada Short Course Series* **38**, 1–28.

Scott, D. R. & Stevenson, D. J. (1986), 'Magma Ascent by Porous Flow', *Journal of Geophysical Research* **91**, 9283–9296.

Shaw, H. R. (1972), 'Viscosities of magmatic silicate liquids; an empirical method of prediction', *American Journal of Science* **272**(9), 870–893.

Slagstad, T., Roberts, N. M., Coint, N., Høy, I., Sauer, S., Kirkland, C. L., Marker, M., Røhr, T. S., Henderson, I. H., Stormoen, M. A., Skår, Ã., Sørensen, B. E. & Bybee, G. (2018), 'Magma-driven, high-grade metamorphism in the Sveconorwegian Province, southwest Norway, during the terminal stages of Fennoscandian Shield evolution', *Geosphere* **14**(2), 861–882.

Slagstad, T., Roberts, N. M. & Kulakov, E. V. (2017), 'Linking orogenesis across a supercontinent; the Grenvillian and Sveconorwegian margins on Rodinia', *Gondwana Research* **44**, 109–115.
URL: *http://dx.doi.org/10.1016/j.gr.2016.12.007*

Slagstad, T., Roberts, N. M., Marker, M., Røhr, T. S. & Schiellerup, H. (2013), 'A non-collisional, accretionary Sveconorwegian orogen', *Terra Nova* **25**(1), 30–37.

Sleep, N. H. (1988), 'Tapping of melt by veins and dikes', *Journal of Geophysical Research* **93**(B9), 10255–10272.

Soesoo, A., Kalda, J., Bons, P. D. D., Urtson, K. & Kalm, V. (2004), 'Fractality in geology:

A possible use of fractals in the studies of partial melting processes', *Proceedings of the Estonian Academy of Sciences: Geology* **53**(1), 13–27.

Spiegelman, M. (1993*a*), 'Flow in deformable porous media. Part 1 Simple analysis', *Journal of Fluid Mechanics* **247**, 17–38.

Spiegelman, M. (1993*b*), 'Physics of melt extraction: theory, implications and applications', *Philosophical Transactions - Royal Society of London, A* **342**, 23–41.

Stuart, C. A., Piazolo, S. & Daczko, N. R. (2016), 'Mass transfer in the lower crust: Evidence for incipient melt assisted flow along grain boundaries in the deep arc granulites of Fiordland, New Zealand', *Geochemistry, Geophysics, Geosystems* **17**(9), 3733–3753.
URL: *http://doi.wiley.com/10.1002/2015GC006236*

Stuart, C. A., Piazolo, S. & Daczko, N. R. (2018), 'The recognition of former melt flux through high-strain zones', *Journal of Metamorphic Geology* **36**(8), 1049–1069.

Sumita, I. & Ota, Y. (2011), 'Experiments on buoyancy-driven crack around the brittle-ductile transition', *Earth and Planetary Science Letters* **304**(3-4), 337–346.
URL: *http://dx.doi.org/10.1016/j.epsl.2011.01.032*

Sutton, J. & Watson, J. (1950), 'The pre-Torridonian metamorphic history of the Loch Torridon and Scourie areas in the North-West Highlands, and its bearing on the chronological classification of the Lewisian', *Quarterly Journal of the Geological Society of London* **106**(1-4), 241–307.

Tanner, D. C. (1999), 'The scale-invariant nature of migmatite from the Oberpfalz, NE Bavaria and its significance for melt transport', *Tectonophysics* **302**(3-4), 297–305.

The OpenFOAM Foundation (n.d.).
URL: *www.openfoam.org*

Thompson, A. B. (1999), 'Some time-space relationships for crustal melting and granitic intrusion at various depths', *Geological Society, London, Special Publications* **168**(1), 7–

25.
URL: *https://www.lyellcollection.org/doi/10.1144/GSL.SP.1999.168.01.02*

Tomkins, H. S., Williams, I. S. & Ellis, D. J. (2005), 'In situ U-Pb dating of zircon formed from retrograde garnet breakdown during decompression in Rogaland, SW Norway', *Journal of Metamorphic Geology* **23**(4), 201–215.

Turcotte, D. L. & Ahern, J. L. (1978), 'A porous flow model for magma migration in the asthenosphere', *Journal of Geophysical Research: Solid Earth* **83**(B2), 767–772.
URL: *https://agupubs.onlinelibrary.wiley.com/doi/10.1029/JB083iB02p00767*

Van der Molen, I. & Paterson, M. S. (1979), 'Experimental Deformation of Partially-Melted Granite', *Contributions to Mineralogy and Petrology* **70**, 299–318.

Vanderhaeghe, O. (2001), 'Melt segregation, pervasive melt migration and magma mobility in the continental crust: The structural record from pores to orogens', *Physics and Chemistry of the Earth, Part A: Solid Earth and Geodesy* **26**(4-5), 213–223.

Vanderhaeghe, O. (2009), 'Migmatites, granites and orogeny: Flow modes of partially-molten rocks and magmas associated with melt/solid segregation in orogenic belts', *Tectonophysics* **477**(3-4), 119–134.
URL: *http://dx.doi.org/10.1016/j.tecto.2009.06.021*

Vanderkam, D. (2021), 'Extract Raster Network'.
URL: *https://github.com/danvk/extract-raster-network*

Vass, A., Koehn, D., Toussaint, R., Ghani, I. & Piazolo, S. (2014), 'The importance of fracture-healing on the deformation of fluid-filled layered systems', *Journal of Structural Geology* **67**(PA), 94–106.
URL: *http://dx.doi.org/10.1016/j.jsg.2014.07.007*

Walmann, T., Malthe-Sørenssen, A., Feder, J., Jøssang, T., Meakin, P. & Hardy, H. H. (1996), 'Scaling relations for the lengths and widths of fractures', *Physical Review Letters* **77**(27), 5393–5396.

Watkins, J. M., Clemens, J. D. & Treloar, P. J. (2007), 'Archaean TTGs as sources of younger granitic magmas: Melting of sodic metatonalites at 0.6-1.2 GPa', *Contributions to Mineralogy and Petrology* **154**(1), 91–110.

Weinberg, R. F. (1999), 'Mesoscale pervasive felsic magma migration: Alternatives to dyking', *Lithos* **46**(3), 393–410.

Weinberg, R. F. & Podladchikov, Y. Y. (1994), 'Diapiric ascent of magmas through power law crust and mantle', *Journal of Geophysical Research: Solid Earth* **99**, 9543–9559.

Weinberg, R. F. & Regenauer-Lieb, K. (2010), 'Ductile fractures and magma migration from source', *Geology* **38**(4), 363–366.

Weinberg, R. F. & Sarle, M. P. (1998), 'The Pangong Injection Complex, Indian Karakoram: a case of pervasive granite flowthrough hot viscous crust', *Journal of the Geological Society* **155**(5), 883–891.
URL: *https://www.lyellcollection.org/doi/10.1144/gsjgs.155.5.0883*

Westphal, M., Schumacher, J. C. & Boschert, S. (2003), 'High-temperature metamorphism and the role of magmatic heat sources at the Rogaland Anorthosite Complex in Southwestern Norway', *Journal of Petrology* **44**(6), 1145–1162.

White, R. W. & Powell, R. (2002), 'Melt loss and the preservation of granulite facies mineral assemblages', *Journal of Metamorphic Geology* **20**(7), 621–632.

Whitehouse, M. J. (1989), 'Sm-Nd evidence for diachronous crustal accretion in the Lewisian complex of northwest Scotland', *Tectonophysics* **161**(3-4), 245–256.

Wickham, S. M. (1987), 'The segregation and emplacement of granitic magmas', *Journal of the Geological Society* **144**(2), 281–297.
URL: *https://www.lyellcollection.org/doi/10.1144/gsjgs.144.2.0281*

Wrona, T., Brune, S., Gayrin, P. & Hake, T. (2022), 'Fatbox - Fault Analysis Toolbox'.
URL: *https://github.com/thilowrona/fatbox*

Yakymchuk, C., Brown, M., Ivanic, T. & Korhonen, F. (2013), 'Leucosome distribution

in migmatitic paragneisses and orthogneisses: A record of self-organized melt migration and entrapment in a heterogeneous partially-molten crust', *Tectonophysics* **603**, 136–154.
URL: *http://dx.doi.org/10.1016/j.tecto.2013.05.022*